MEASUREMENT OF $|V_{ub}|$ USING b SEMILEPTONIC DECAY

By

Jiansen Lu

B.Sc., University of Science and Technology of China,1986

M.Sc., University of Saskatchewan, 1997

A THESIS SUBMITTED IN PARTIAL FULFILLMENT OF

THE REQUIREMENTS FOR THE DEGREE OF

DOCTOR OF PHILOSOPHY

in

THE FACULTY OF GRADUATE STUDIES

DEPARTMENT OF PHYSICS AND ASTRONOMY

We accept this thesis as conforming

to the required standard

.....

.....

.....

.....

.....

THE UNIVERSITY OF BRITISH COLUMBIA

December, 2001

In presenting this thesis in partial fulfilment of the requirements for an advanced degree at the University of British Columbia, I agree that the Library shall make it freely available for reference and study. I further agree that permission for extensive copying of this thesis for scholarly purposes may be granted by the head of my department or by his or her representatives. It is understood that copying or publication of this thesis for financial gain shall not be allowed without my written permission.

_____

Department of Physics and Astronomy
The University of British Columbia
6224 Agricultural Road
Vancouver, B.C., Canada
V6T 1Z1

Date:

_____

Abstract

The magnitude of the CKM matrix element $|V_{ub}|$ is determined by measuring the inclusive charmless semileptonic branching fraction of beauty hadrons at OPAL based on $b \to X_u \ell\nu$ event topology and kinematics. This analysis uses OPAL data collected between 1991 and 1995, which correspond to about four million hadronic Z decays. $\mathrm{Br}(b \to X_u \ell\nu)$ is measured to be $(1.63 \pm 0.53\ ^{+0.55}_{-0.62}) \times 10^{-3}$. The first uncertainty is the statistical error and the second is the systematic error. From this analysis, $|V_{ub}|$ is determined to be:

$$|V_{ub}| = (4.00 \pm 0.65\ (\mathrm{stat})\ ^{+0.67}_{-0.76}\ (\mathrm{sys}) \pm 0.19\ (\mathrm{HQE})) \times 10^{-3}.$$

The last error represents the theoretical uncertainties related to the extraction of $|V_{ub}|$ from $\mathrm{Br}(b \to X_u \ell\nu)$ using the Heavy Quark Expansion.

Table of Contents

List of Tables

List of Figures

Acknowledgements

I would like to thank my supervisor Dr. Janis McKenna for her help and guidance throughout the work. Her encouragement and patience have been invaluable in the completion of this project.

I have worked at CERN for more than 14 months for the OPAL online data reconstruction. I had a very pleasant time to work with Gordon Long, Carla Sbarra, Ian Bailey and Brigitte Vachon for the OPAL online data reconstruction. Thanks for their help and sharing the duty.

Thanks to those OPAL physicists: Oliver Cooke, Pauline Gagnon, Alain Bellerive, Bob Kowalewski, Rob McPherson and Richard Hawkings for a lot of good discussions for this V_{ub} analysis. Thanks to Christoph Schwick for his help with the $b \to X_u \ell \nu$ hybrid model.

I would like to thank my PhD committee for all their help in my academic progress.

The financial support from my supervisor's NSERC grants and UBC Physics and Astronomy Department is gratefully acknowledged.

I am grateful to my fellow graduate student Douglas Thiessen for sharing the computer lab teaching assistantship and sharing four years of student life.

Finally I must thank my wife Hui Xu. With her encouragement, I continue to stay in my science and research career. I also want to thank my wife again for bringing my son Andy Lu to this world last June.

Chapter 1

Introduction

This thesis presents a measurement of $|V_{ub}|$ using b semileptonic decay. The data used in this analysis consist of four million hadronic Z decays collected with the OPAL detector at the LEP accelerator between 1991 and 1995.

In this chapter an overview of the Cabibbo, Kobayashi and Maskawa (CKM) matrix [1] in the Standard Model of particle physics is presented. Measurements of $|V_{ub}|$ are discussed. An outline of this thesis is presented.

1.1 The CKM matrix in the Standard Model

The Standard Model is used to describe the fundamental particles of nature and their interactions. According to the Standard Model, matter is built of six quarks and six leptons and their anti-particles, shown in Table 1.1, which interact via the exchange of gauge bosons. The Standard Model contains a neutral Higgs boson that is introduced for the SU(2)$\otimes$U(1) symmetry breaking. There is no experimental evidence for the neutral Higgs boson yet.

There are four interactions, namely strong, weak, electromagnetic and gravitation, so far as we know. Each interaction is mediated by the exchange of bosons. The strong

interaction is mediated by a gluon. The weak interaction is mediated by $W^{\pm}$ and Z bosons. The electromagnetic interaction is mediated by a photon and the gravitational interaction is supposedly mediated by a graviton.

The Standard Model unifies the electroweak interaction, electromagnetic interaction and strong interaction based on group theory SU(3)⊗SU(2)⊗U(1).

Leptons	$\begin{pmatrix} \nu_e \\ e \end{pmatrix}$ $\begin{pmatrix} \nu_\mu \\ \mu \end{pmatrix}$ $\begin{pmatrix} \nu_\tau \\ \tau \end{pmatrix}$
Quarks	$\begin{pmatrix} u \\ d \end{pmatrix}$ $\begin{pmatrix} c \\ s \end{pmatrix}$ $\begin{pmatrix} t \\ b \end{pmatrix}$
Gauge Bosons	γ, $W^{\pm}$ and Z, gluons

Table 1.1: The basic particles of the Standard Model. γ is a photon.

The SU(2)⊗U(1) in the Standard Model is the gauge group of the electroweak interaction. Quark weak eigenstates are different from their mass eigenstates for their respective interactions. The weak eigenstates and mass eigenstates are connected by the CKM matrix. A quark q_i decays weakly to a quark q_j and a W boson, as shown in Figure 1.1. The decay rate is proportional to the CKM matrix element $|V_{ij}|^2$. The interaction Lagrangian for flavour-changing quark transitions coupling to W bosons can be written as:

$$\mathcal{L}_{\text{int}} = \frac{-g}{\sqrt{2}}(\mathcal{J}^{\mu}\mathcal{W}_{\mu}^{+} + \mathcal{J}^{\mu\dagger}\mathcal{W}_{\mu}^{-}), \tag{1.1}$$

where g is a gauge coupling constant. $\mathcal{W}_{\mu}^{+}$ is an operator which annihilates a W^+ or creates a W^- and vice verse for $\mathcal{W}_{\mu}^{-}$. The charged current $\mathcal{J}^{\mu}$ is equal to:

$$\mathcal{J}^{\mu} = \sum_{i,j} \bar{u}_i \gamma^{\mu} \frac{1}{2}(1 - \gamma_5) V_{ij} d_j, \tag{1.2}$$

where the i and j are indices running from 1 to 3. $\bar{u}_i$ is a field operator which creates u, c and t quarks or annihilates their corresponding anti-particles as the index i runs

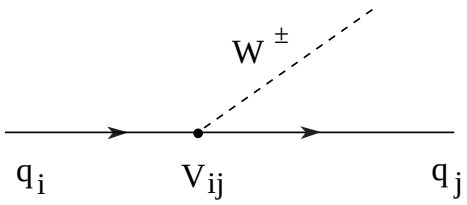

Figure 1.1: The quark q_i weak decay to the quark q_j by W boson. V_{ij} is a CKM matrix element.

from 1 to 3. d_j is a field operator which annihilates d, s and b quarks or creates their corresponding anti-particles as the index j runs from 1 to 3. The V_{ij} is the CKM matrix element. The CKM matrix is defined as following:

$$\begin{pmatrix} d' \\ s' \\ b' \end{pmatrix} = \begin{pmatrix} V_{ud} & V_{us} & V_{ub} \\ V_{cd} & V_{cs} & V_{cb} \\ V_{td} & V_{ts} & V_{tb} \end{pmatrix} \begin{pmatrix} d \\ s \\ b \end{pmatrix}, \tag{1.3}$$

where d′, s′ and b′ are the weak eigenstates, d, s and b are the mass eigenstates. It is the CKM matrix which specifies a rotation of basis from mass to weak eigenstates.

A common approximate parameterization of the CKM matrix is the Wolfenstein form [2]:

$$\begin{pmatrix} 1-\lambda^2/2 & \lambda & A\lambda^3(\rho - i\eta) \\ -\lambda & 1-\lambda^2/2 & A\lambda^2 \\ A\lambda^3(1-\rho-i\eta) & -A\lambda^2 & 1 \end{pmatrix},$$

where λ is the Cabibbo mixing angle and has a value around 0.21. A, ρ and η are of order unity.

The 90% confidence limits on magnitudes from recent measurements [2] and the

requirement that the CKM matrix be unitary are:

$$\begin{pmatrix} 0.9742 - 0.9757 & 0.219 - 0.226 & 0.002 - 0.005 \\ 0.219 - 0.225 & 0.9734 - 0.9749 & 0.037 - 0.043 \\ 0.004 - 0.014 & 0.035 - 0.043 & 0.9990 - 0.9993 \end{pmatrix}.$$

Measurements of the CKM matrix elements are described briefly below:

$|V_{ud}|$: $|V_{ud}|$ is precisely determined to be 0.9740 ± 0.0010 from superallowed $0^+ \to 0^+$ nuclear β decay compared to the muon decay rate [2]. The uncertainties are mainly from nuclear structure corrections and isospin symmetry breaking corrections. $|V_{ud}|$ can also be obtained from free neutron decay and charged pion decay, but with larger uncertainties.

$|V_{us}|$: $|V_{us}|$ is determined to be 0.2196 ± 0.0023 from K^0 and K^+ semileptonic decays [3].

$|V_{ub}|$: $|V_{ub}|$ is measured to be $(3.3 \pm 0.8) \times 10^{-3}$ from $B \to \pi \ell \nu$ and $B \to \rho \ell \nu$ from CLEO measurements [4]. $|V_{ub}|$ can also be measured from inclusive b to u semileptonic decays. The average $|V_{ub}|$ from inclusive measurements of ALEPH, DELPHI and L3, the other three LEP experiments, is $(4.13\ ^{+0.63}_{-0.75}) \times 10^{-3}$ [5]. This current analysis also measures $|V_{ub}|$ using inclusive b to u semileptonic decay. The result will be incorporated with other three LEP experiments and be used to produce a new LEP $|V_{ub}|$ value.

$|V_{cd}|$: $|V_{cd}|$ is measured to be 0.224 ± 0.016 from the differential cross section of $\nu_\mu N \to \mu^- cX$, i.e. the charm production rate in neutrino interactions with valence quarks in nucleus [2]. There is a large theoretical uncertainty in predicting this differential cross section due to the sea quarks, especially due to the s quark contributions.

$|V_{cs}|$: $|V_{cs}|$ is determined to be 1.04 ± 0.16 from $D \to \bar{K} \ell^+ \nu$ [2]. The recent measurement value of $|V_{cs}|$ from $W^\pm \to$ hadrons from the DELPHI experiment is $0.94^{+0.32}_{-0.26} \pm 0.13$

[6], where the unitarity of the CKM matrix and three generations of quarks are assumed. $|V_{cs}|$ can also be extracted from $\nu_\mu N \to \mu^- cX$, similar to the extraction of $|V_{cd}|$. But the uncertainty is large due to lack of knowledge regarding the contribution of $s\bar{s}$ pair to the parton sea.

$|V_{cb}|$: $|V_{cb}|$ can be measured from $B \to D\ell\nu$ and $B \to D^*\ell\nu$ decays. The average value of $|V_{cb}|$ is 0.0395 ± 0.0017 [2].

$|V_{td}|$ and $|V_{ts}|$: $|V_{td}|$ and $|V_{ts}|$ can be measured from $B_d^0\bar{B}_d^{\,0}$ and $B_s\bar{B}_s$ mixing. Using $\Delta M_{B_d} = (0.472 \pm 0.018)$ ps^{-1} (using convention $\hbar = c = 1$) from $B^0\bar{B}^0$ mixing, where ΔM_{B_d} is the mass difference between the high mass and low mass in B_d^0 system, $|V_{tb}^* V_{td}|$ is determined to be 0.0084 ± 0.0018 [2]. $|V_{ts}|$ can be obtained by using the unitarity of the CKM matrix:

$$V_{us}V_{ub}^* + V_{cs}V_{cb}^* + V_{ts}V_{tb}^* = 0. \tag{1.4}$$

As the first term in Equation 1.4 is tiny, $|V_{ts}|$ is equal to $|V_{cs}V_{cb}^*/V_{tb}^*|$ and is approximately equal to $|V_{cb}|$.

$|V_{tb}|$: $|V_{tb}|$ is measured from t to b semileptonic decay from CDF and D0 experiments and the result is [2]:

$$\frac{|V_{tb}|^2}{|V_{td}|^2 + |V_{ts}|^2 + |V_{tb}|^2} = 0.99 \pm 0.29. \tag{1.5}$$

The requirement of unitarity of the CKM matrix produces:

$$V_{ud}V_{ub}^* + V_{cd}V_{cb}^* + V_{td}V_{tb}^* = 0. \tag{1.6}$$

Since V_{ud} and V_{tb} are real numbers and approximately equal to 1 and $V_{cd} = -\lambda < 0$, the above equation can be written as:

$$\frac{V_{ub}^*}{|V_{cd}V_{cb}^*|} + \frac{V_{td}}{|V_{cd}V_{cb}^*|} = 1, \tag{1.7}$$

which can be depicted as the unitarity triangle in a complex plane in Figure 1.2. If a deviation from unitarity could be proven, the physics beyond the Standard Model will be discovered.

The angles α, β and γ in the unitarity triangle are related to the phase in the CKM matrix. The observed Charge Parity (CP) violation is solely related to a nonzero value of this phase, which can be measured in $B^0 - \bar{B}^0$ mixing. The Feynman diagrams for $B^0 - \bar{B}^0$ mixing are shown in Figure 1.3.

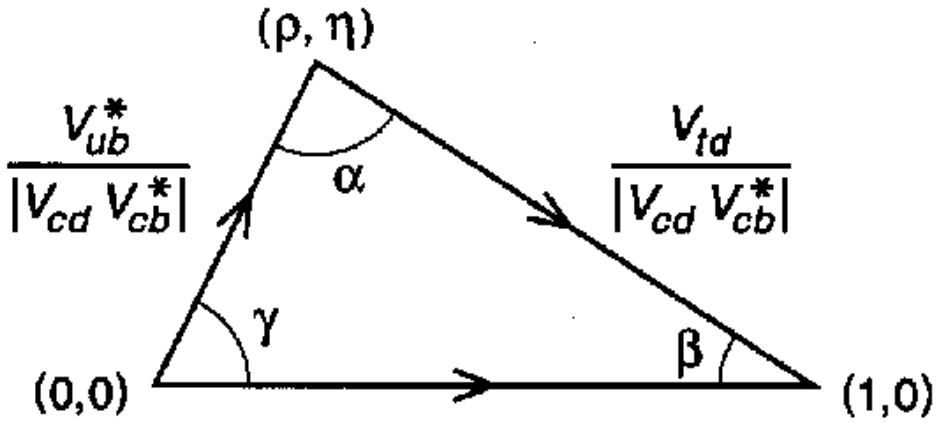

Figure 1.2: The unitarity triangle derived from constraints on the CKM matrix.

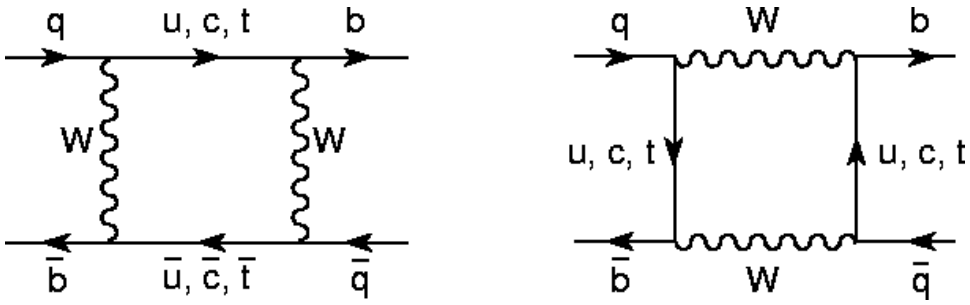

Figure 1.3: Feynman diagrams for $B^0 - \bar{B}^0$ mixing.

As CP is not good symmetry of nature, the mass eigenstates in the weak interaction are different from flavour eigenstates. The flavour eigenstate for B^0 is $\bar{b}d$ and for $\bar{B}^0$ is $b\bar{d}$.

The low mass B_1 and high mass B_2 eigenstates can be expressed as linear combinations of flavour eigenstates, B^0 and $\bar{B}^0$:

$$|B_1\rangle = p|B^0\rangle + q|\bar{B}^0\rangle, \tag{1.8}$$

$$|B_2\rangle = p|B^0\rangle - q|\bar{B}^0\rangle, \tag{1.9}$$

where p and q are complex coefficients and obey the normalization condition:

$$|p|^2 + |q|^2 = 1. \tag{1.10}$$

The coefficients p and q are governed by a time-dependent Schrödinger equation:

$$i\frac{d}{dt}\begin{pmatrix} p \\ q \end{pmatrix} = \begin{pmatrix} M - \frac{i\Gamma}{2} & M_{12} - \frac{i\Gamma_{12}}{2} \\ M_{12}^* + \frac{i\Gamma_{12}^*}{2} & M - \frac{i\Gamma}{2} \end{pmatrix}\begin{pmatrix} p \\ q \end{pmatrix}. \tag{1.11}$$

The time evolution of $|B^0(t)\rangle$ and $|\bar{B}^0(t)\rangle$ in terms of basis states $|B^0\rangle$ and $|\bar{B}^0\rangle$ can be written as [7]:

$$|B^0(t)\rangle = g_+(t)|B^0\rangle + \frac{q}{p}g_-(t)|\bar{B}^0\rangle, \tag{1.12}$$

$$|\bar{B}^0(t)\rangle = \frac{p}{q}g_-(t)|B^0\rangle + g_+(t)|\bar{B}^0\rangle, \tag{1.13}$$

where

$$g_+(t) = e^{-iMt}e^{\frac{-\Gamma t}{2}}\cos(\frac{\Delta m_B}{2}t), \tag{1.14}$$

$$g_-(t) = e^{-iMt}e^{\frac{-\Gamma t}{2}}\sin(\frac{\Delta m_B}{2}t), \tag{1.15}$$

where Δm_B is the mass difference between the high mass $|B_2\rangle$ and the low mass $|B_1\rangle$ states. Defining the final states (CP eigenstates) from B^0 and $\bar{B}^0$, such as $\pi^+\pi^-$ and $J/\psi K_s$ as f_{CP}, the decay widths for B^0 and $\bar{B}^0$ decay to f_{CP} can be written as [7]:

$$\Gamma(B^0(t) \to f_{CP}) = |A|^2e^{-\Gamma t}(\frac{1+|\lambda|^2}{2} - \frac{1-|\lambda|^2}{2}\cos(M_{12}t) - Im(\lambda)\sin(M_{12}t)), \tag{1.16}$$

$$\Gamma(\bar{B}^0(t) \to f_{CP}) = |A|^2e^{-\Gamma t}(\frac{1+|\lambda|^2}{2} - \frac{1-|\lambda|^2}{2}\cos(M_{12}t) - Im(\lambda)\sin(M_{12}t)), \tag{1.17}$$

where

$$\lambda = \frac{q\bar{A}}{pA}, \tag{1.18}$$

and

$$A = \langle f_{CP}|\mathcal{H}|B^0\rangle, \tag{1.19}$$

$$\bar{A} = \langle f_{CP}|\mathcal{H}|\bar{B}^0\rangle, \tag{1.20}$$

where $\mathcal{H}$ is the Hamiltonian. The time dependent CP asymmetry $\alpha(t)$ can be defined as:

$$\alpha(t) = \frac{\Gamma(\bar{B}^0(t) \to f_{CP}) - \Gamma(B^0(t) \to f_{CP})}{\Gamma(\bar{B}^0(t) \to f_{CP}) + \Gamma(B^0(t) \to f_{CP})} = -Im(\lambda)\sin(M_{12}t). \tag{1.21}$$

For $B^0 \to \pi^+\pi^-$ and $B^0 \to J/\psi K_s$ decays, $Im(\lambda)$ is equal to $\sin(2\alpha)$ and $\sin(2\beta)$ respectively. The angles α and β in the unitarity triangle can be measured from CP asymmetry in the B system and will provide additional information to the unitarity triangle. Any inconsistency in this unitarity triangle may be a hint or a sign of new physics.

1.2 Measurements of $|V_{ub}|$

V_{ub}, an element of the CKM matrix, describes decays of the b to u quark. Its magnitude, $|V_{ub}|$, can be calculated by measuring the inclusive $b \to u$ semileptonic decay rate, which refers to the total decay rate with all possible final-state hadrons in $b \to u$ semileptonic decay, ignoring the detailed breakdown among the individual modes. Given that the branching fraction of inclusive $b \to u$ semileptonic decay is of order 10^{-3}, a large number of b hadrons is required to measure $|V_{ub}|$. The dominant background to $b \to X_u\ell\nu$ comes from $b \to X_c\ell\nu$ decays because the branching ratio of $b \to X_c\ell\nu$ is more than 50 times greater than that of $b \to X_u\ell\nu$. Here the lepton ℓ refers to either an electron or a muon, and b denotes all weakly decaying b hadrons[1]. X_u and X_c represent hadronic

[1] Charged conjugate states are implied if not stated otherwise.

states resulting from a b quark semileptonic decay to a u or c quark respectively. The determination of $|V_{ub}|$ depends on the b to u and b to c semileptonic decay models.

The lepton endpoint energy E_{max} for $b \to X_u \ell\nu$ and $b \to X_c \ell\nu$ can be calculated as:

$$E_{max} = \frac{m_B^2 - m_X^2 + m_\ell^2}{2m_B}, \tag{1.22}$$

where m_B and m_ℓ are the mass of B meson and the mass of the lepton ℓ respectively. m_X is the mass of X_u or X_c. The E_{max} can be calculated as 2.64 GeV and 2.31 GeV for $B \to \pi\ell\nu$ and $\bar{B} \to D\ell\nu$ respectively. The inclusive method developed by ARGUS [8] and CLEO [9] is to extract $|V_{ub}|/|V_{cb}|$ from the excess of events in the 2.31 to 2.64 GeV/c region of the lepton momentum spectrum in the B meson rest frame, where the $b \to X_c \ell\nu$ contributions vanish. This technique uses only a small fraction of the lepton phase space and so has considerable model dependence in extrapolating to the entire lepton spectrum in the B rest frame. In addition, since the LEP experiments can not precisely determine the B meson rest frame, this method is not appropriate for the LEP experiments. Instead, at LEP, $|V_{ub}|$ or $|V_{ub}|/|V_{cb}|$ is extracted using a larger portion of the lepton spectrum as well as other kinematic variables. The inclusive measurement of the branching fraction of the $b \to X_u \ell\nu$ decay has also been performed at LEP by ALEPH [10], DELPHI [11] and L3 [12].

The theoretical uncertainty for the value of $|V_{ub}|$ extracted from a measurement of the inclusive $b \to X_u \ell\nu$ branching fraction differs from that extracted from measurements of exclusive b $\to$ u semileptonic decay rates. A recent theoretical study concludes that there is a 5% theoretical uncertainty on $|V_{ub}|$ values derived from $b \to X_u \ell\nu$ inclusive measurements [13], using the Heavy Quark Expansion. There is a 15% theoretical uncertainty associated with $|V_{ub}|$ values extracted from measurements of the exclusive branching fractions $B \to \pi\ell\nu$ or $B \to \rho\ell\nu$ [14], interpreted within the framework of the Heavy Quark Effective Theory (HQET).

The current analysis uses OPAL 1991 to 1995 data, collected near the Z resonance, comprising about four million hadronic Z decays. Monte Carlo simulated events were generated using the JETSET 7.4 [15] generator, with parameters described in [16]. Approximately five million hadronic $Z \to b\bar{b}$ decays were generated to study the $b \to X_c \ell\nu$ decay and the $b \to c \to \ell$ cascade decay. Six million hadronic $Z \to q\bar{q}$ (where q can be u, d, s, c and b) decays were generated to study the leptons from primary charm quarks and light quarks. Two hundred thousand events from a $b \to X_u \ell\nu$ hybrid model [17] were produced to simulate the $b \to u$ semileptonic decay. The $b \to X_u \ell\nu$ hybrid model will be described in detail in Section 2.4.

1.3 Outline

In this thesis, the determination of $|V_{ub}|$ using the inclusive $b \to X_u \ell\nu$ decay rate from the OPAL data taken at the center of mass energies near the Z resonance is described. The b semileptonic decay, the OPAL detector, the event preselection, $b \to X_u \ell\nu$ decay models and the neural network used to separate $b \to X_u \ell\nu$ from the background will be discussed in detail in the following chapters.

In Chapter 2 the theory behind b to u semileptonic decay models is discussed. An overview of the current status of $|V_{ub}|$ measurements is presented. A hybrid model for the b to u semileptonic decay is discussed.

In Chapter 3 descriptions of the LEP accelerator, the OPAL detector and the online data reconstruction are presented. OPAL subdetectors are discussed in detail.

In Chapter 4 an event preselection is presented. Multihadron selection, b tag, lepton selection and b semileptonic decay selection are discussed in detail. The concept of an artificial neural network is reviewed as neural networks are used several times in this analysis.

In Chapter 5 an identification of the b to u semileptonic decay is presented. $b \to X_u \ell\nu$ neural network and its input variables are discussed in detail. The $b \to X_u \ell\nu$ neural network output distributions for different signal and background compositions are also discussed.

In Chapter 6 the χ^2 fit method which is used to extract the branching fraction $\mathrm{Br}(b \to X_u \ell\nu)$ from the $b \to X_u \ell\nu$ neural network is presented. The systematic error analysis and cross checks for $\mathrm{Br}(b \to X_u \ell\nu)$ are presented. The extraction of $|V_{ub}|$ from $\mathrm{Br}(b \to X_u \ell\nu)$ is also discussed.

In Chapter 7 the final results for the branching fraction of $b \to X_u \ell\nu$ decay and $|V_{ub}|$ are presented. The average of $|V_{ub}|$ values from the four LEP experiments is also presented.

In Appendices, my contribution to OPAL collaboration is presented and a glossary of terminology in this thesis is also presented.

Chapter 2

b SEMILEPTONIC DECAY AND HYBRID MODEL

In this chapter an overview of b quark and b hadron physics is presented. The theory behind $b \to X_c \ell\nu$ and $b \to X_u \ell\nu$ semileptonic decays is presented. A $b \to X_u \ell\nu$ hybrid model is described.

2.1 Introduction to b physics

Bound $b\bar{b}$ states have a rich spectrum and are collectively called Υ mesons. $\Upsilon(1S)$ was first observed in 1977 in the $\mu^+\mu^-$ spectrum from 400 GeV protons striking a nuclear target at the Fermi National Laboratory (FNAL) under the direction of Dr. Leon Lederman [18]. One year later, the $\Upsilon(1S)$ and $\Upsilon(2S)$ were confirmed in e^+e^- annihilation at the DORIS Ring in Hamburg [19]. The CUSB and CLEO experiments at the Cornell Electron-positron Storage Ring (CESR) at Cornell University also confirmed $\Upsilon(1S)$ and $\Upsilon(2S)$ in 1979 and discovered $\Upsilon(3S)$ and $\Upsilon(4S)$ in 1980 [20]. Later B mesons were also discovered at CESR [21]. In 1987, the ARGUS experiment in DESY first observed the evidence of $B^0\bar{B}^0$ mixing [22]. In 1989, evidence for b to u semileptonic decay was observed

by the ARGUS and CLEO experiments [8, 9]. Almost at the same time, Isgur and Wise and Voloshin and Shifman developed the Heavy Quark Effective Theory (HQET) [23, 24] to describe heavy quark transitions. Using HQET, the calculation of the transition rate for b semileptonic decay can be simplified. In 1993, B_s and Λ_b were discovered by LEP experiments at CERN [25]. The same year, CLEO found evidence of the penguin decay $B \to K^*\gamma$ [26]. In 1997, a series of B rare decays, including $B \to K\pi$, were discovered by CLEO at CESR [27]. A brief summary of the history of b physics is shown in Table 2.1.

1977	Discovery of $\Upsilon(1s)$ at FNAL
1983	Discovery of B meson at Cornell
1987	Discovery of $B^0\bar{B}^0$ mixing at DESY
1989	Discovery of $B \to X_u\ell\bar{\nu}$ at Cornell and DESY
1989	Heavy Quark Effective Theory by Isgur, Wise, Voloshin and Shifman
1993	Discovery of B_s and Λ_b at CERN
1993-1994	Discovery of radiative penguin decays $B \to K^*\gamma$ and $B \to X_s\gamma$
1997	Discovery of $B \to K\pi$ rare decay at Cornell

Table 2.1: A brief history of b physics.

2.2 *b* hadron production

The *b* hadron can be produced by e^+e^- or $p\bar{p}$ collider or fixed target experiments. The three main approaches for *b* hadron production are: $e^+e^- \to \Upsilon(4S) \to B\bar{B}$, $e^+e^- \to Z \to b\bar{b}$ and $p\bar{p} \to b\bar{b}X$. The competitive detectors and accelerators associated with the *b* hadron production are shown in Table 2.2.

The current analysis uses the OPAL data of Z decay to multihadrons. OPAL is one

$b\bar{b}$ production	Detectors	Accelerator	N($b\bar{b}$) 10^6
$e^+e^- \to \Upsilon(4S) \to B\bar{B}$	CLEO II	CESR	5.1
$e^+e^- \to \Upsilon(4S) \to B\bar{B}$	BABAR	PEP II	>10
$e^+e^- \to \Upsilon(4S) \to B\bar{B}$	BELLE	KEKB	>10
$e^+e^- \to Z \to b\bar{b}$	ALEPH, DELPHI, OPAL, L3	LEP	0.9
$e^+e^- \to Z \to b\bar{b}$	SLD	SLC	0.08
$p\bar{p} \to b\bar{b}X$	CDF, D0	Tevatron	600

Table 2.2: Some existing experiments to study b physics

of the four experiments in the Large Electron Positron (LEP) collider at CERN. From 1990 to 1995, the center of mass energy was around the Z resonance (91.1 GeV) and these data were used in this analysis. After 1995 the center of mass energy was increased to produce W pairs for studying triple gauge boson coupling. The primary quark pair or the lepton pair can be produced from Z decay. The decay of Z into quark pairs results in multihadronic events. The lowest order Feynman diagrams for Z decay to multihadrons are shown in Figure 2.1. The decay rate of Z to fermion pairs, $\Gamma_{Z\to f\bar{f}}$ from the lowest order, using the Born approximation is:

$$\Gamma_{Z\to f\bar{f}} = (c_V^2 + c_A^2)\frac{G_F M_Z^3}{24\pi\sqrt{2}}, \tag{2.1}$$

with

$$G_F = \frac{\sqrt{2}e^2}{8M_W^2 \sin^2\theta_W},$$
$$c_V = I_3^f - 2\sin^2\theta_W Q_f,$$
$$c_A = I_3^f,$$

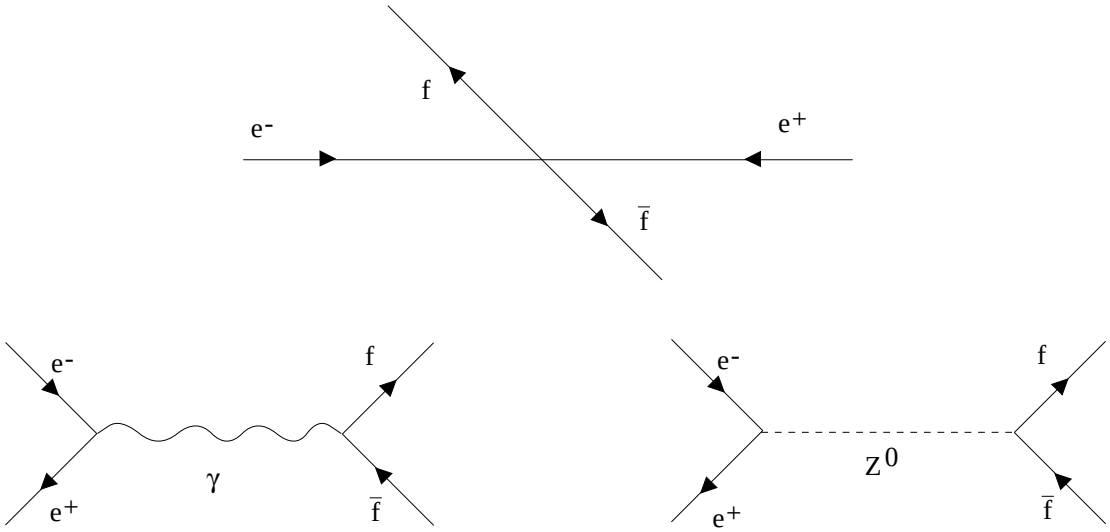

Figure 2.1: Kinematics and lowest order Feynman Diagrams in the multihadron production in Z decay. f and $\bar{f}$ represent fermion pair.

where M_Z is the Z mass, M_W is the W mass. θ_W is the Weinberg angle describing the relative strength of the electromagnetic to the weak coupling. Q_f is the electric charge of the fermion. I_3^f is the third component of the weak isospin of the fermion. G_F is the Fermi coupling constant. c_V and c_A are vector and axial-vector coupling constants. For $M_Z = 91$ GeV and $\sin^2\theta_W = 0.23$, $\Gamma_{Z\to c\bar{c}}$ and $\Gamma_{Z\to b\bar{b}}$ can be calculated as:

$$\Gamma(Z \to c\bar{c}) \approx 280 \text{ MeV}, \ \text{Br}(Z \to c\bar{c}) \approx 12\%, \tag{2.2}$$

$$\Gamma(Z \to b\bar{b}) \approx 360 \text{ MeV}, \ \text{Br}(Z \to b\bar{b}) \approx 15\%. \tag{2.3}$$

The multihadronic decay accounts for 69.9% of Z decay.

The relative ground state b hadron production fractions from the Z resonance are shown in Table 2.3 [2]. The hadron production in Z decay can be described in the following four processes, which are shown in Figure 2.2. At first, primary quarks are produced from Z decay by electron and positron annihilation. This process can be precisely calculated by the electroweak theory. The second process is that the primary quarks radiate

B^+	38.9 ± 1.3 %
B^0	38.9 ± 1.3 %
B_s^0	10.7 ± 1.4 %
Λ_b	11.6 ± 2.0 %
B_c^+	negligible

Table 2.3: b hadron production fraction.

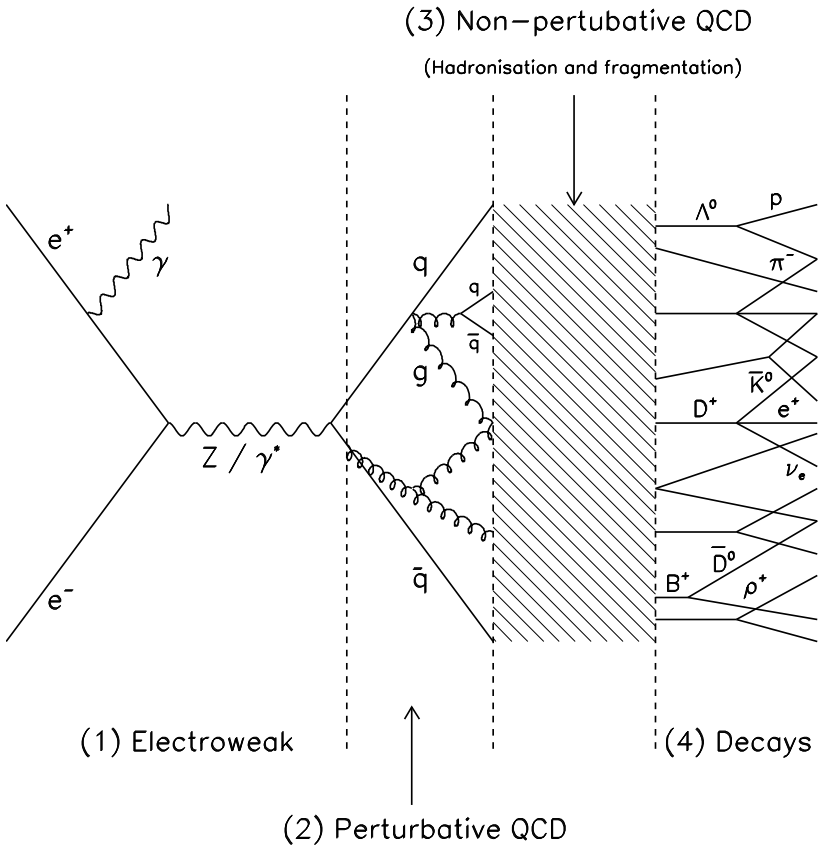

Figure 2.2: The hadron production from annihilation of e^+ and e^- [28].

gluons and gluons can radiate gluons or a quark anti-quark pair. This process is repeated until the parton energy is low relative to the QCD scale parameter. This process can be calculated using perturbation theory. When the parton energy is low relative to the QCD scale parameter, the strong coupling constant is large and hadrons are formed by partons. At this point, perturbation theory can not be applied anymore. Thus phenomenological models have to be used to describe this process, called fragmentation. The last step is that unstable hadrons decay to stable particles according to their decay branching fractions.

The fragmentation functions can be deduced by analyzing $Q \to (Q\bar{q}) + q$. The scaled energy transferred to the hadron $Q\bar{q}$ can be defined as:

$$z = \frac{(E + p_{\parallel})_{Q\bar{q}}}{(E + p_{\parallel})_{Q}}, \tag{2.4}$$

where $(E + p_{\parallel})_{Q\bar{q}}$ is the hadron $Q\bar{q}$ energy plus its longitudinal momentum relative to initial quark direction. $(E + p_{\parallel})_{Q}$ is the primary quark Q energy plus its momentum. z is Lorentz invariant. Several models to describe the z distribution in the fragmentation process are discussed below:

- The Peterson fragmentation function [29]: The Peterson function is mainly used in modeling heavy quark fragmentation. The heavy quark Q with momentum p evolves to a hadron $Q\bar{q}$ with momentum zp and a light quark q with momentum (1 - z)p. The transition amplitude is proportional to the inverse of the energy transfer ΔE^{-1}, where

$$\Delta E = \sqrt{m_Q^2 + p^2} - \sqrt{m_{Q\bar{q}}^2 + (zp)^2} - \sqrt{m_q^2 + ((1-z)p)^2}. \tag{2.5}$$

  Assuming that the heavy quark mass is small compared to the momentum p, ΔE can be simplified as:

$$\Delta E \sim 1 - \frac{1}{z} - \frac{m_q^2}{m_Q^2(1-z)}. \tag{2.6}$$

Using

$$f(z) \propto \frac{1}{z(\Delta E)^2}, \tag{2.7}$$

where the factor $\frac{1}{z}$ arises from longitudinal phase space, the Peterson function can be obtained:

$$f(z) = \frac{N}{z(1 - \frac{\epsilon_Q}{1-z} - \frac{1}{z})^2}, \tag{2.8}$$

where N is the normalization factor, $\epsilon_Q = \frac{m_q^2}{m_Q^2}$. m_Q is the heavy quark mass and m_q is the light quark mass.

- The fragmentation model of Collins and Spiller [30]: The heavy quark fragmentation function and heavy meson structure function should be the same when $z \to 1$. For $z \to 1$, the heavy meson structure function goes as 1 - z, whereas the Peterson function goes as $(1 - z)^2$. This difference becomes important only for very high quark mass. Collins and Spiller suggest another fragmentation function, where the fragmentation function becomes 1 - z as $z \to 1$:

$$f(z) = N(\frac{1 - z}{z} + \frac{2 - z}{1 - z}\bar{\epsilon})(1 + z^2)(1 - \frac{\bar{\epsilon}}{1 - z} - \frac{1}{z})^{-2}, \tag{2.9}$$

where N is the normalization factor. $\bar{\epsilon}$ is a parameter which is proportional to the inverse mass of the heavy quark.

- The Kartvelishvili *et al.* fragmentation model [31]: Kartvelishvili, Likhoded and Petrov discussed another fragmentation function for charmed mesons:

$$f(z) = Nz^{\alpha}(1 - z), \tag{2.10}$$

where N is the normalization factor, α is a free parameter.

- The Lund symmetric fragmentation model [32]: The Lund symmetric model is mainly used for light quark fragmentation and can be written as:

$$f(z) = N\frac{(1 - z)^a}{z}e^{\frac{-b(M_H^2 + p_t^2)}{z}}, \tag{2.11}$$

where a and b are free parameters. M_H is the mass of the hadron. p_t is the hadron transverse momentum with respect to the string direction in the Lund symmetric fragmentation model.

The z value can not be directly measured from experiments. Instead an accessible variable, the scaled energy of the hadron, $x_E = E_{hadron}/E_{beam}$, is used. Here E_{hadron} is the measured energy of the hadron and E_{beam} is the incident beam energy.

2.3 *b* hadron semileptonic decay

Semileptonic decays of B mesons have been extensively studied experimentally and theoretically. The study of *b* hadron semileptonic decay can help us understand the weak interaction and strong interaction in the Standard Model and is used to measure the fundamental parameters in the Standard Model. The *b* semileptonic decay width can be calculated from the electroweak theory and QCD. There are large theoretical uncertainties for the non-perturbative QCD effects. Heavy quark effective theory (HQET) [23, 24] is introduced to analyze the meson containing a heavy quark and a light quark to reduce the theoretical uncertainties. In a heavy quark and a light quark system, the momenta of the light quark and the heavy quark have a scale around Λ_{QCD} (0.2 - 0.3 GeV), a typical strong interaction scale. The associated velocity transfer from the light quark to the heavy quark is approximately Λ_{QCD}/m_Q. When the heavy quark mass is far greater than the QCD scale, Λ_{QCD} (0.2 - 0.3 GeV), the heavy quark behaves as a stationary source of a colour field. Spin decouples from the dynamics as the colour magnetic moment is inversely proportional to the heavy quark mass. In HQET, the decay properties of the hadron with a heavy quark are analyzed in terms of an expansion in E/m_Q,

where E is the kinematic energy of the heavy quark. In contrast to calculations from hadron models, the HQET expansion is derived from the fundamental theory of QCD.

In *b* hadron semileptonic decay, the b quark decays to a c quark or u quark via emission of a virtual W^- boson, which subsequently decays to a lepton plus an anti-neutrino. b to c and b to u semileptonic decays are discussed in detail below.

2.3.1 b to c semileptonic decay

The decay rate of b to c semileptonic decay depends upon the CKM matrix element $|V_{cb}|$. $|V_{cb}|$ can be derived from exclusive and inclusive b to c semileptonic decay rates.

2.3.1.1 Exclusive b to c semileptonic decay

The b to c semileptonic decay is dominated by a few resonant states, namely the ground state 1^1S_0 (D), the first excited state 1^3S_1 (D^*) and the higher states 1^3P_2, 1^3P_1, 1^3P_0, 1^1P_1, 2^1S_0 and 2^3S_1 (collectively referred as D^{**}). The matrix element for B semileptonic decay to a charm hadron can be written as [33]:

$$\mathcal{M} = -i\frac{G_F}{\sqrt{2}}V_{cb}\mathcal{L}_\mu\mathcal{H}^\mu, \tag{2.12}$$

where G_F is Fermi coupling constant, $\mathcal{L}_\mu$ is the leptonic current:

$$\mathcal{L}_\mu = \bar{u}_\ell\gamma_\mu(1-\gamma_5)v_\nu, \tag{2.13}$$

and $\mathcal{H}^\mu$ is the hadronic current. $\bar{u}_\ell$ and v_ν are field operators for the lepton and neutrino. $\bar{B} \to D\ell\nu$ decay is a pseudoscalar meson to a pseudoscalar meson decay

and the hadronic current $\mathcal{H}^\mu$ can be written as follows, based on two form factors:

$$\mathcal{H}^\mu = \langle \mathrm{D(k)}|\mathrm{J}^\mu|\bar{\mathrm{B}}(\mathrm{p})\rangle = \mathrm{F}_1(\mathrm{q}^2)((\mathrm{p}+\mathrm{k})^\mu - \frac{\mathrm{M}_\mathrm{B}^2 - \mathrm{M}_\mathrm{D}^2}{\mathrm{q}^2}\mathrm{q}^\mu) + \mathrm{F}_0(\mathrm{q}^2)\frac{\mathrm{M}_\mathrm{B}^2 - \mathrm{M}_\mathrm{D}^2}{\mathrm{q}^2}\mathrm{q}^\mu, \tag{2.14}$$

where q^2 is the four momentum transfer between B meson and D meson. p and k are the four momenta of the B and D mesons. As $\mathrm{q}^\mu \mathcal{L}_\mu = 0$ when the lepton mass is zero, the hadronic current $\mathcal{H}_\mu$ can be simplified as

$$\mathcal{H}^\mu = \mathrm{F}_1(\mathrm{q}^2)((\mathrm{p}+\mathrm{k})^\mu - \frac{\mathrm{M}_\mathrm{B}^2 - \mathrm{M}_\mathrm{D}^2}{\mathrm{q}^2}\mathrm{q}^\mu). \tag{2.15}$$

The differential decay rate for $\bar{\mathrm{B}} \to \mathrm{D}\ell\nu$ can be deduced as:

$$\frac{\mathrm{d}\Gamma}{\mathrm{dq}^2} = \frac{\mathrm{G}_\mathrm{F}^2|\mathrm{V_{cb}}|^2\mathrm{k}^3}{24\pi^3}|\mathrm{F}_1(\mathrm{q}^2)|^2. \tag{2.16}$$

$\bar{\mathrm{B}} \to \mathrm{D}^*\ell\nu$ decay is a pseudoscalar meson to a vector meson decay and the hadronic current $\mathcal{H}^\mu$ can be calculated from four form factors [33], $\mathrm{A}(\mathrm{q}^2)$, $\mathrm{A}_1(\mathrm{q}^2)$, $\mathrm{A}_2(\mathrm{q}^2)$ and $\mathrm{V}(\mathrm{q}^2)$:

$$\mathcal{H}^\mu = \langle \mathrm{D}^*|\mathrm{V}^\mu - \mathrm{A}^\mu|\bar{\mathrm{B}}\rangle, \tag{2.17}$$

with

$$\langle \mathrm{D}^*(\epsilon,\mathrm{k})|\mathrm{V}^\mu|\bar{\mathrm{B}}(\mathrm{p})\rangle = \frac{2\mathrm{V}(\mathrm{q}^2)\epsilon^{\mu\gamma\delta\beta}\epsilon^*_\beta \mathrm{p}_\gamma \mathrm{k}_\delta}{\mathrm{m_B} + \mathrm{m_{D^*}}}, \tag{2.18}$$

$$\langle \mathrm{D}^*(\epsilon,\mathrm{k})|\mathrm{A}^\mu|\bar{\mathrm{B}}(\mathrm{p})\rangle = \mathrm{i}(\mathrm{m_B}+\mathrm{m_{D^*}})\mathrm{A}_1(\mathrm{q}^2)\epsilon^{*\mu} - \frac{\mathrm{iA}_2\mathrm{q}^2(\epsilon\cdot\mathrm{p})(\mathrm{p}+\mathrm{k})^\mu}{\mathrm{m_B}+\mathrm{m_{D^*}}} + \frac{\mathrm{iA}(\mathrm{q}^2)2\mathrm{m_{D^*}}(\epsilon\cdot\mathrm{p})\mathrm{q}^\mu}{\mathrm{q}^2}, \tag{2.19}$$

where ϵ is the D^* polarization vector. q^2 is the four momentum transfer between the B meson and D^* meson. $\mathrm{p_{\bar{B}}}$ and $\mathrm{p_{D^*}}$ are the four momenta for B and D^* mesons. Another form factor A_0 is defined, which will be used later, in terms of $\mathrm{A} + \mathrm{A}_3$ where

$$\mathrm{A}_3 = \frac{(\mathrm{m_B}+\mathrm{m_{D^*}})\mathrm{A}_1 - (\mathrm{m_B}-\mathrm{m_{D^*}})\mathrm{A}_2}{2\mathrm{m_{D^*}}}. \tag{2.20}$$

In the heavy quark limit, the form factors in B to D and B to D^* semileptonic decay are related and can be expressed by the Isgur-Wise function [34] $\xi(\omega)$, which contains all the nonperturbative QCD effects:

$$F_1(q^2) = V(q^2) = A_0(q^2) = A_2(q^2), \tag{2.21}$$

$$A_2(q^2) = A_1(q^2)(1 - \frac{q^2}{(m_B + m_H)^2}) = \xi(\omega)\frac{m_B + m_D}{2\sqrt{m_B m_H}}, \tag{2.22}$$

with

$$\omega = v_B \cdot v_H = \frac{m_H^2 + m_{B^0}^2 - q^2}{2m_{B^0} m_H}, \tag{2.23}$$

where H represents the D or D^* meson as appropriate. v_B and v_H are four velocities for B and H mesons.

ISGW, ISGW** and ISGW2 models are used to describe b semileptonic decay and are discussed below.

ISGW: Isgur, Scora, Grinstein and Wise (ISGW) [34] used a non-relativistic approximation in B decay due to the heavy mass of the b quark. The form factor $F(q^2)$ at the minimum recoil of the final state meson, i.e. maximum q^2, can be obtained by solving the Coulomb potential plus linear potential for the ground B state in the Schrödinger equation:

$$V(r) = \frac{-4\alpha_s}{3r} + c + br, \tag{2.24}$$

where $\alpha_s = 0.5$, $c = -0.84$ GeV and $b = 0.18$ GeV/c^2. $F(q^2)$ is modeled to be exponential:

$$F(q^2) \propto F(q^2_{max}) \exp(\frac{q^2 - q^2_{max}}{k q^2_{max}}) \tag{2.25}$$

where k accounts for relativistic effects and is determined to be 0.7 from the measured pion form factor.

The ISGW model predicts the relative fractions of the B $\to$ D$\ell\nu$, B $\to$ D$^*\ell\nu$ and B $\to$ D$^{**}\ell\nu$ to be 27%, 62% and 11% [34]. The lepton spectra for b to c semileptonic decay predicted by the ISGW model and the free quark model are shown in Figure 2.3. For b to c semileptonic decay, the lepton spectrum

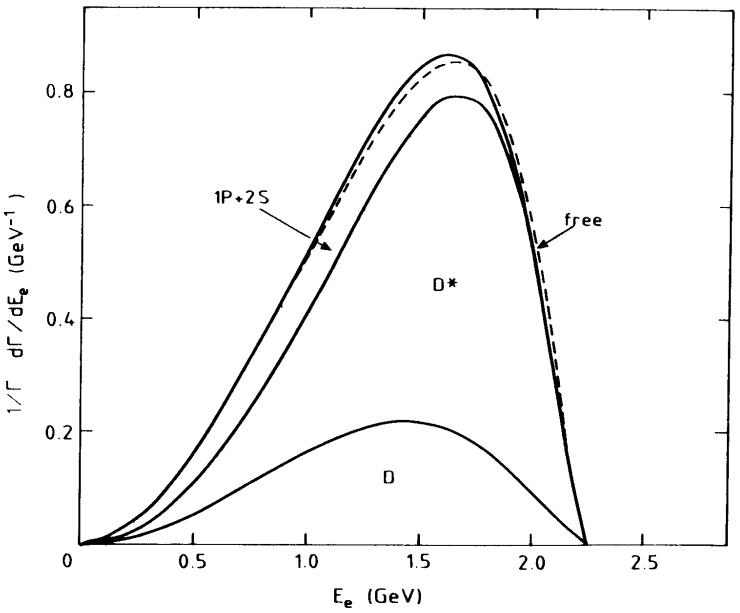

Figure 2.3: The lepton spectrum for b to c semileptonic decay from the ISGW model and free quark model [34].

predicted by the ISGW model is close to that predicted by the free quark model. For b to u semileptonic decay, the lepton spectrum from the ISGW model is much softer than that predicted by the free quark model, which will be discussed in the $b \to X_u\ell\nu$ hybrid model.

ISGW:** Various experiments have measured the sum of exclusive D and D* fractions of the total semileptonic B decay width. The CLEO experiment measured (65 $\pm$ 12)% [35] and the ARGUS experiment measured (60 $\pm$ 10)%

[36] significantly smaller than the 89% predicted by the ISGW model. CLEO therefore increased the D** rate from 11% to 32%, which was referred to as the ISGW** model and better fit the lepton spectrum than the ISGW model.

ISGW2: The ISGW2 model [37] is an update of the ISGW model for the semileptonic meson decay based on the discovery and development of Heavy Quark Symmetry. The Heavy Quark Effective Theory (HQET) treats both the $1/m_Q$ and the perturbative QCD corrections to the extreme Heavy Quark Symmetry limit. In the low-recoil region, the ISGW model is already consistent with the Heavy Quark limit. In high recoil $b \to c\ell\nu$ transitions, ISGW2 improved ISGW by including the constraints imposed by Heavy Quark Symmetry, hyperfine distortions of wavefunctions and form factors with more realistic high recoils behaviors. The ISGW2 model predicts the relative fractions of the $B \to D\ell\nu$, $B \to D^*\ell\nu$ and $B \to D^{**}\ell\nu$ to be 29%, 61% and 10%, which is close to the ISGW model.

In the exclusive method, the value of $|V_{cb}|$ can be extracted by studying the decay rate of $\bar{B}^0 \to D^{*+}\ell^-\bar{\nu}$ as a function of the recoil kinematics of the D^{*+} meson. In b to c semileptonic decay, both b quark and c quark are heavy and the HQET can be applied. Using HQET, the differential partial width for $\bar{B}^0 \to D^{*+}\ell^-\bar{\nu}$ is given by [7]:

$$\frac{d\Gamma(\bar{B} \to D^{*+}\ell^-\bar{\nu})}{d\omega} = \mathcal{K}(\omega)\mathcal{F}^2(\omega)|V_{cb}|^2 \ , \tag{2.26}$$

where $\mathcal{K}(\omega)$ is a known phase space term and $\mathcal{F}(\omega)$ is the hadronic form factor for this decay. m_{B^0} and $m_{D^{*+}}$ are the mass of B^0 and D^{*+}. q^2 is the four momentum transfer between B^0 and D^{*+}.

Although the shape of the form factor $\mathcal{F}(\omega)$ is not known, its magnitude at zero recoil, $\omega = 1$, can be estimated using HQET. In the heavy quark limit, $\mathcal{F}(\omega)$

coincides with the Isgur-Wise function which is normalised to unity at the point of zero recoil. Corrections to $\mathcal{F}(1)$ have been calculated to take into account the effects of finite quark masses and QCD corrections, yielding the value and theoretical uncertainty $\mathcal{F}(1)$=0.913± 0.042 [7].

$\mathcal{F}(\omega)$ is unknown. There are various parameterizations of $\mathcal{F}(\omega)$. A simple one is $\mathcal{F}(\omega) = \mathcal{F}(1)(1-(\omega-1)\rho^2)$ using the Taylor expansion at $\omega = 1$, as the range of ω is fairly small, between 1 and 1.5, in $\bar{\mathrm{B}}^0 \to \mathrm{D}^{*+}\ell^-\bar{\nu}$ decay.

2.3.1.2 Inclusive b to c semileptonic decay

In the inclusive b to c semileptonic decay, the final states refer to all possible final-state *c* hadrons, ignoring the detailed breakdown among the individual modes in b semileptonic decay. Experimentally, only a lepton is identified and this eliminates the difficulty to construct each daughter hadron individually. The CLEO experiment fit the electron spectrum to the sum of the shape from $\mathrm{b} \to \mathrm{ce}\bar{\nu}_\mathrm{e}$ and $\mathrm{b} \to \mathrm{c} \to \mathrm{e}$ decay [38] in the region 0.6 - 2.6 GeV/c. The electron momentum is required to be greater than 0.6 GeV/c to eliminate electrons from primary charm quarks. The lepton spectra of $\mathrm{b} \to \mathrm{ce}\bar{\nu}_\mathrm{e}$ and $\mathrm{b} \to \mathrm{c} \to \mathrm{e}$ decay from the CLEO measurement are shown in Figure 2.4. The $\mathrm{Br}(\mathrm{b} \to \mathrm{Xe}\nu)$ from CLEO measurements is $(10.49 \pm 0.17 \pm 0.43)\%$, where X refers to a u quark or a c quark. The ARGUS collaboration used a charge correlation method to separate the contributions from $\mathrm{b} \to \mathrm{ce}\nu$ and $\mathrm{b} \to \mathrm{c} \to \mathrm{e}$ and yielded $\mathrm{Br}(\mathrm{b} \to \mathrm{X}\ell\nu)$ as $(9.7 \pm 0.5 \pm 0.4)\%$.

The inclusive b to c semileptonic decay rate can be written as following:

$$\Gamma = \frac{\mathrm{G_F^2 m_b^5}}{192\pi^3}|\mathrm{V_{cb}}|^2 \mathrm{z_0}(\frac{\mathrm{m_c^2}}{\mathrm{m_b^2}})\eta_{\mathrm{QCD}}, \tag{2.27}$$

with

$$\mathrm{z_0(x)} = 1 - 8\mathrm{x}^2 + 8\mathrm{x}^6 - \mathrm{x}^8 - 24\mathrm{x}^4 \ln \mathrm{x}, \tag{2.28}$$

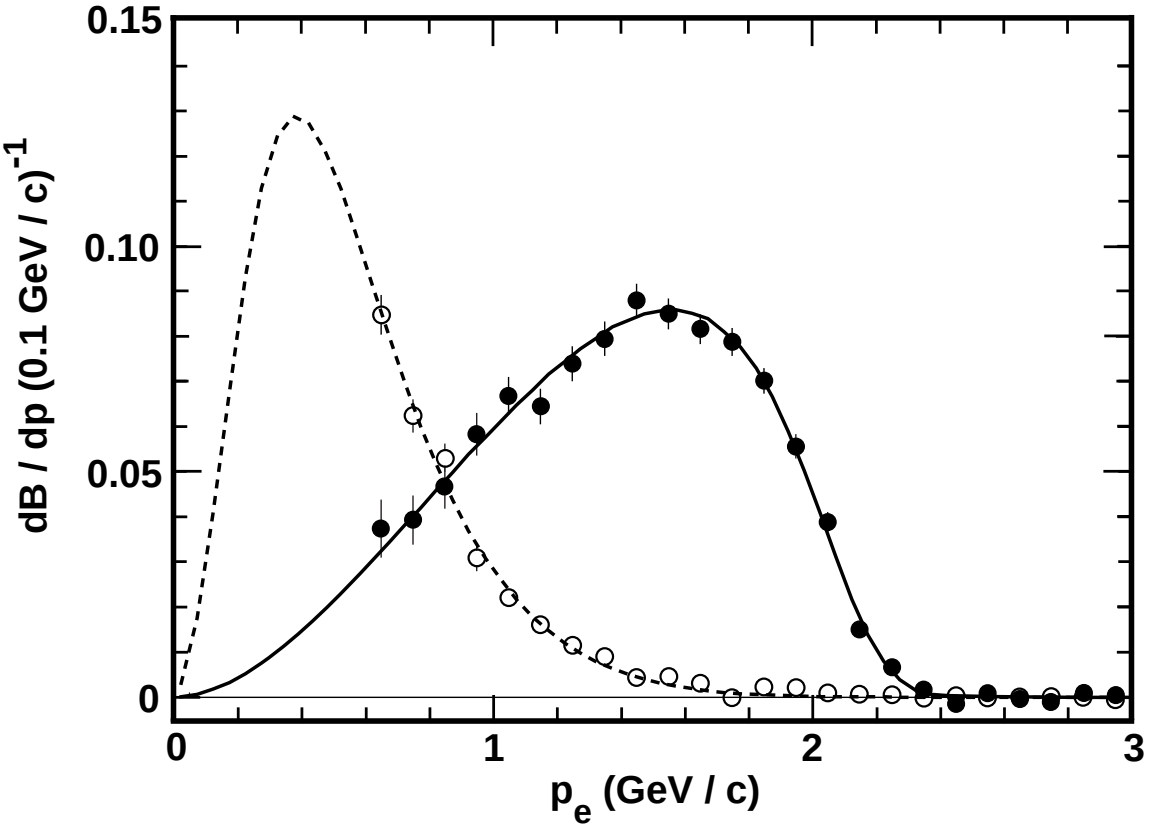

Figure 2.4: Lepton spectra from b $\to$ c e $\bar{\nu}_e$ (filled circles) and b $\to$ c $\to$ e (open circles) from CLEO data [38]. The curves show the best fit to the modified ISGW model with 23% B to D** semileptonic decay.

where m_b and m_c are the b quark and c quark mass. η_{QCD} is a QCD correction factor. $\Gamma/|V_{cb}|^2$ can be deduced from the combined calculations of Ball *et al.* and Shifman *et al.* [39, 40]:

$$\frac{\Gamma}{|V_{cb}|^2} = (42.3 \pm 4.2)\ \mathrm{ps}^{-1}. \tag{2.29}$$

Using the average of $\mathrm{Br}(b \to X\ell\nu)$ from CLEO and ARGUS measurements and subtracting the contribution from $b \to u\ell\nu$, $|V_{cb}|$ from $\Upsilon(4S)$ measurements can be calculated as $(3.87 \pm 0.09 \pm 0.19) \times 10^{-2}$ [2].

The average of $\mathrm{Br}(b \to X\ell\nu)$ from the four LEP experiments at the Z resonance is $(10.56 \pm 0.11 \pm 0.18)\%$ [5, 41, 42, 43, 44]. The LEP experiments use hemisphere b tagging techniques to select high purity samples of b hadrons. The opposite hemisphere is then searched for high momentum lepton candidates and the fraction of these samples which result from semileptonic b decay are determined using a variety of techniques. The precision of these measurements is limited by the modeling uncertainties in the semileptonic decay lepton momentum spectra.

The combined LEP result [5] for $|V_{cb}|$ from $\mathrm{Br}(b \to X_c\ell\nu)$ using Heavy Quark Expansion [45] is:

$$|V_{cb}| = 0.0411 \left(\mathrm{Br}(b \to X_c\ell\nu)\frac{1.55}{0.105}\right)^{\frac{1}{2}} (1 - 0.024\frac{\mu_\pi^2 - 0.5}{0.2})(1 \pm 0.025_{\mathrm{QCD}} \pm 0.035_{m_b}), \tag{2.30}$$

where μ_π^2 is the average of the square of the b quark momentum in the b hadron. Using Equation 2.30, $|V_{cb}|$ can be derived from LEP average $\mathrm{Br}(b \to X\ell\nu)$ after subtracting the contribution from $b \to u\ell\nu$ and the value is $(4.07 \pm 0.05 \pm 0.24) \times 10^{-2}$ [5], where the first uncertainty is statistical and the second uncertainty is systematic.

2.3.2 b to u semileptonic decay

Exclusive and inclusive b to u semileptonic decays can be used to extract $|V_{ub}|$, a small and least well known element in the CKM matrix. The branching fraction of b to u semileptonic decay is small. The exclusive and inclusive b to u semileptonic decays are discussed below.

2.3.2.1 Exclusive b to u semileptonic decay

Unlike $b \to X_c \ell\nu$, $b \to X_u \ell\nu$ decay is distributed over many exclusive modes with no dominant modes. Because of the isospin symmetry, the following relations hold:

$$\Gamma(B^0 \to \rho^- \ell^+ \nu) = 2\Gamma(B^- \to \rho^0 \ell^- \bar{\nu}), \tag{2.31}$$

$$\Gamma(B^0 \to \pi^- \ell^+ \nu) = 2\Gamma(B^- \to \pi^0 \ell^- \bar{\nu}), \tag{2.32}$$

where Γ is the decay rate.

CLEO has searched for B to π^-, π^0, ρ^-, ρ^0 and ω semileptonic decays [4] from 2 million $\Upsilon(4S) \to B\bar{B}$ decays. Neutral pions are reconstructed by pion decay to two photons. Vector mesons are reconstructed by their decay to two pions. The $b \to X_c \ell\nu$ background is suppressed by requiring the lepton momentum to be greater than 1.5 GeV/c in B to pion semileptonic decay and 2.0 GeV/c in B to vector meson decay. A simultaneous fit to the B meson mass and the energy difference between the beam energy and B meson energy yields the number of decays to charged pions and vector mesons. For the decay rate of $B \to \pi^0 \ell\nu$, the isospin symmetry is used. The branching fractions of $B^0 \to \rho^- \ell^+ \nu$ and $B^0 \to \pi^- \ell^+ \nu$ from recent CLEO measurements [2] are:

$$\mathrm{Br}(B^0 \to \rho^- \ell^+ \nu) = (2.6\ ^{+0.6}_{-0.7}) \times 10^{-4}, \tag{2.33}$$

$$\mathrm{Br}(\mathrm{B}^0 \to \pi^-\ell^+\nu) = (1.8 \pm 0.6) \times 10^{-4}. \tag{2.34}$$

Similar to $\mathrm{B} \to \mathrm{D}\ell\nu$ in Equation 2.14, $\mathrm{B}^0 \to \pi^-\ell^+\nu$ is the transition between a pseudoscalar meson to a pseudoscalar meson semileptonic decay, the hadronic current can be written in terms of two form factors:

$$\mathcal{H}^\mu = \langle\pi(\mathrm{k})|\mathrm{J}^\mu|\bar{\mathrm{B}}(\mathrm{p})\rangle = \mathrm{F}_1(\mathrm{q}^2)((\mathrm{p}+\mathrm{k})^\mu - \frac{\mathrm{M}_\mathrm{B}^2 - \mathrm{M}_\pi^2}{\mathrm{q}^2}\mathrm{q}^\mu) + \mathrm{F}_0(\mathrm{q}^2)\frac{\mathrm{M}_\mathrm{B}^2 - \mathrm{M}_\pi^2}{\mathrm{q}^2}\mathrm{q}^\mu, \tag{2.35}$$

where q^2 is the four momentum transfer between B meson and π meson. p and k are the four momenta for B meson and π meson, respectively.

Similar to $\bar{\mathrm{B}} \to \mathrm{D}^*\ell\nu$ decay, $\mathrm{B}^0 \to \rho^-\ell^+\nu$ is a pseudoscalar meson to a vector meson semileptonic decay. The hadronic current can be written in terms of four form factors as in Equation 2.19, just replacing $\mathrm{m}_{\mathrm{D}^*}$ with m_ρ. The differential decay rate of $\bar{\mathrm{B}} \to \rho\ell\bar{\nu}$ with ρ decay to $\mathrm{P}_1\mathrm{P}_2$ can be written as [14]:

$$\frac{\mathrm{d}\Gamma(\bar{\mathrm{B}} \to \rho\ell\bar{\nu})}{\mathrm{dq}^2} = \frac{\mathrm{G}_\mathrm{F}^2|\mathrm{V}_{\mathrm{ub}}|^2}{192\pi^3\mathrm{m}_\mathrm{B}^2}\mathrm{pq}^2\mathrm{B}(\rho \to \mathrm{P}_1\mathrm{P}_2)(|\mathrm{H}_+(\mathrm{q}^2)|^2 + |\mathrm{H}_-(\mathrm{q}^2)|^2 + |\mathrm{H}_0(\mathrm{q}^2)|^2), \tag{2.36}$$

where p is the ρ meson momentum. $\mathrm{B}(\rho \to \mathrm{P}_1\mathrm{P}_2)$ is the branching fraction for ρ decay decay to $\mathrm{P}_1\mathrm{P}_2$. $\mathrm{H}_+(\mathrm{q}^2)$, $\mathrm{H}_-(\mathrm{q}^2)$ and $\mathrm{H}_0(\mathrm{q}^2)$ are related to helicity +1, -1 and 0 for the ρ meson and can be expressed in terms of the four form factors [14]:

$$\mathrm{H}_\pm(\mathrm{q}^2) = (\mathrm{m}_\mathrm{B} + \mathrm{m}_\rho)\mathrm{A}_1(\mathrm{q}^2) \mp \mathrm{V}(\mathrm{q}^2)\frac{2\mathrm{m}_\mathrm{B}\mathrm{p}}{\mathrm{m}_\mathrm{B} + \mathrm{m}_\rho}, \tag{2.37}$$

$$\mathrm{H}_0(\mathrm{q}^2) = \frac{1}{2\mathrm{m}_\rho\sqrt{\mathrm{q}^2}}((\mathrm{m}_\mathrm{B}^2 - \mathrm{m}_\rho^2 - \mathrm{q}^2)(\mathrm{m}_\mathrm{B} + \mathrm{m}_\rho)\mathrm{A}_1(\mathrm{q}^2) - \frac{4\mathrm{A}_2(\mathrm{q}^2)\mathrm{m}_\mathrm{B}^2\mathrm{p}^2}{\mathrm{m}_\mathrm{B} + \mathrm{m}_\rho}), \tag{2.38}$$

where p is the ρ meson momentum in the B rest frame. From lattice QCD (UKQCD [46]), the differential decay rate of $\bar{\mathrm{B}} \to \rho\ell\bar{\nu}$ near maximum q^2 can be simplified as [7]:

$$\frac{\mathrm{d}\Gamma(\bar{\mathrm{B}} \to \rho\ell\bar{\nu})}{\mathrm{dq}^2} = \frac{10^{-12}\mathrm{G}_\mathrm{F}^2|\mathrm{V}_{\mathrm{ub}}|^2}{192\pi^3\mathrm{m}_\mathrm{B}^3}\mathrm{q}^2\lambda^{1/2}(\mathrm{q}^2)\mathrm{a}^2[1 + \mathrm{b}(\mathrm{q}^2 - \mathrm{q}_{\mathrm{max}}^2)], \tag{2.39}$$

where $\lambda(q^2) = (m_B^2 + m_\rho^2 - q^2)^2 - 4m_B^2 m_\rho^2$. The constants $a = (4.6\ ^{+0.4}_{-0.3} \pm 0.6)$ GeV, $b = (-8\ ^{+4}_{-6}) \times 10^{-2}$ GeV^2 are determined from the lattice calculation.

$|V_{ub}|$ can be extracted from $\Gamma(\bar{B} \to \rho \ell \bar{\nu})$ based on:

$$\frac{\Gamma(\bar{B} \to \rho \ell \bar{\nu})}{|V_{ub}|^2} = \tilde{\Gamma}_{thy}, \tag{2.40}$$

where $\tilde{\Gamma}_{thy}$ is model dependent and is shown in Table 2.4.

Form Factor model	$\tilde{\Gamma}_{thy}(ps^{-1})$
ISGW2 [37]	14.2
UKQCD [46]	16.5
LCSR [47]	16.9
Wise/Ligeti+E791 [48]	19.4
Beyer/Melikhov [49]	16.0

Table 2.4: $\tilde{\Gamma}_{thy}(ps^{-1})$ predictions from different form factor models.

2.3.2.2 Inclusive b to u semileptonic decay

The first evidence of b to u semileptonic decay was reported by the ARGUS and CLEO Collaborations in 1990 [8, 9]. The inclusive method developed by ARGUS and CLEO was used to extract the $b \to X_u \ell \nu$ signal using the difference in the endpoint of the lepton spectrum in $b \to X_u \ell \nu$ and $b \to X_c \ell \nu$. ARGUS measured the ratio between $b \to X_u \ell \nu$ in the lepton spectrum region of 2.3 - 2.6 GeV/c and $b \to X_c \ell \nu$ in the lepton spectrum region of 2.0 - 2.3 GeV/c from $\Upsilon(4S) \to B\bar{B}$ and then used the ACCMM model to expand to the whole lepton spectrum to extract $|V_{ub}/V_{cb}|$ [8]. The CLEO collaboration extracted the signal from the region of the lepton spectrum of 2.2 - 2.6 GeV/c [50] and 2.3 - 2.6 GeV/c [51]. Extraction of

$|V_{ub}/V_{cb}|$ is model dependent. The CLEO Collaboration used the ACCMM model to extract $|V_{ub}/V_{cb}|$ as 0.076 ± 0.008 [50, 51].

In the LEP experiments, the lepton spectrum had to be boosted to the b hadron rest frame. As there is a relatively large uncertainty in the b hadron direction, the endpoint method is not appropriate to LEP experiments. The inclusive methods used in this analysis and other three LEP experiments are to extract $|V_{ub}|$ or $|V_{ub}|/|V_{cb}|$ by using the entire lepton spectrum as well as other kinematic variables. ALEPH and this analysis used a neural network discriminant based on kinematic variables. L3 adopted a sequential cut analysis based on the kinematics of the two leading hadrons produced in the same hemisphere as a tagged lepton. DELPHI used a classification based on the reconstructed hadronic mass, decay topology and presence of secondary kaons.

2.4 The $b \to X_u \ell \nu$ hybrid model

A $b \to X_u \ell \nu$ hybrid model, which combines exclusive and inclusive models, is used to simulate the $b \to X_u \ell \nu$ decay in this V_{ub} analysis.

Several theoretical models have been proposed for the $b \to X_u \ell \nu$ decay. The exclusive bound-state models [34, 37, 52, 53] approximate the inclusive $b \to X_u \ell \nu$ decay spectrum by summing contributions from all the exclusive final states. The exclusive models do not include all the possible exclusive final states nor any non-resonant states and therefore yield an incomplete prediction of the inclusive lepton momentum distribution, especially in the high hadronic invariant mass region. The inclusive free quark models [54, 55, 56, 57, 58] treat the heavy quark as a free quark and the final state as a quark plus gluons. The free quark models are known to give

poor agreement with experiments at low u quark recoil momentum. Therefore, a hybrid model [17] is proposed to model the $b \to X_u \ell\nu$ decay by using the exclusive model in the lower hadronic invariant mass region and using the inclusive model in the higher hadronic invariant mass region. The ISGW2 model [37] is used as the exclusive part of the hybrid model. The ACCMM model [54], combined with the W decay model [59] plus JETSET fragmentation, is used as the inclusive part of the hybrid model. Since the ISGW2 exclusive model includes the exclusive resonant final states 1S, 2S and 1P up to 1.5 GeV/c^2 in the hadronic mass, the boundary between the inclusive and exclusive parts of the hybrid model is placed at the hadronic invariant mass of 1.5 GeV/c^2. The relative normalization of the inclusive and exclusive parts of the hybrid model is determined by the inclusive model. This hybrid model is only applied to the B mesons. There are no theoretical predictions for b to u semileptonic transitions of b baryons. The exclusive transitions of the b baryons in the OPAL tuned JETSET 7.4 [15, 16] are used.

In order to estimate systematic uncertainties due to modeling of the inclusive spectrum, alternative models are also studied. Signal events have been generated also with the QCD universal function [55, 56, 57] and parton [58] models. The invariant mass distribution of the hadronic recoil u$\bar{\text{q}}$ system is shown in Figure 2.5 for the QCD universal function, ACCMM and parton models. The invariant mass distribution of the hadronic recoil u$\bar{\text{q}}$ system for the hybrid model is also shown in Figure 2.5.

2.4.1 b to u inclusive model

In this analysis, the ACCMM model [54] is used as a base model for the inclusive part in the hybrid model. The QCD universal structure function [55, 56, 57] and

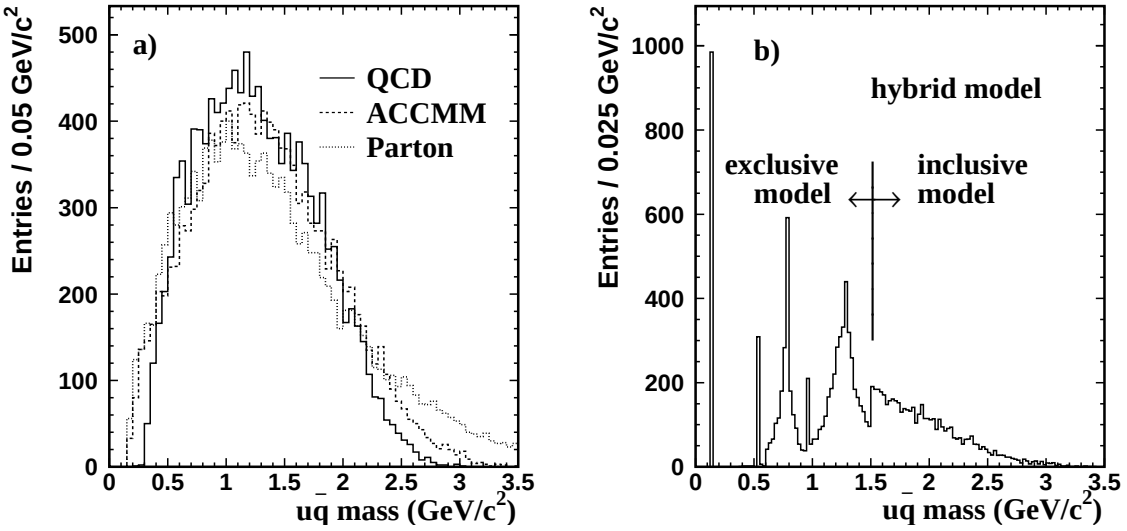

Figure 2.5: **a,b.** The $u\bar{q}$ invariant mass distributions, **a** using the QCD universal function, ACCMM and parton inclusive models, **b** using the hybrid model. Only the portion of the $u\bar{q}$ invariant mass above 1.5 GeV/c^2 from the inclusive model in **a** is used in the hybrid model. The boundary between the exclusive model (left arrow) and the inclusive model (right arrow) in the hybrid model is indicated by the solid line in **b**.

the parton model [58] are used to estimate inclusive model systematic errors in the hybrid model. These inclusive models are described in detail in the following subsections.

2.4.1.1 ACCMM Model

In the ACCMM model, the b quark and the spectator quark momenta in the b hadron rest frame follow a Gaussian distribution:

$$\phi(\mathrm{p}) = \frac{4}{\sqrt{\pi}\mathrm{p}_\mathrm{F}^3} \mathrm{e}^{\frac{-\mathrm{p}^2}{\mathrm{p}_\mathrm{F}^2}}, \tag{2.41}$$

where the width $\mathrm{p_F}$ is known as Fermi momentum [54, 60, 61]. The $\mathrm{p_F}$ values extracted from the fit to the momentum spectrum of leptons from the $\mathrm{b} \to \mathrm{c}\ell\nu\mathrm{X}$ are shown in Table 2.5. A value of $\mathrm{p_F} = 0.5$ GeV/c [61] extracted from the $\mathrm{b} \to \mathrm{c}\ell\nu\mathrm{X}$

Channel	$\mathrm{p_F}$ (GeV/c)	$\mathrm{m_{sp}}$ (GeV/$\mathrm{c^2}$)	Ref
$\mathrm{b} \to \mathrm{c}\ell\nu\mathrm{X}$	0.27 ± 0.04	0.30	[60]
$\mathrm{b} \to \mathrm{c}\ell\nu\mathrm{X}$	$0.51^{+0.08}_{-0.07}$	0.0	[61]
$\mathrm{b} \to \mathrm{s}\gamma$	0.45	0.0	[62]
$\mathrm{B} \to \mathrm{J}/\psi\mathrm{X}$	0.57	0.15	[63]

Table 2.5: Experimental fit results of $\mathrm{p_F}$ and the spectator quark mass $\mathrm{m_{sp}}$ in the ACCMM model

in the CLEO data is used in the $b \to \mathrm{X_u}\ell\nu$ hybrid model.

2.4.1.2 QCD universal structure function

A universal structure function [55, 56, 57] is used to describe the distribution of the light cone residual momentum of the b quark inside the b hadron. The light cone

residual momentum k_+ can be expressed as the difference between the b quark pole mass and its effective mass m_b^* inside the hadron: $k_+ = m_b - m_b^*$. The light-cone structure function is suggested as [55]:

$$f(k_+) = \frac{32}{\pi^2 \bar{\Lambda}}(1-x)^2 e^{\{\frac{-4}{\pi}(1-x)^2\}}\Theta(1-x) \tag{2.42}$$

where $x = \frac{k_+}{\bar{\Lambda}}$, $\bar{\Lambda} = m_B - m_b$. m_B is the b hadron mass and m_b is the b quark pole mass. Θ is the Heaviside step function. $\bar{\Lambda}$ is treated as a free parameter and is predicted by QCD sum rules [64, 65] to be 0.57 GeV.

2.4.1.3 Parton Model

In the parton model [58], the b quark behaves as a free particle carrying a fraction z of the b hadron momentum, i.e. $p_b = zp_B$. The z distribution can be described by the Peterson fragmentation function [29]:

$$f(z) = \frac{Nz(1-z)^2}{((1-z)^2 + \epsilon_b z)^2}, \tag{2.43}$$

where ϵ_b is a free parameter and its experimental value is $0.0047^{+0.001}_{-0.0008}$ [2].

2.4.1.4 Decay kinematics

In the above models, the b quark decay kinematics are required to obtain the decay product u quark's energy and momentum. The u and $\bar{q}$ quarks' energies and momenta are used to obtain the $u\bar{q}$ invariant mass. The b quark decays as $b \to Wu$, and the virtual W boson may be characterized via its effective mass Q^2. The description of the Q^2 distribution is [59]:

$$\frac{d\Gamma(b \to u\ell\nu)}{dx} = \frac{G_F^2 m_b^5 |V_{ub}|^2}{192\pi^3} F_0(x)(1 - \frac{2\alpha_s}{3\pi}F_1(x)), \tag{2.44}$$

where $x^2 = \frac{Q^2}{m_b^2}$ and

$$F_0(x) = 2(1-x^2)^2(1+2x^2),$$

$$F_1(x) = F_0(x)(\pi^2 + 2S_{1,1}(x^2) - 2S_{1,1}(1-x^2)) + 8x^2(1-x^2-2x^4)\ln(x),$$

$$+2(1-x^2)^2(5+4x^2)\ln(1-x^2) - (1-x^2)(5+9x^2-6x^4).$$

$S_{1,1}(x)$ is the Nielsen polylogarithm [66, 67] and m_b is the b quark mass. α_s is the QCD coupling constant at the scale of m_b. α_s has an approximate value 0.24 at the m_b scale. To ensure energy conservation, the effective b quark mass is:

$$m_b^2 = m_B^2 + m_{sp}^2 - 2m_B\sqrt{p_b^2 + m_{sp}^2}. \tag{2.45}$$

The m_B is the *b* hadron mass and m_{sp} is the spectator quark mass. p_b is the b quark momentum. The effective b quark mass depends on p_F and the mass of the spectator quark m_{sp}.

Due to the spin of the W boson, the lepton production angular distribution $\frac{dN}{d\cos\theta}$ is $(1+\cos\theta)^2$ [59]. The angle θ is the lepton direction in the W rest frame with respect to the W direction in the b quark rest frame. The corresponding azimuthal distribution ϕ in the lepton production is isotropic.

2.4.1.5 Implementation of inclusive models

Finally, a string is added between the u quark and the spectator quark for the hadronization of the $u\bar{q}$ system. The string fragmentation in JETSET is used, which will be discussed in Section 2.5.1. The lepton's momentum and energy can be obtained from the virtual W boson's momentum and energy which can be calculated from the b quark decay kinematics. This $b \to X_u \ell\nu$ decay Monte Carlo model is incorporated into JETSET and is referred to as the inclusive model in this analysis.

	$\bar{B}^0 \to X_{u\bar{d}} e \bar{\nu}_e$		$B^- \to X_{u\bar{u}} e \bar{\nu}_e$			
			I = 1		I = 0	
X	mass MeV	partial width	mass MeV	partial width	mass MeV	partial width
1^1S_0	$\pi(140)^+$	0.96	$\pi(140)^0$	0.48	$\eta(547)^0$	0.45
					$\eta'(958)^0$	0.28
$1\ ^3S_1$	$\rho(770)^+$	1.42	$\rho(770)^0$	0.71	$\omega(782)^+$	0.71
$1\ ^3P_2$	$a_2(1320)^+$	0.33	$a_2(1320)^0$	0.16	$f_2(1270)^0$	0.18
$1\ ^1P_1$	$b_1(1235)^+$	1.09	$b_1(1235)^0$	0.54	$h_1(1170)^0$	0.57
$1\ ^3P_1$	$a_1(1260)^+$	0.87	$a_1(1260)^0$	0.43	$f_1(1285)^0$	0.41
$1\ ^3P_0$	$a_0(1450)^{*+}$	0.05	$a_0(1450)^{*0}$	0.02	$f_0(1370)^{*0}$	0.03
$2\ ^1S_0$	$\pi(1300)^+$	0.17	$\pi(1300)^0$	0.08	$\eta(1440)^0$	0.08
$2\ ^3S_1$	$\rho(1450)^+$	0.41	$\rho(1450)^0$	0.20	$\omega(1420)^0$	0.20
total width		5.3		2.6		2.9

Table 2.6: Partial widths for b to u semileptonic decays for B mesons in the ISGW2 model [37]. The notation $N^{2S+1}L_J$ is used here, where N is the energy level quantum number. S, L and J are the spin, the orbital and total angular momentum for the two quark combination. The partial width is in units $10^{13}|V_{ub}|^2$ sec^{-1}.

2.4.2 ISGW2 exclusive model

The ISGW2 model can be used to describe exclusive b to c semileptonic decays as mentioned in Section 2.3.1.1. The ISGW2 model can also be used to describe exclusive b to u semileptonic decays and is used as the exclusive part of the $b \to X_u \ell \nu$ hybrid model. The partial widths for b to u semileptonic decays from B, B_s and B_c mesons in the ISGW2 model are shown in Table 2.6 and Table 2.7. The lepton spectra for $B^- \to X_{u\bar{u}} e \bar{\nu}_e$ predicted by the ISGW2 model are shown in Figure 2.6.

	$\bar{B}_s^0 \to X_{u\bar{s}} e \bar{\nu}_e$		$B_c^- \to X_{u\bar{c}} e \bar{\nu}_e$	
X	mass	partial width	mass	partial width
1^1S_0	$K(494)^+$	0.85	$D(1864)^0$	0.30
$1\ ^3S_1$	$K(892)^{*+}$	1.14	$D(2010)^{*0}$	0.62
$1\ ^3P_2$	$K(1430)^{*+}$	0.28	$D_2(2460)^{*0}$	0.06
$1\ ^3P_1$	$K_{1A}(1270)^+$	1.72	$D_{1A}(2420)^{*0}$	0.62
$1\ ^1P_1$	$K_{1B}(1400)^+$	0.08	$D_1(2420)^{*0}$	0.04
$1\ ^1P_0$	$K_0(1430)^{*+}$	0.04	$D_0(2400)^{*0}$	0.01
$2\ ^1S_0$	$K(1460)^+$	0.45	$D(2580)^0$	0.46
$2\ ^1S_1$	$K(1580)^{*+}$	0.54	$D(2640)^{*0}$	0.40
partial total		5.1		2.5

Table 2.7: Partial widths for b to u semileptonic decay for B_s and B_c in the ISGW2 model [37]. The notation $N^{2S+1}L_J$ is used here, where N is the energy level quantum number. S, L and J are the spin, the orbital and total angular momentum for the two quark combination. The partial width is in units $10^{13}|V_{ub}|^2$ sec^{-1}.

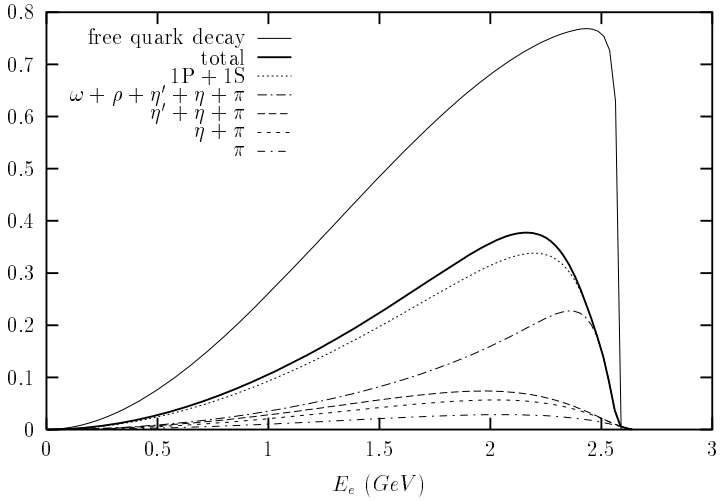

Figure 2.6: The electron energy distribution $(1/\Gamma_{\rm free})(d\Gamma/dE_e)$ *vs* electron energy for $B^- \to X_{u\bar{u}} e \bar{\nu}$ showing contributions of π^0, η, η', ρ^0, ω and the 1P and 2S states [37].

2.5 Signal and background simulation using JETSET

Monte Carlo simulation of multihadron production is model dependent because of the difficulties of calculation of the fragmentation phase of the multihadron production shown in Figure 2.2. The Monte Carlo simulated events in this analysis were generated using the JETSET 7.4 [15] generator, which is described in detail below.

2.5.1 JETSET

JETSET is a Monte Carlo simulation program for jet fragmentation and e^+e^- physics based on the Lund Model. OPAL JETSET is a Monte Carlo simulation generator to simulate the multi-hadronic event production in electron and positron collisions using the OPAL tune [16]. OPAL JETSET describes many aspects of hadronic event production extremely well.

In JETSET, $e^+e^- \rightarrow Z \rightarrow q\bar{q}$ process is based on the Feynman rules of the electroweak theory. The γ and Z interference, initial state radiation and gluon emission of the final quark are considered. The gluon is radiated by primary quarks from Z decay, and later the gluon splits into gluons or quark antiquark pairs. This process can be described by the perturbative theory until the energy density of the system decreases below a fixed level.

Matrix-element and parton shower methods are both used to model the perturbative corrections. In the matrix element method, Feynman diagrams are calculated order by order. The calculation becomes difficult for the higher order Feynman diagrams. In the parton model, one parton decay into two partons or more is used to approach

the multi jet events. The branching probabilities of $q \to q\gamma$, $q \to qg$, $g \to gg$ and $g \to q\bar{q}$, where q represents a quark and g a gluon, are calculated by applying the Altarelli Parisi equations [68].

After the perturbative phase, the coloured partons are transformed into colourless hadrons. There are three main models to describe this fragmentation process, namely string fragmentation (SF), independent fragmentation (IF) and cluster fragmentation. In JETSET, the string fragmentation is used. In string fragmentation, the QCD potential between quarks is described as:

$$V_{QCD} = kr - \frac{4\alpha_s}{3r}, \tag{2.46}$$

where k is a constant and r is the distance between quarks. The string model suggests there is a colour flux tube between quarks. The transverse dimensions of the tube are of typical hadronic sizes, around 1 fm. As the quark q and $\bar{q}$ move apart, the potential energy stored in the string increases. The string may break up by the production of a new $q'\bar{q}'$ pair. Then two colour-singlet systems $q\bar{q}'$ and $q'\bar{q}$ are formed. The string break-up process is repeated until on-mass-shell hadrons remain. The quark flavour production ratio can be predicted by invoking the quantum mechanical tunneling, in which $u : d : s : c = 1 : 1 : 0.3 : 10^{-11}$. Charm and heavier quarks are not expected to be produced in this soft fragmentation, but only in the perturbative parton-shower process.

A large fraction of the particles produced by fragmentation are unstable and subsequently decay into stable particles, which are controlled by the decay table in JETSET. The particle mass and decay properties are well defined in the decay table according to recent measurements.

2.5.2 Signal and background simulations

The b hadron was generated from $e^+e^- \to b\bar{b}$ according to OPAL JETSET [15] generator in the Monte Carlo simulation. For the signal $b \to X_u\ell\nu$ Monte Carlo simulation, the b hadron is forced to decay to $X_u\ell\nu$ according to the branching fractions predicted by the $b \to X_u\ell\nu$ hybrid model. The energies and momenta of X_u, ℓ and ν are calculated from the $b \to X_u\ell\nu$ hybrid model. For background Monte Carlo simulation, the ACCMM model [54] is used to describe the lepton spectrum of $b \to X_c\ell\nu$ and $b \to c \to \ell$ decays. The fragmentation function of Peterson *et al.* [29] is used to describe the b quark and c quark fragmentation. The branching fractions of $B^0 \to D^-\ell^+\nu$, $B^0 \to D^{*-}\ell^+\nu$, $B^+ \to \bar{D}^0\ell^+\nu$, $B^+ \to \bar{D}^{*0}\ell^+\nu$, $\bar{B} \to D^{**}\ell\nu$ and $\Lambda_b \to \Lambda_c X\ell\nu$ are modified to reproduce those given by the Particle Data Group [2]. The Λ_b lepton momentum spectrum corresponding to -56% polarization [69] is used as a central value. The b to u semileptonic decay and background simulated events are passed through the OPAL detector simulation [70] to produce the corresponding response. The production fractions of B^+, B^0, B_s^0 and Λ_b in Z decay are chosen to reproduce those given by the Particle Data Group [2].

Chapter 3

The LEP collider and OPAL detector

The current analysis uses the data taken by the OPAL detector. OPAL is one of the four experiments at the Large Electron and Positron collider (LEP) at CERN. The LEP collider and OPAL detector are described in this chapter. For the OPAL coordinate system, a right handed coordinate system is used, with positive z along the e^- beam direction and x pointing toward the center of the LEP ring. The polar and azimuthal angles are denoted by θ and ϕ, and the origin is taken to be the center of the detector.

3.1 The LEP collider

The LEP collider is located in a 27 km circumference tunnel at CERN, Geneva, Switzerland. It lies underground at a depth between 50 meters and 130 meters below the surface. The four LEP experiments ALEPH, DELPHI, L3 and OPAL are equally spaced around the collider as shown in Figure 3.1. The OPAL detector

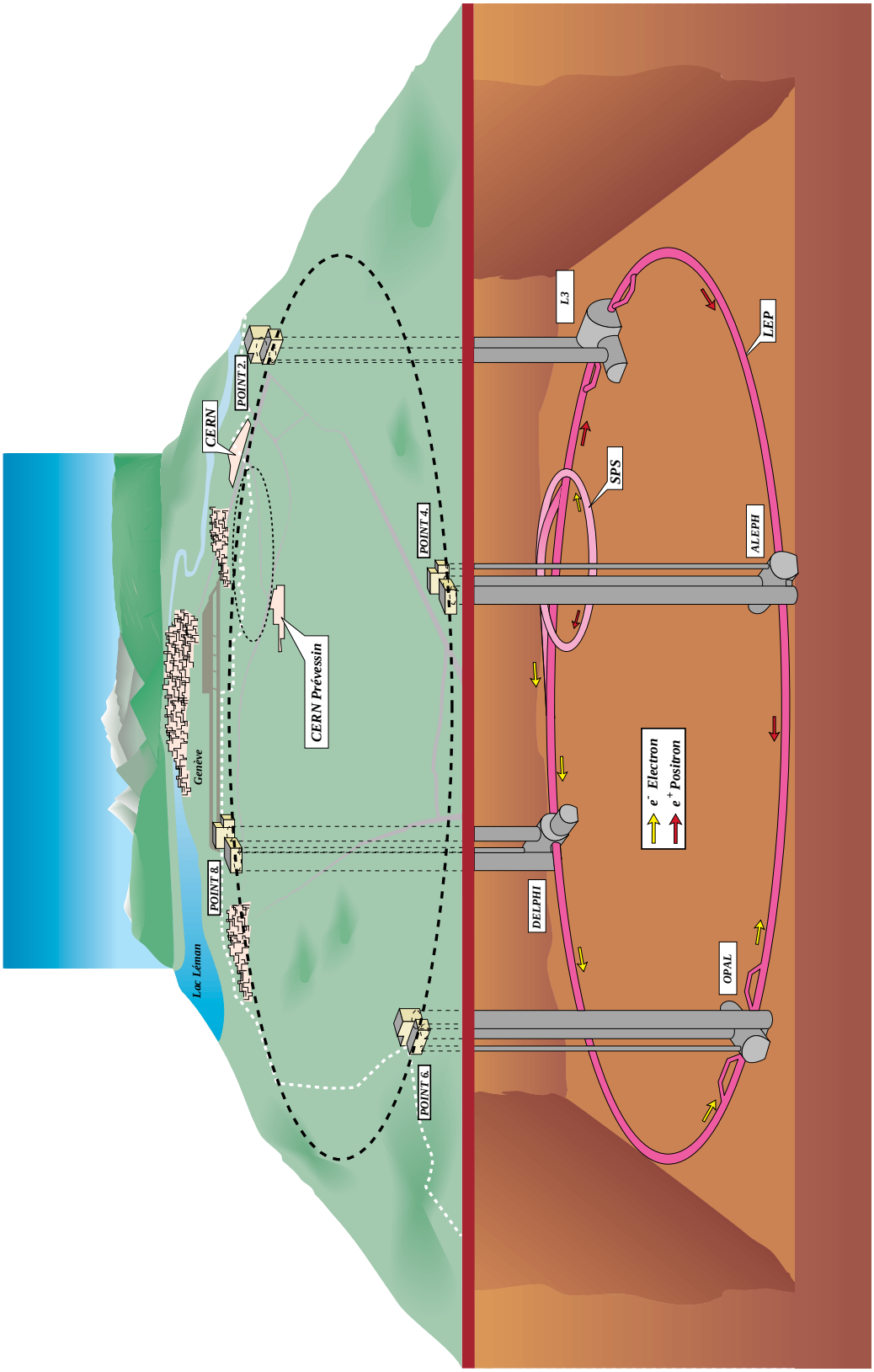

Figure 3.1: The layout of the LEP collider and the four LEP experiments [72].

lies underground 99 m below the surface. The production of LEP beam is shown in Figure 3.2. The LEP injector linac produces electrons and accelerates them to 200 MeV. Some of these electrons strike a tungsten target and produce positrons. Both electrons and positrons are further accelerated to 600 MeV by a second linac and then stored in the Electron Positron Accumulator ring (EPA). Later these leptons are injected into the Proton Synchrotron (PS) and are accelerated to 3.5 GeV. Electrons and positrons are then passed on to the Super Proton Synchrotron (SPS) and further accelerated to 20 GeV before injection into LEP. The LEP collider

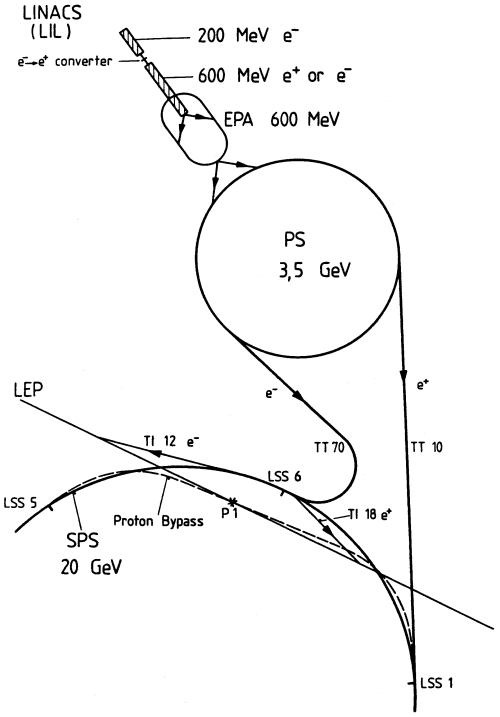

Figure 3.2: The layout of the CERN injector system for the LEP ring [73].

began to operate in 1989 and was shut down in November, 2000. The LEP operation was divided into two phases:

LEP I (1989-1995): LEP I operated in the center mass of around 91 GeV and was designed for the study of the Z boson. The current analysis uses LEP I data.

LEP II(1996-2000): LEP II was used to search for possible new particles. In 1997, LEP operated at a center of mass energy exceeding 160 GeV and produced the first observation of W^+W^- pair production.

3.2 The OPAL detector

The OPAL detector [71], i.e Omni Purpose Apparatus for LEP, is one of the four multi purpose detectors at LEP. The structure of the OPAL detector is shown in Figure 3.3.

The OPAL detector is about 12 m long, 12 m high and 12 m wide and attains almost 4π coverage by closing the barrel with endcap detectors. The main features of the detector are:

- the reconstruction of charged particle tracks inside a magnetic field enabling a measurement of momentum, particle identification (by dE/dx) and the reconstruction of primary and secondary vertex positions;
- the identification of electrons and photons together with a measure of their energy via electromagnetic shower detection;
- the measurement of hadronic energy by total absorption;
- the detection of Bhabha scattering ($e^+e^- \rightarrow e^+e^-$) events at low angles with respect to the beam line, providing a measurement of the absolute luminosity.

The OPAL sub-detectors are discussed in the following sections.

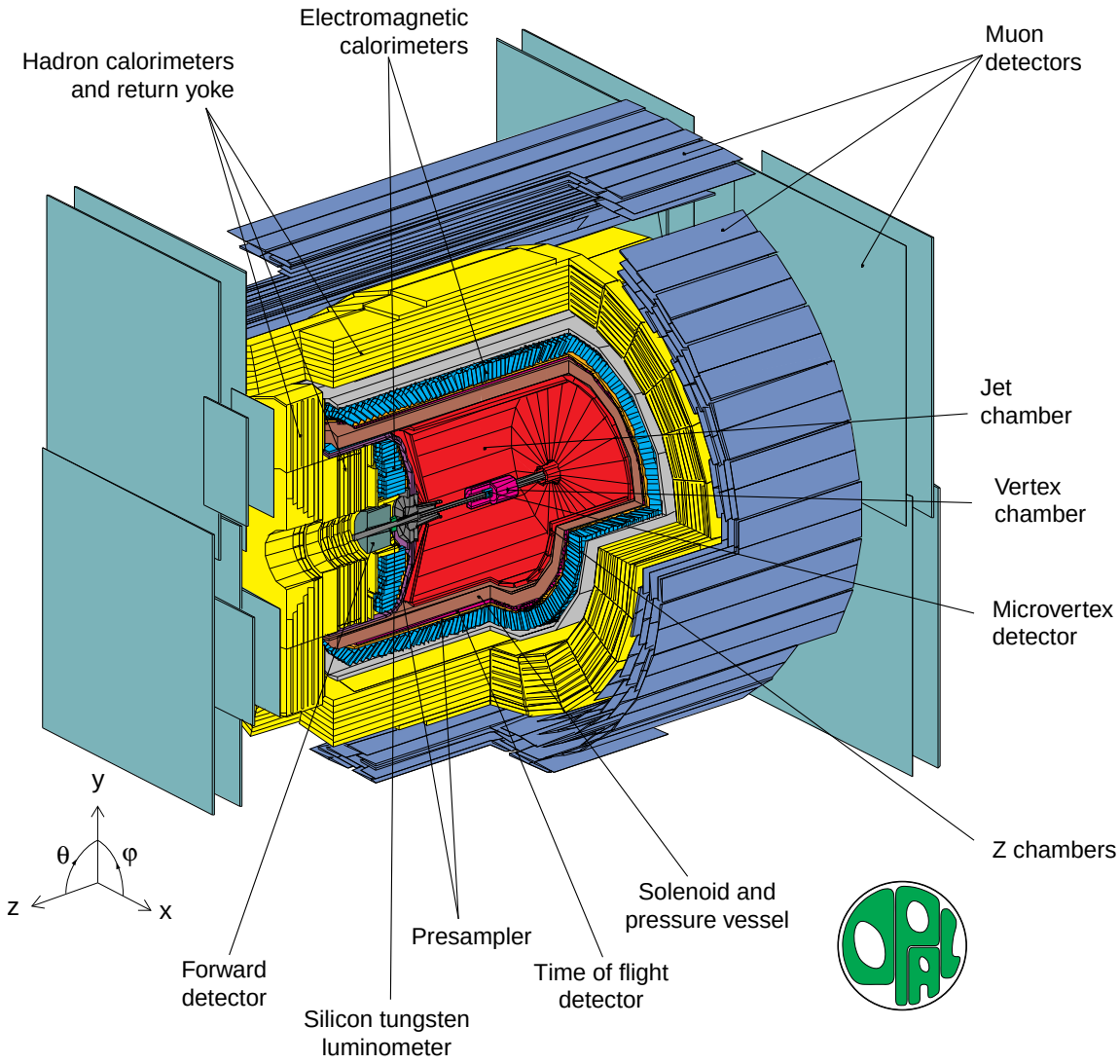

Figure 3.3: The OPAL detector [74].

3.2.1 Beampipe

The OPAL beampipe, which is shown Figure 3.4, consists of an inner aluminum tube covered by layers of carbon fiber epoxy of 2.2 mm thickness. The beampipe is the innermost detector component and is used to isolate the electron and positron beams from the 4 bar pressure gas vessel of the vertex chamber and the jet chamber. Before 1991, the inner radius of the pipe was chosen to be 80.2 mm. In 1991 a second

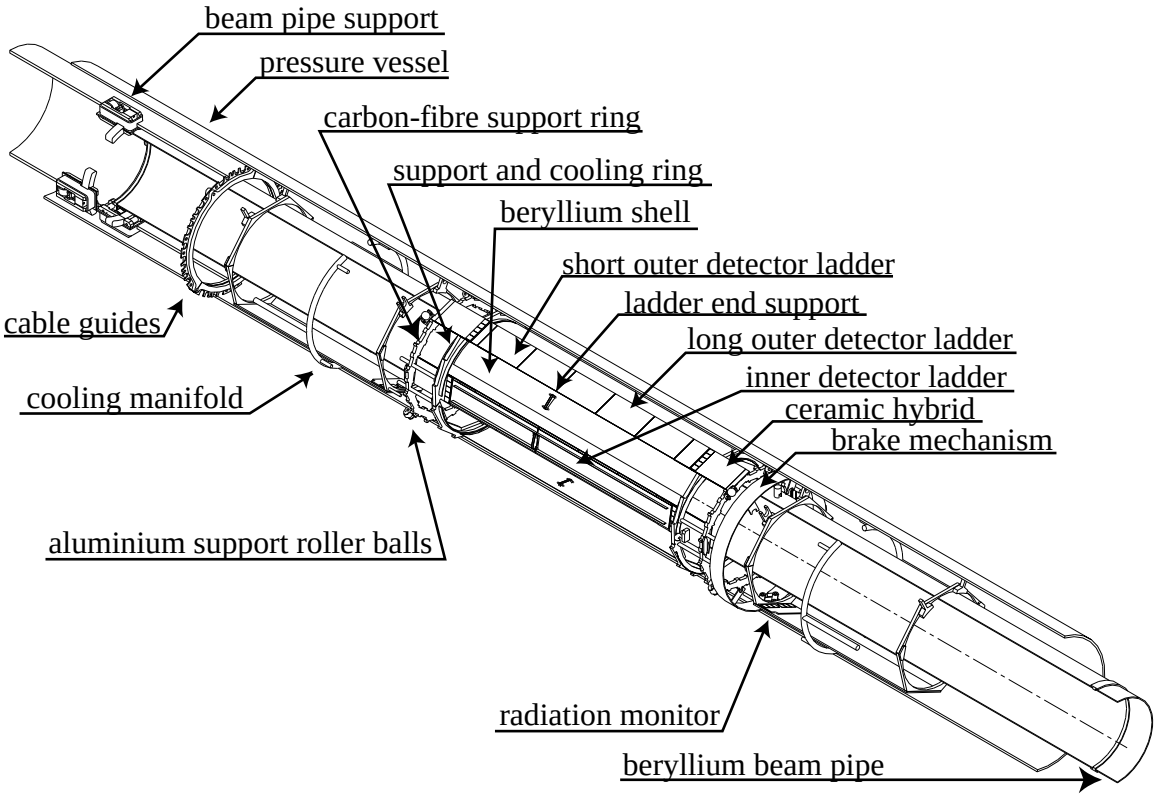

Figure 3.4: The OPAL beampipe structure [75].

beam pipe at a radius of 53.5 mm consisting of 1.1 mm thick beryllium was added and the silicon microvertex detector was inserted between them.

3.2.2 Subdetectors for particle tracking

The tracking of charged particles in the OPAL detector uses information from the silicon microvertex detector [75], the central vertex chamber [76], the jet chamber [77], the z chambers [78] and the muon chamber [79]. The silicon microvertex detector collects the ionization charges generated by charged particles passing through the silicon wafers and measures the track position. The central vertex chamber, the jet chamber, the z chambers and the barrel muon chambers are all gaseous drift chambers. In drift chambers an electric field causes the ionized electrons to drift towards the anode field wires. The ionizing particle position can be detected by measuring the time that electrons need to reach the anode wire, from the moment that the ionizing particle traverses the detector. The endcap muon chambers use streamer tubes. Streamer tubes work in a similar manner to drift chambers but operate in a higher electric field. These subdetectors for the particle tracking are described in detail below.

3.2.2.1 The silicon microvertex detector

The B meson decay length is of the order of a few millimeters. With the silicon microvertex detector, the B meson decay point can be precisely measured.

The silicon microvertex detector [75] consists of 25 ladders arranged in two barrels of inner radius of 6 cm and outer radius of 7.5 cm, which is shown in Figure 3.5. The inner layer consists of 11 ladders and the outer layer of 14 ladders. Each ladder is 18 cm long and consists of 3 silicon microstrip wafers (3 cm $\times$ 6 cm) daisy chained together. Each detector has 629 readout strips. These strips are oriented along the beam axis and have a 50 μm readout pitch in order to measure coordinates in the r $-$ ϕ plane with an intrinsic resolution of about 5 μm. The absolute resolution for

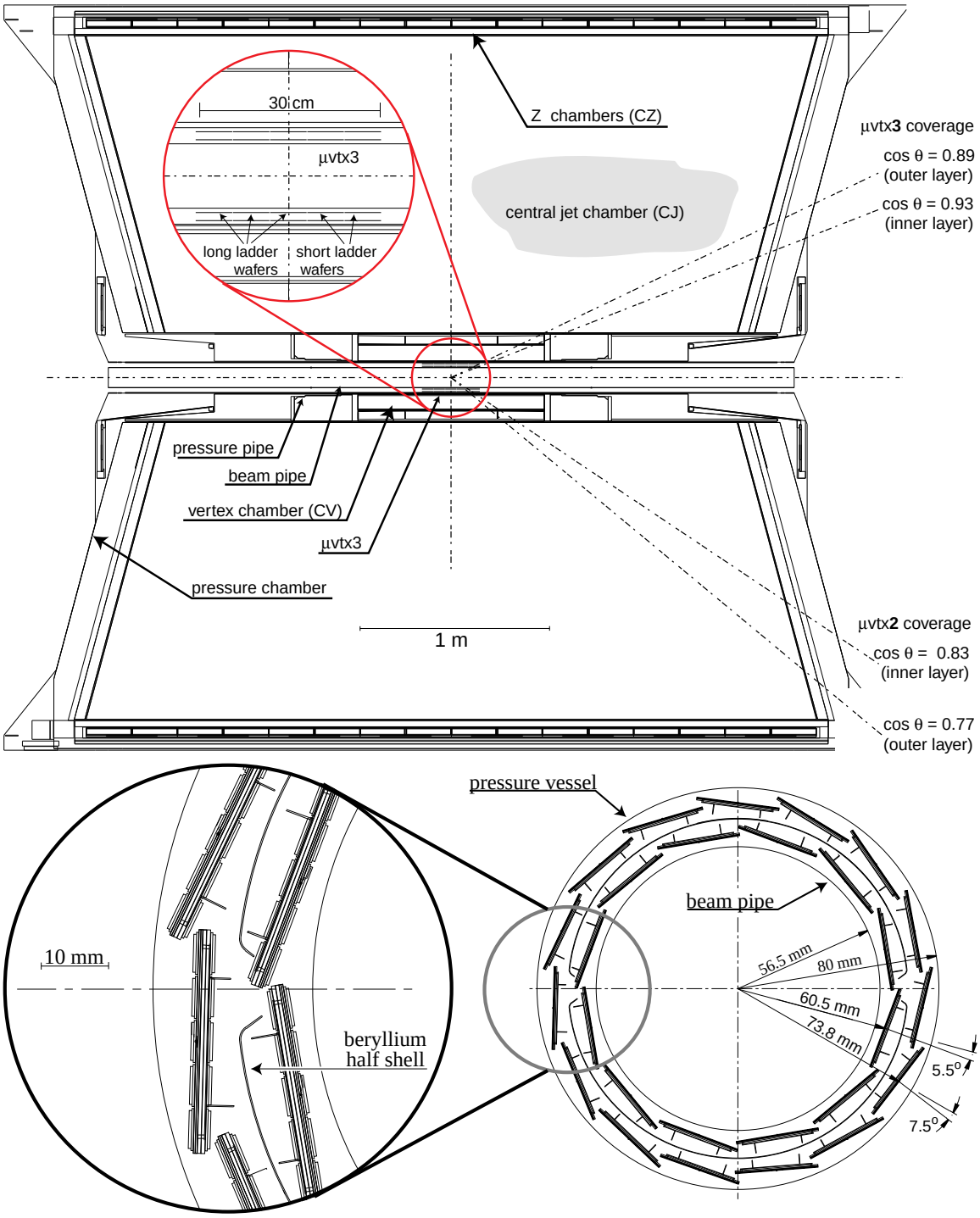

Figure 3.5: The structure of the OPAL silicon microvertex detector [75].

the hit position in event reconstruction is 10 μm. The hit efficiency for the ladder was measured with $Z \rightarrow \mu^+\mu^-$ events to be 97%. The first silicon microvertex detector, μvtx1 was installed in OPAL in 1991 and had readout in the $r-\phi$ plane only. The single hit coverage in ϕ is almost 100%. In 1993 an upgraded detector μvtx2 was installed that had $r-\phi$ and $r-z$ wafers glued back to back, resulting in polar coordinate acceptance to $|\cos\theta| < 0.83$ for the inner barrel and $|\cos\theta| < 0.77$ for the outer barrel. In 1995, the detector was further upgraded to μvtx3. The number of ladders for the inner layer and outer layer was increased to 12 and 15 respectively. The outer layer was also extended from 3 wafers to 5 wafers by an addition of a layer of 2 wafer ladders at the $r-z$ end. In 1996, 2 wafer ladders were added to the inner layer extending polar coordinate acceptance to $|\cos\theta| < 0.89$ for the inner layer.

3.2.2.2 The central vertex chamber

The central vertex chamber [76] is designed to provide precise tracking capabilities for the reconstruction of secondary vertices. The central vertex chamber consists of two 1.0 m cylindrical drift chambers with 36 sectors azimuthally each. The inner chamber contains the axial sectors, where each sector contains a plane of 12 sense wires strung parallel to the beam direction. The wires range radially from 103 mm to 162 mm at a spacing of 5.3 mm. The outer chamber contains the stereo sectors each containing a plane of 6 sense wires inclined at a stereo angle of around 4 degrees. The stereo wires lie between the radii 188 mm and 213 mm at a spacing of 5 mm. These chambers are operated with a gas mixture of 88% argon, 9.4% methane and 2.6% isobutane at a pressure of 4 bars. The precise measurement of the drift time onto axial sector sense wires provides a position resolution of 50

microns in the r - ϕ plane. Measuring the time difference between signals at two ends of the anode wires allows a fast but relatively coarse z coordinate measurement which is used by the OPAL track trigger in a pattern recognition. A more precise z measurement is made by combining axial and stereo drift time information offline.

3.2.2.3 The jet chamber

The central jet chamber [77] is designed to provide precise tracking capabilities for the reconstruction of jet-like events. The central jet chamber is a cylindrical drift chamber of length 4 m with an outer (inner) diameter of 3.7 (0.50) m respectively. The chamber is divided into 24 identical sectors each containing a sense wire plane of 159 wires strung parallel to the beam direction. Each wire is read out at both ends with a 100 MHz flash ADC. The coordinates of wire hits in the r - ϕ plane are determined from a measurement of drift time. The central jet chamber measures the three-dimensional coordinates of charged tracks, the particle momentum and the particle energy loss in the gas volume. The resolution in the r - ϕ plane is 160 μm. The z coordinate is measured by collecting the charge at each end of a wire, which produces a resolution of 6.2 cm. The jet chambers are operated with the same gas mixture as the central vertex chamber.

3.2.2.4 The z chambers

The z chambers [78] provide a precise measurement of the z coordinate of tracks as they leave the jet chamber. The z chambers consist of a layer of 24 drift chambers, each 400 cm long, 50 cm wide and 5.9 cm thick covering 94% of the azimuthal angle and the polar angle range from 44 to 136 degrees. Each chamber is divided into 8 cells of 50 cm $\times$ 50 cm in the z direction, with each cell containing 6 sense wires

spaced at 0.4 cm and with a stagger of $\pm$ 250 μm in order to resolve the left-right ambiguity. The chambers use the same gas as the jet chamber with a uniform field of 800 V/cm over the full drift distance of 25 cm in z. A FADC system is employed to determine the drift distance and a charge division technique is used to give a coarse ϕ measurement.

3.2.2.5 Magnet

The OPAL magnet consists of a solenoid and an iron return yoke. The solenoid was constructed with a water cooled coil of aluminum and glass-epoxy. The magnetic field distribution has to satisfy two main requirements:

- high uniformity through the central detector volume. The central detector refers to the silicon microvertex detector, the central vertex detector, the jet chamber and the z chambers. The field in the central detector region is measured to be 0.435 T produced by 7000 A current and to be uniform within 0.5% over the volume of the central detector. The solenoid and pressure vessel together represent about 1.7 radiation lengths of material.
- a magnetic field not exceeding a few tens of Gauss in the angular region between the solenoid and the iron yoke to facilitate the operation of photo multiplier tubes in surrounding sub-detectors. For the OPAL magnet, the stray field outside the solenoid is below 0.01 T because of the soft iron return yoke.

3.2.2.6 The muon chambers

The outermost of the OPAL detectors are the muon chambers [79]. The muon detector consists of a barrel and two endcaps and covers the iron yoke almost

completely. Particles which reach the muon chambers have to traverse 7 interaction lengths (for pions) and therefore the tracks in the central tracking system matched to muon chamber hits can be identified as muons. The probability for an isolated pion of 5 GeV/c being misidentified as a muon is less than 1%.

The barrel part of the muon detector consists of 110 large-area drift chambers divided into four modules. Each chamber is 120 cm wide and 9 cm deep. Two modules, each with 44 chambers are mounted on each side of the barrel. The remaining two modules, contain 10 chambers in the top module and 12 chambers in the bottom module, which close the gap and provide full coverage in ϕ. The hit in z, with a resolution of 0.2 cm in the muon chamber, can be obtained by measuring the time differences at each end of the sense wires. The resolution in r - ϕ is 0.15 cm using drift time information. The barrel part of muon chambers covers $|\cos\theta| < 0.68$.

The endcap muon detectors cover the angular range $0.67 < |\cos\theta| < 0.985$. An area of about 150 m^2 at the end of the OPAL detector is covered with four layers of limited streamer tubes which are perpendicular to the beam axis. Each endcap consists of eight quadrant chambers (6 m $\times$ 6 m) and four patch chambers (3 m $\times$ 2.5 m). Each chamber consists of two layers of streamer tubes, spaced by 1.9 cm, one layer having vertical wires and the other horizontal wires. The position resolution in x and y coordinates is 0.1 cm.

3.2.2.7 Performance of the tracking system

The reconstructed tracks are characterized using the following five parameters, where the point of closest approach is with respect to the origin:

- k, the track curvature, where $|k| = \frac{1}{2\rho}$ and ρ is the radius of curvature of the

track. The sign of k is chosen positive for a particle which is deflected in the direction of increasing ϕ if traveling along the track direction. Positive values of k correspond to a particle with negative charge;

- ϕ_0, the azimuthal angle of the track tangent at the point of closest approach with respect to the x axis;
- d_0, the impact parameter and $d_0 = (\hat{\phi} \times \vec{d}) \cdot \hat{z}$, where $\hat{\phi}$ is the unit track vector at the point of closest approach and $\vec{d}$ is the vector from the origin of the OPAL detector to the origin. $\hat{z}$ is the unit vector along the z axis;
- $\tan\lambda = \cot\theta$, where θ is the polar angle of the track tangent at the point of closest approach;
- z_0, the track z coordinate at the point of closest approach in the r - ϕ plane.

A schematic diagram of these five parameters is shown in Figure 3.6. In the OPAL jet chamber, each hit provides a measurement of the specific energy loss of the charged particle. The dE/dx resolution [80] is:

$$\frac{\sigma(\mathrm{dE/dx})}{\mathrm{dE/dx}} \sim \mathrm{N}^{-0.43}, \tag{3.1}$$

where N is the number of measured dE/dx samples, around 159 for this jet chamber. The dE/dx resolution is measured to be 3.8% for minimum ionizing particles in a jet.

The transverse momentum of the track can be calculated from the measured curvature of the track in the magnetic field. The resolution [81] of the transverse momentum of the track in the jet chamber can be deduced as:

$$\frac{\sigma \mathrm{p_t}}{\mathrm{p_t}} = \sqrt{(0.02)^2 + (0.0015\mathrm{p_t})^2}, \tag{3.2}$$

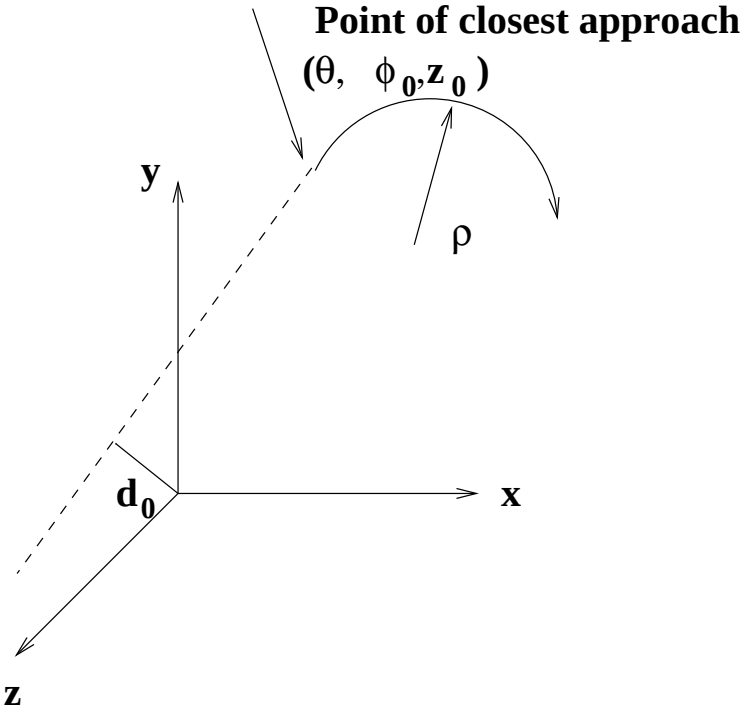

Figure 3.6: A schematic diagram for five parameters describing a track.

where p_t is given in GeV/c. The momentum dependent term of the resolution can be reduced to $0.00128p_t$ by combining the track information of the other central detectors.

3.2.3 Subdetectors for calorimetry

The calorimetry system is designed to measure the particle energies. This is especially important for neutral particles, which are not detected by the tracking detectors. The calorimetry system is composed of the electromagnetic calorimetry and hadron calorimetry, which are described in detail below.

3.2.3.1 The electromagnetic calorimeter

The function of the electromagnetic calorimeter is to detect and identify electrons and photons from tens of MeV to 100 GeV by using lead glass blocks. The electromagnetic calorimeter consists of a barrel, covering angle $|\cos\theta| < 0.82$, and two end cap arrays, covering angle $0.81 < |\cos\theta| < 0.98$. This arrangement, plus two forward lead scintillator calorimeters from the forward detector, makes the OPAL acceptance for electron and photon detection almost 99% of the solid angle. The presence of about 2 radiation lengths of material in front of the calorimeter (due to the solenoid and pressure vessel) results in most electromagnetic showers initiating before reaching the lead glass. Presampling devices are therefore installed in front of the lead glass in the barrel and endcap regions to measure the position and energy of showers to improve overall spatial and energy resolution and give additional γ/π^0 and electron/hadron discrimination. The components of the electromagnetic calorimeter are described in detail below:

Barrel electromagnetic presampler: The barrel electromagnetic presampler [82] consists of 16 chambers forming a cylinder of radius 239 cm and length 662 cm. Each chamber consists of 2 layers of drift tubes operated in the limited streamer mode with the anode wire running parallel to the beam direction. Each layer of tubes contains 1 cm wide cathode strips on both sides at $\pm$ 45 degree to the wire direction. Spatial positions can then be determined by reading out the strips in conjunction with a measurement of the charge collected at each end of the wire to give a z coordinate by charge division. The hit multiplicity is approximately proportional to the energy deposited in the material in front of the presampler allowing the calorimeter shower energy to be corrected with a corresponding improvement in resolution. From test

beam results the presampler can achieve a spatial resolution for electromagnetic showers in the plane perpendicular to the shower direction of 0.6 to 0.4 cm for incident energies in the range of 6 GeV to 50 GeV. The resolution in z for an isolated charged particle is around 10 cm.

Barrel lead glass calorimeter: The electromagnetic barrel lead glass calorimeter [71] consists of a cylindrical array of 9940 lead glass blocks at a radius of 246 cm and covering $|\cos\theta| < 0.82$. The lead glass provides an excellent intrinsic energy resolution ($\sigma_{\mathrm{E}}/\mathrm{E} = 5\%/\sqrt{\mathrm{E}}$ [71], for E in GeV), spatial resolution (around 1 cm) and linear response over a wide dynamic range. To achieve good energy resolution at high energies, shower leakage from the back of the calorimeter must be minimized. This is achieved by using a very dense glass (24.6 radiation lengths) with each block 37 cm in depth and 10 cm $\times$ 10 cm in area. In order to maximize detection efficiency the longitudinal axis of each block is angled to point at the interaction region. The focus of this pointing geometry is slightly offset from the $\mathrm{e^+e^-}$ collision point in order to reduce particle losses in the gaps between blocks. Cerenkov light from the passage of relativistic charged particles through the lead glass is detected by 3 inch diameter photo-tubes at the base of each block. Each photo-tube is shielded from the stray field of the magnet so that operation in magnetic fields up to 100 Gauss is possible with a gain variation of less than 1%. The photomultiplier signals are digitized by charge integrating 15-bit ADCs. The linearity of the ADC was measured to be better than $\pm$ 1 count over the full range of the core channel. In order to ensure the quality of the gain calibration for each phototube over long time periods, a gain monitoring system using a Xenon light source is employed.

Endcap electromagnetic presampler: The endcap presampler [83] is a multi-wire proportional counter located in the region between the pressure bell and the endcap lead glass detector. The device consists of 32 chambers arranged in 16 sectors covering all ϕ and the polar angle range $0.83 < |\cos\theta| < 0.95$. Performance results from test beam electrons and pions show that the spatial resolution attained is in agreement with the expected $1/\sqrt{12}$ of the strip or wire effective pitch, which is 0.2 cm for the anode strips and 0.32 cm for the cathode planes.

Endcap electromagnetic calorimeter: The endcap electromagnetic calorimeter [84] consists of two dome-shaped arrays of 1132 lead glass blocks located in the region between the pressure bell and the pole tip hadron calorimeter. It has an acceptance coverage of the full azimuthal angle and $0.81 < |\cos\theta| < 0.98$.

Time-of-flight Counters: The time-of-flight system consists of barrel and endcap detectors and provides fast triggering information, effective rejection of cosmic rays and charged particle identification in the low momentum region (0.6 - 2.5 GeV/c). The time-of-flight system consists of 160 scintillation counters forming a barrel layer 6.84 m long with mean radius 2.36 m surrounding the OPAL coil and covering the region $|\cos\theta| < 0.82$. Light is collected from both ends of each counter via Plexiglas light guides glued directly onto phototubes which are shielded from stray magnetic fields. The output signal from each phototube is then split into two parts. The first, for the timing measurement, goes to a constant fraction discriminator, TDC and mean timer. The second goes to an ADC for a pulse height measurement which can be used to correct the pulse heights of the electromagnetic and hadronic calorimeters. The time-of-flight trigger signals are derived from the mean timers with the requirement that the time of flight was within 50 ns and that discriminators at both ends

fire within 50 ns of each other. The time-of-flight system achieves a timing resolution in the central region of the counters of 350 ps with a z resolution around 10 cm. The endcap detector was installed in 1997 to provide additional information on minimum ionizing particles in the endcap region. It consists of a 1 cm thick scintillator layer between the endcap presampler and the endcap electromagnetic calorimeter.

3.2.3.2 Hadron calorimeter

The hadron calorimeter is built in 3 sections: the barrel, the endcap and the pole-tip. By positioning detectors between the layers of the magnet return yoke a sampling calorimeter is formed covering a solid angle of 97% of 4π and offering at least 4 radiation lengths of iron absorbers to particles emerging from the electromagnetic calorimeter. Essentially all hadrons are absorbed at this stage leaving only muons to pass into the surrounding muon chambers. To correctly measure the hadronic energy, the hadron calorimeter information must be used in combination with that from the preceding electromagnetic calorimeter. This is necessary due to the likelihood of hadronic interactions occurring in the 2.2 radiation lengths of material that exists in front of the iron yoke.

The barrel region contains nine layers of chambers sandwiched with eight layers of 10 cm thick iron. The barrel ends are then closed off by toroidal endcaps consisting of 8 layers of chambers sandwiched with 7 slabs of iron. The chambers themselves are limited streamer tube [85] devices strung with anode wires 10 mm apart in a gas mixture of isobutane (75%) and argon (25%) which is continually flushed through the system. The signals from the wires themselves are used only for monitoring purposes. The chamber signals from induced charge are collected on pads and strips

which are located on the outer and inner surfaces of the chambers respectively. The layers of pads are grouped together to form towers that divide the detector volume into 48 bins in ϕ and 21 bins in θ. The analogue signals from the 8 pads in each chamber are then summed to produce an estimate of the energy in hadron showers which is subsequently digitized by a 12-bit ADC. From pion test beam results, the tower response was found to be linear with energy and has a resolution of σ_{E}=120%$\sqrt{\mathrm{E}}$ [71] where E is in GeV. The strips are made from aluminum of width 0.4 cm, which runs the full length of the chamber centered above the anode wire positions. Hence they run parallel to the beam line in the barrel region and in a plane perpendicular to this in the endcaps. Strip hits thus provide muon tracking information with positional accuracy limited by the 1 cm wire spacing. Typically, the hadronic shower initiated by a normally incident 10 GeV pion produces 25 strip hits and generates a charge of 600 pC.

The barrel detector covers the angular region up to $|\cos\theta| < 0.81$. The endcap detector extends the angular region up to $|\cos\theta| < 0.91$. The pole-tip detector [86] extends the angular coverage up to $|\cos\theta| < 0.99$ using ten thin multi-wire chambers with nine 8 cm thick iron plates.

3.2.4 Luminosity monitor

The forward detector [71] is used to determine the luminosity delivered to the interaction point. The cross section of Bhabha ($\mathrm{e^+e^-} \to \mathrm{e^+e^-}$) events in the forward detector can be calculated as:

$$\sigma_{\mathrm{Bhabha}} = \frac{16\pi\alpha^2}{\mathrm{s}}\left(\frac{1}{\theta^2_{\mathrm{min}}} - \frac{1}{\theta^2_{\mathrm{max}}}\right), \tag{3.3}$$

where α is the electromagnetic coupling constant at the Z resonance. s is the center of mass energy. θ_{min} and θ_{max} define the angular acceptance of the forward

detector, which are 47 mrad and 120 mrad for this detector. The forward detector consists of a lead glass calorimeter, proportional tube chambers, gamma catcher and far forward monitor, which are described below.

Calorimeter: The forward calorimeter consists of 35 sampling layers of lead glass scintillator with a presampler of 4 radiation lengths and the main calorimeter of 20 radiation lengths.

Proportional tube chambers: There are three layers of proportional tube chambers positioned between the presampler and main sections of the calorimeter. The position resolution is ± 0.05 cm.

Gamma catcher: The gamma catcher is a ring of lead scintillator of 7 radiation length thickness. It plugs the hole in acceptance between the inner edge of the electromagnetic endcap calorimeter and the start of the forward calorimeter.

Far forward monitor: The far forward monitor counters are small lead glass scintillator calorimeters, 20 radiation lengths thick, mounted on either side of the beampipe 7.85 m from the intersection region. Electrons which are deflected outwards by the action of LEP quadrupoles are detected in the range 5 to 10 mrad.

A silicon tungsten detector was added to improve luminosity measurement precision after 1993. The silicon tungsten detector is a sampling calorimeter designed to detect low angle Bhabha scattering events in order to measure the luminosity. There are 2 calorimeters at ± 238.94 cm in z from the interaction point with an angular acceptance of 25 mrad to 59 mrad. Each calorimeter consists of 19 layers of silicon detectors and 18 layers of tungsten. At the front of each calorimeter is a bare layer of silicon to detect preshowering, the next 14 silicon layers are each behind 1 radiation length (0.38 cm) of tungsten and the final 4 layers are behind

2 radiation lengths (0.76 cm) of tungsten. Luminosity may be determined to a precision of 0.1% using the forward detector and silicon tungsten detector.

3.2.5 Trigger of the OPAL detector

Electron and positron bunches collide at the interaction point every 11 μs in the 4 $\times$ 4 modes (4 electron bunches and 4 positron bunches) before 1993. After 1993 LEP was changed to 8 on 8 bunches. OPAL decided to modify the pretrigger to keep the old trigger [87]. The trigger is used to decide which events are of physics interest and which should not be considered further during this time interval. The expected physics event rate can be calculated by the luminosity times the interaction cross-section. For LEP I, the luminosity is around 1.6×10^{31} cm^{-2}s^{-1}. The cross section of Z decay to lepton pairs and multi-hadrons is 92 nb, so the expected total physics event rate is around 1.5 Hz. To efficiently select physics events of interest, the trigger should be as loose as possible. However this will increase the background rate and experiment deadtime. The OPAL trigger is designed so that the deadtime of the experiment does not exceed 10% of the trigger rate. As the average dead time for recording an event is 20 ms, the maximum allowed trigger rate can be calculated as 10%/20 ms, i. e. 5 Hz.

The general trigger information can be divided into two classes, stand-alone signal and coincidence signal. Stand-alone signals are formed by 1 bit information indicating tracking chamber multiplicity counts and total energy summations. For the coincidence signal, each detector is divided into 24 intervals in ϕ and 6 intervals in θ. A 24 $\times$ 6 $\theta - \phi$ matrix is formed. A $\theta - \phi$ bin is set if the signal in the corresponding region of the detector is seen. The standalone trigger and coincidence trigger are analyzed in parallel to provide a faster trigger for physics events. If no

trigger condition is met, the whole detector is reset for the next bunching crossing.

3.2.6 Online ROPE

When the trigger conditions are met, each subdetector is read out separately by its own special front-end readout electronics into its local system crate(s). Then the data are assembled in the event builder and are passed in sequence to the Filter. The Filter is a collection of software that acts as a third level trigger where the events are checked, analyzed, monitored and compressed before being written to disks. Some obvious junk events, such as beam gas backgrounds, typically 15% - 35% of all triggers, are rejected. A completed record of events, including event pointers, event header and calibration information, is written in data files in 20 Mbyte partitions. All of these 20 Mbyte files are copied from the Filter disk to the ROPE (Reconstruction of OPAL Events) farm. ROPE is a collection of software designed to reconstruct raw digit events to DST (Data Summary Tape) format which can be analyzed online or offline. The event data files are also spooled off to cartridge as a permanent backup before they are deleted from the Filter disk.

The Online ROPE farm provides the following functionality:

1. record online data onto optical disks and tapes;
2. reconstruct the events in real time or almost real time;
3. perform data monitoring;
4. distribute DST files and ROPE log files to computer center, subdetector calibration files to the subdetector groups.

Finally, the data are stored in DST format for offline analysis. The raw data are also stored for future improvements, such as better calibration and improved

reconstruction techniques.

In addition, the system is used to perform offline data Re-Ropes. Re-Rope is offline reconstruction performed on raw data with improved calibrations etc. The system runs on 12 dedicated HP workstations. It runs continuously, not knowing about the start or end of runs, and requires no operator intervention. Tapes are automatically mounted by a robot in the CERN computer center.

Chapter 4

Event preselection

This chapter describes the techniques to identify candidates of b decay and candidates of electron and muon tracks from raw OPAL data in Z decay. A hadronic event selection [88] and detector performance requirements are applied to the data. The thrust axis polar angle $|\cos\theta|$ is required to be less than 0.9 to ensure that the events are well contained within the acceptance of the detector. The selected events must pass the b identification[89], the lepton selection and the b semileptonic decay selection. These preselections use the OPAL standard b tagging (BT) and particle identification (ID) packages and are described in detail in the following sections. After all these preselections, the $b \to X_u \ell\nu$ decay purity is 1.3% and the main background is from $b \to X_c \ell\nu$ decays. An Artificial Neural Network (ANN) algorithm is introduced in this chapter as it is widely used in event selection.

4.1 An introduction to Artificial Neural Networks

Artificial Neural Networks are computational models applied to classification, pattern recognition and optimization, inspired by biological neural systems. A neural

network is constructed based on a series of inputs, one or more outputs and multiple layers of nodes lying between inputs and outputs, an example of which is shown in Figure 4.1. The inputs, outputs and nodes in the neural network are connected by

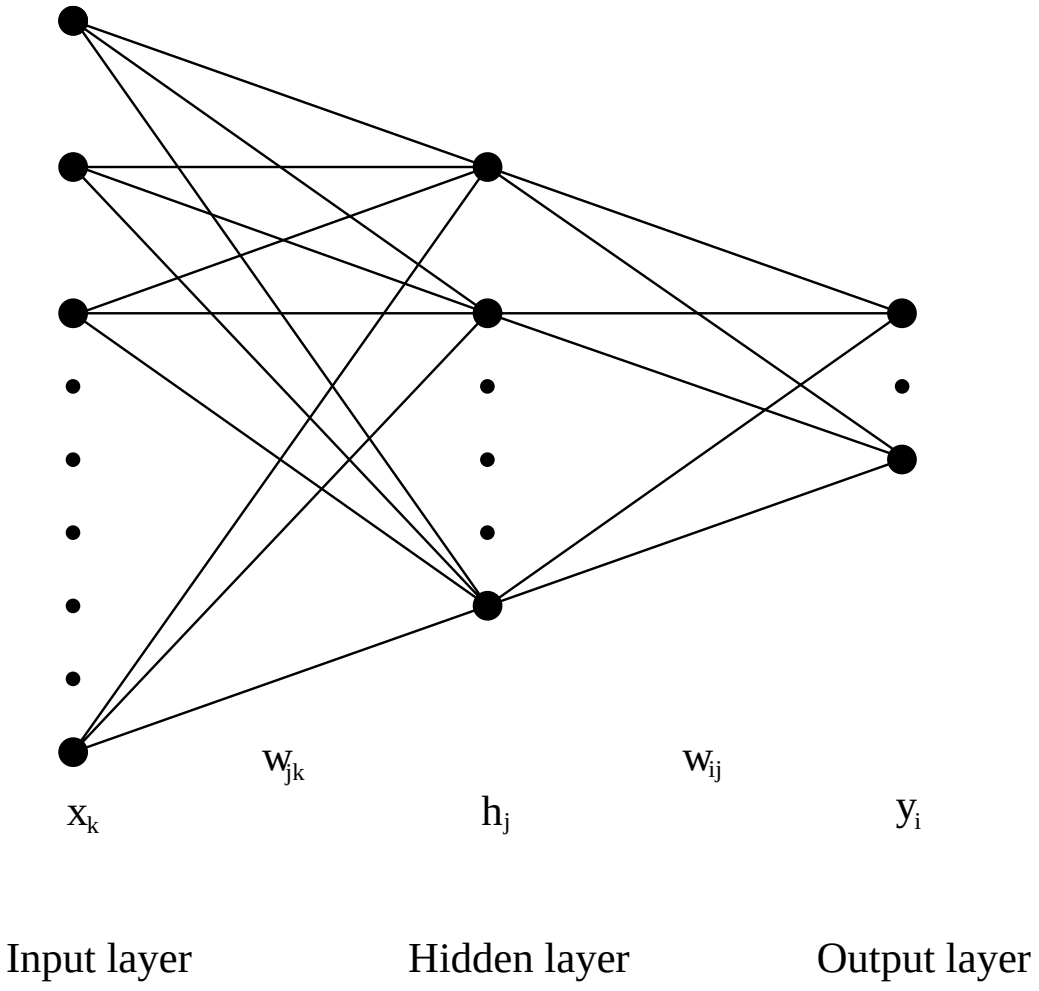

Figure 4.1: Input, hidden and output layers in a neural network

weights which can be obtained by training of known samples. Feed-forward neural networks, in which the connections are unidirectional, are used in this analysis.

Neural network outputs can be calculated from inputs and weights based on the following formula:

$$y_i = g(\sum_j w_{ij} g(\sum_k w_{jk} x_k + \theta_j) + \theta_i), \tag{4.1}$$

where y_i is the neural network i^{th} output. w_{ij} is the weight between the internal node j and i^{th} neural network output. w_{jk} is the weight between the internal node j and k^{th} neural network input. θ_j and θ_i are constant threshold values for the nodes, which can be used to adjust neural network performance and are commonly set to zero. The transfer function g controls neural network response and has the form:

$$g(x) = \frac{1}{1 + e^{-2x/T}}, \tag{4.2}$$

where T is the temperature of the neural network. The Figure 4.2 shows g(x) as a function of different temperatures. For a higher temperature, g(x) approaches a straight line and the resulting neural network has a linear response. This neural network can be used in function fitting applications. For a lower temperature, g(x) approaches a step function and is used in pattern recognition. The temperature is relatively arbitrary as the neural network can adjust itself accordingly. The temperature is chosen to be 1, which is a common choice for the separation of two samples.

The weights and thresholds of the neural network can be obtained by minimizing an error function using a training sample, for which the event classification is known. The error function is defined as:

$$E = \frac{1}{2} \sum_p (o_p - t_p)^2, \tag{4.3}$$

where the sum runs over all training patterns. o_p is the output of the neural network from the training sample. t_p is the expected output from the training sample. For minimizing the error function, the back propagation technique is used and is introduced as follows. The weights are updated during each iteration of the training pattern p:

$$w_{jk}^{(p+1)} = w_{jk}^{(p)} + \Delta w_{jk}^{(p)}, \tag{4.4}$$

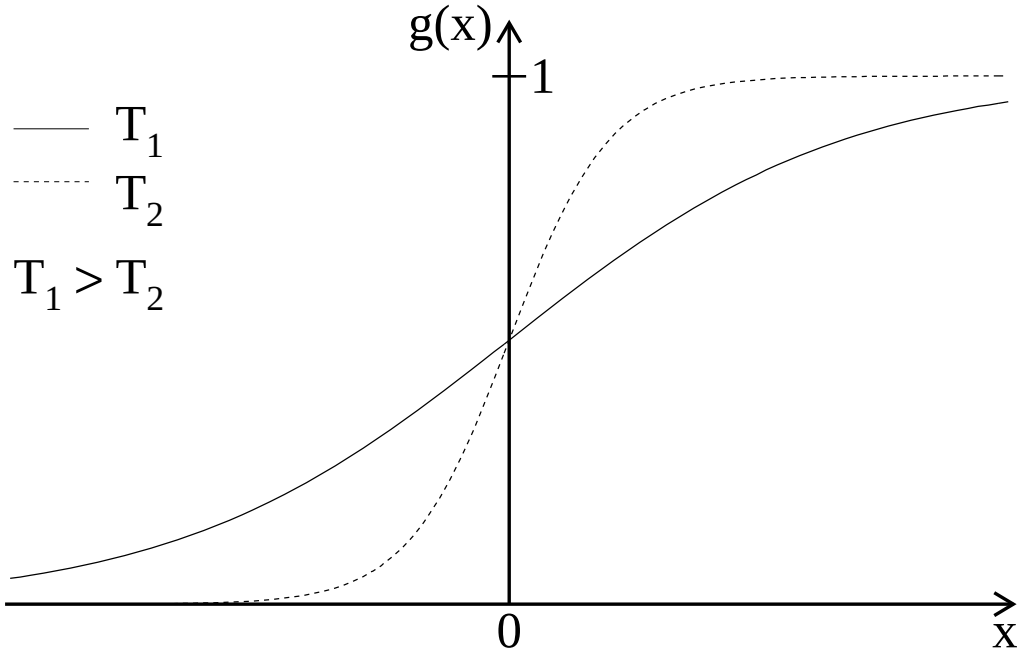

Figure 4.2: g(x) as a function of temperature.

$\Delta w_{jk}^{(p)}$ can be obtained from:

$$\Delta w_{jk}^{(p)} = -\eta \frac{\partial E}{\partial w_{jk}} + \alpha \Delta w_{jk}^{(p-1)}, \tag{4.5}$$

where η is the step size parameter controlling the convergence rate. α is the momentum parameter which is between 0 and 1.

After the neural network is optimized using the training samples, test samples are used to test the neural network performance. The neural network can learn the specific features of training samples by using a very complicated neural network structure. If neural network output distributions from the test samples are different from those of the training samples, the training sample size, η, α and neural network structure should be adjusted. Here the neural network structure means number of layers, number of input variables and nodes.

To optimize the training procedure, the following rules should be considered:

- Input variables are chosen based on separation power and minimal correlation.
- All input variables should be scaled to values of the order of one. If the order of magnitude of the input values varies a lot, the training will be very slow.
- The number of training events in the different classes should be equal. The training events of the different classes should be presented to the neural network alternately.
- For a given number of hidden nodes, twice the number of inputs should be sufficient for any problem, but fewer hidden nodes are often used. For the size of the training sample, the more the better. One thousand training events per hidden node should be sufficient.
- Parameters such as the step size η and the momentum α should be optimized.

The temperature is not a critical parameter, as long as no extreme values are chosen.

4.2 Multi-hadron selection

The current analysis uses OPAL data from Z decays. The multi-hadron $Z \to q\bar{q}$ selection criteria [90] (where q can be u, d, s, c, b) are applied first to suppress the background events from Z to lepton pair decays. In this multi-hadron event selection, good electromagnetic clusters are defined as having:

1. $E_{raw} \geq 0.100$ GeV in the barrel or $E_{raw} \geq 0.200$ GeV in the endcap, where E_{raw} is the uncorrected energy of the cluster;
2. $N_{blocks} \geq 1$ in the barrel or $N_{blocks} \geq 2$ in the endcap, where N_{blocks} is the number of adjacent blocks in the cluster.

Good tracks are defined as having:

1. $N_{hit} \geq 20$, where N_{hit} is the total number of hits in the vertex, jet and z tracking chambers;
2. $|d_0| < 2$ cm, where $|d_0|$ is the impact parameter;
3. $|z_0| < 40$ cm, where $|z_0|$ is the z coordinate of the track at the point of closest approach;
4. $p_{xy} \geq 0.050$ GeV/c, where p_{xy} is the track momentum transverse to the z axis;
5. $|\cos\theta| < 0.995$, where θ is the azimuthal track angle;
6. $\chi^2_{r-\phi} < 999$, where $\chi^2_{r-\phi}$ is the χ^2 calculated from the track fitting in $r-\phi$ plane;

7. $\chi^2_z < 999$, where χ^2_z is the χ^2 calculated from the track fitting in r − z plane.

Events are selected as multi-hadron events if they satisfy all of the following conditions:

1. $R_{vis} \geq 0.10$, where $R_{vis} = \frac{\sum E_{raw}}{2 \times E_{beam}}$ and the summation runs over all good clusters;
2. $|R_{bal}| \leq 0.65$, where $R_{bal} = \frac{\sum E_{raw} \cos\theta}{\sum E_{raw}}$ and θ is the polar angle of the cluster;
3. $N_{tracks} \geq 5$, where N_{tracks} is the number of good tracks;
4. $N_{clusters} \geq 7$, where $N_{cluster}$ is the number of good clusters.

The main background in the multi-hadron selection is from $Z \to \tau^+\tau^-$ and two-photon events, which account for $(0.11 \pm 0.03)\%$ and $(0.5 \pm 0.02)\%$ of selected multi-hadronic events respectively [90]. The multi-hadron selection efficiency is 98.4% [90].

The selection of b hadron events uses tighter requirements for tracks, which are:

- the number of hits in the jet chamber greater than 20,
- the track momentum less than 65 GeV/c,
- the track transverse momentum to the z axis greater than 0.15 GeV/c,
- $|\cot\theta|$ less than 100, where θ is the track polar angle from the z axis,
- $\chi^2_{r-\phi} < 100$,
- $\chi^2_z < 100$.

The selection of b hadron events also requires tighter cuts for electromagnetic clusters, which are:

- the corrected energy of barrel clusters greater than 0.2 GeV,

– the corrected energy of endcap clusters greater than 0.1 GeV.

4.3 b identification

A neural network algorithm [89] based on charged particle vertex information is used to separate the b flavour events from the other flavour events in each hemisphere. The OPAL BTag [89, 91] package is used for the thrust and jet finding, primary and secondary vertex reconstruction, b tagging and charged track quality selection. Both hemispheres are searched for lepton candidates.

4.3.1 Jet finding

The primary quark and anti-quark pair from electron and positron collision produces a back to back pair of jets due to momentum conservation, as shown in Figure 4.3. The primary quark may radiate gluons and produce additional jet(s), as shown in Figure 4.4. A cone jet finding algorithm [92, 93] is used to define the tracks and clusters into jets. In this analysis, the total energy in a jet greater than 10.0 GeV and a cone of half angle greater than 0.7 radian are used to define b jets.

4.3.2 Primary and secondary vertex reconstruction

The primary vertex (b hadron production point) position, shown in Figure 4.5, is calculated using a three-dimensional χ^2 minimization technique. The primary vertex is found by using the tracks from only one hemisphere plus a beam spot constraint. A common vertex is fit to all tracks in the hemisphere and the beam

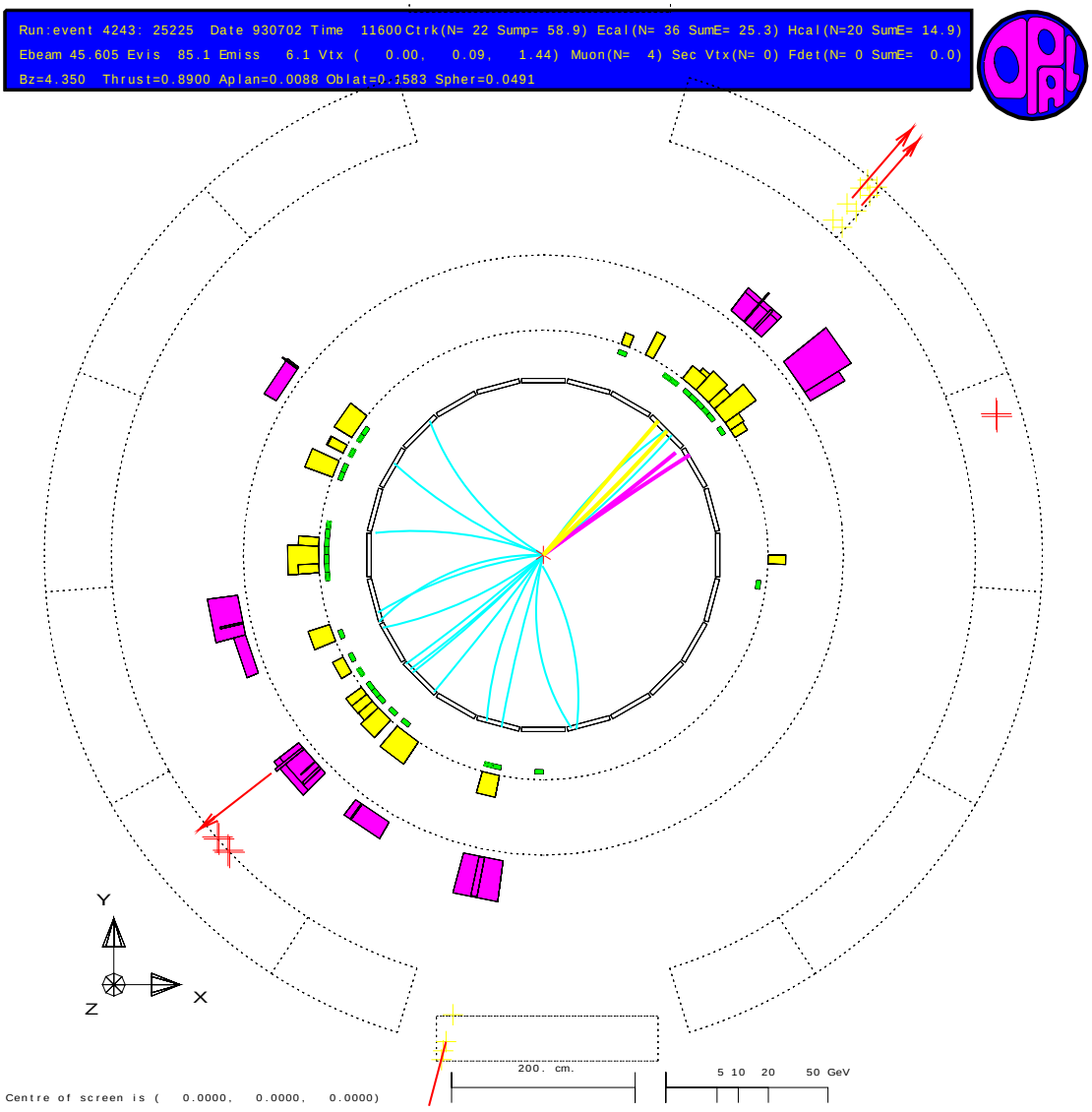

Figure 4.3: A 2 jet event from the OPAL event display. Tracks within inner detectors are depicted as curved lines. The hits in the calorimeters are depicted as filled rectangles, with energy deposited proportional to the rectangle area. The hits in the muon chambers are shown as arrows and X's at the outermost detector.

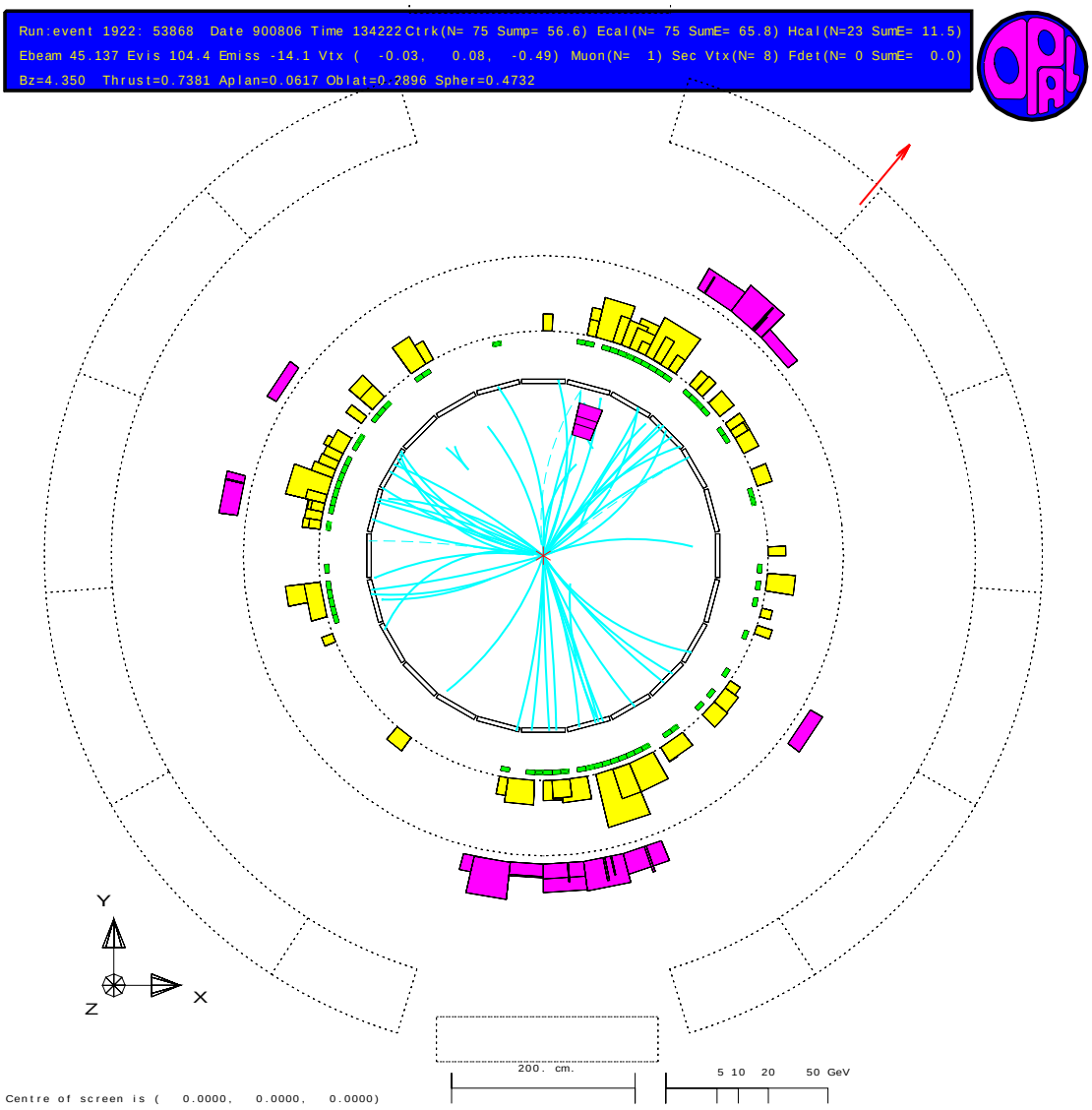

Figure 4.4: A 3 jet event from the OPAL event display. See Figure 4.3 for the explanation of tracks and hits.

spot. Tracks contributing a χ^2 of greater than four are iteratively removed from the fit. If no tracks remain after this procedure, the beam spot is used instead. The

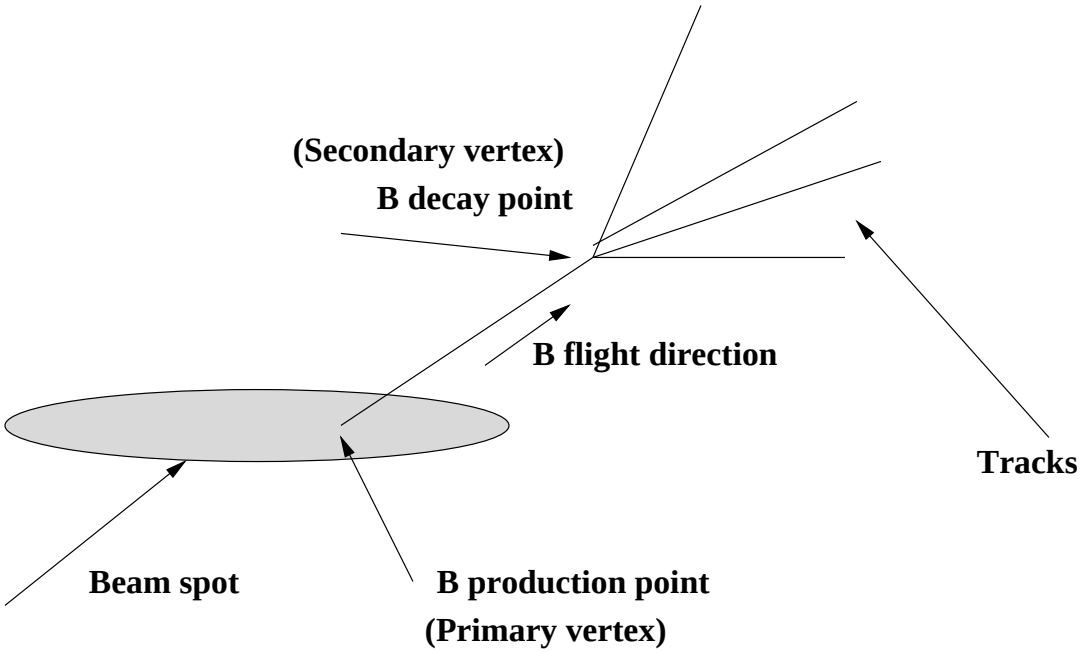

Figure 4.5: The beam spot, primary vertex and secondary vertex in b decay.

secondary vertex (b hadron decay point) is reconstructed using a similar method to the primary vertex reconstruction. The following track quality constraints are required for secondary vertex track candidates:

- the track momentum greater than 0.5 GeV/c,
- the impact parameter with respect to the reconstructed hemisphere primary vertex less than 0.3 cm,
- the error on the track impact parameter with respect to the reconstructed hemisphere primary vertex less than 0.1 cm.

4.3.3 b vertex flavour tagging

The relatively long lifetimes of b hadrons, combined with the boost provided in Z decay, give rise to b track lengths of a few millimeters. This lifetime information can be used to select b hadron samples. Typically, either several charged particle tracks with impact parameters with respect to the primary vertex significantly larger than measurement errors are required, or a second vertex is sought with a significant decay length. With the installation of silicon micro-vertex detectors, b vertex tagging becomes possible. The standard OPAL b tag (BT) neural network 5 [89, 91] is used to separate the b flavour events from other flavour events. The BT neural network uses the number of tracks in the secondary vertex, the vertex decay length L, the decay length significance L/σ_L, the reduced decay length significance and the critical track discriminant [91] as input variables. The vertex decay length L is calculated as the length of the vector from the primary to the secondary vertex. L is given a positive sign if the secondary vertex is displaced from the primary in the direction of the jet momentum, and a negative sign otherwise. The critical track discriminant represents the probability that a set of tracks with invariant mass greater than the average charm hadron mass is consistent with having originated from the reconstructed secondary vertex. The b decays tend to have a large number of tracks in the secondary vertex due to the high mass of b hadrons, longer decay length and larger decay length significance due to the longer life of b hadrons. A vertex tagging variable B is defined as:

$$|\mathrm{B}| = -\ln(1 - \mathrm{NN_b}), \tag{4.6}$$

where $\mathrm{NN_b}$ is the BT neural network output. B is defined as having the same sign as the vertex decay length. The output from the BT neural network is required to be greater than 0.8, corresponding to vertex tagging variable |B| greater than 1.6,

which is shown in Figure 4.6, resulting in a b purity of more than 91% and an efficiency around 30%. The b purity increases after subsequent b hadron semileptonic decay neural network selection, which is described below. The thrust axis polar angle $|\cos\theta|$ is required to be less than 0.9 so that events will be well contained in the acceptance of the detector. Here the thrust T is defined as:

$$\mathrm{T} = \max_{\mathrm{n}} \left(\frac{\sum_{\mathrm{i}} |\overrightarrow{\mathrm{p}}_{\mathrm{i}} \cdot \hat{\mathrm{n}}|}{\sum_{\mathrm{i}} |\overrightarrow{\mathrm{p}}_{\mathrm{i}}|} \right), \tag{4.7}$$

where the summation i runs over all tracks and unassociated clusters in the event. $\overrightarrow{\mathrm{p}}_{\mathrm{i}}$ is the momentum of the i^{th} track or unassociated cluster. The $\hat{\mathrm{n}}$ which maximizes the thrust value is called the thrust axis. Both hemispheres are searched for electron and muon candidates after the b identification.

4.4 Lepton selection

Electrons are identified by the OPAL electron neural network [89, 94] using the track and calorimeter information. Before applying the neural network, the following cuts are required:

- Candidate track momentum is required to be greater than 2 GeV/c.
- The number of z chamber hits associated with the candidate track is required to be greater than 3. The number of jet chamber hits used to calculate the dE/dx is greater than 40.
- The average specific energy loss of ionizing particles can be described by the Bethe-Bloch equation [2]:

$$\mathrm{dE/dx} = -4\pi \mathrm{N_A r_e^2 m_e c^2 z_e^2 Z} \frac{1}{\mathrm{A}\beta^2} \left(\frac{1}{2} \ln \frac{2\mathrm{m_e c^2}\beta^2\gamma^2 \mathrm{T_{max}}}{\mathrm{I^2}} - \beta^2 - \frac{\delta}{2} \right), \tag{4.8}$$

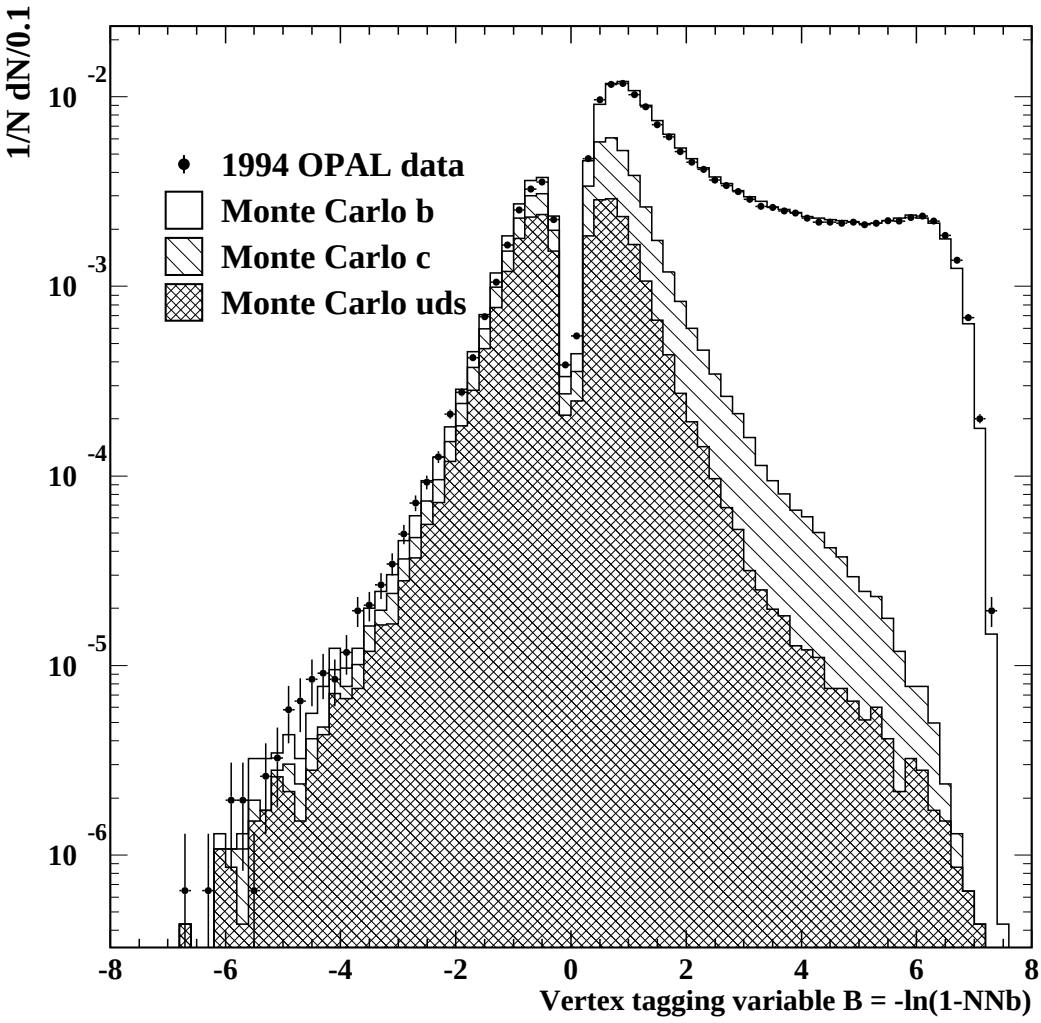

Figure 4.6: Distribution of the vertex tagging variable B for OPAL data and Monte Carlo simulated events. The contributions from uds, c and b jets are indicated [89]. A cut 1.6 in B is used, corresponding to BT neural network output NN_b cut 0.8.

where N_A is Avogadro's number, r_e is the classical electron radius and m_e is the electron mass. z_e is the charge of the the incident particle. Z and A are the atomic number and mass of the medium. T_{max} is the maximum kinetic energy which can be imparted to a free electron in a single collision. I is the mean ionizing potential and δ is a density function. The dE/dx distributions for the electron, muon, pion, kaon and proton from OPAL data are shown in Figure 4.7. $dE/dx|_{norm}$ is defined as:

$$dE/dx|_{norm} = \frac{dE/dx_{measured} - dE/dx_{expected}}{\sigma(dE/dx_{expected})}, \tag{4.9}$$

where $dE/dx_{measured}$ is the raw measured value and $dE/dx_{expected}$ is the expected value according to the Bethe-Bloch equation. $(dE/dx)_{norm}$ is required to be greater than -2.

The separation power S between particle a and b based on dE/dx can be defined as:

$$S = \frac{dE/dx_a - dE/dx_b}{\sqrt{\sigma^2(dE/dx_a) + \sigma^2(dE/dx_b)}}, \tag{4.10}$$

where dE/dx_a and dE/dx_b are the dE/dx for particle a and b respectively. $\sigma^2(dE/dx_a)$ and $\sigma^2(dE/dx_b)$ are the measurement errors on the specific ionization for particle a and b. The separation power depends on the particle momentum which is shown in Figure 4.8.

The six inputs to the electron neural network are:

1. the track momentum;
2. the track polar angle;
3. the electromagnetic energy to momentum ratio;
4. the number of electromagnetic calorimeter blocks contributing to the energy measurement;

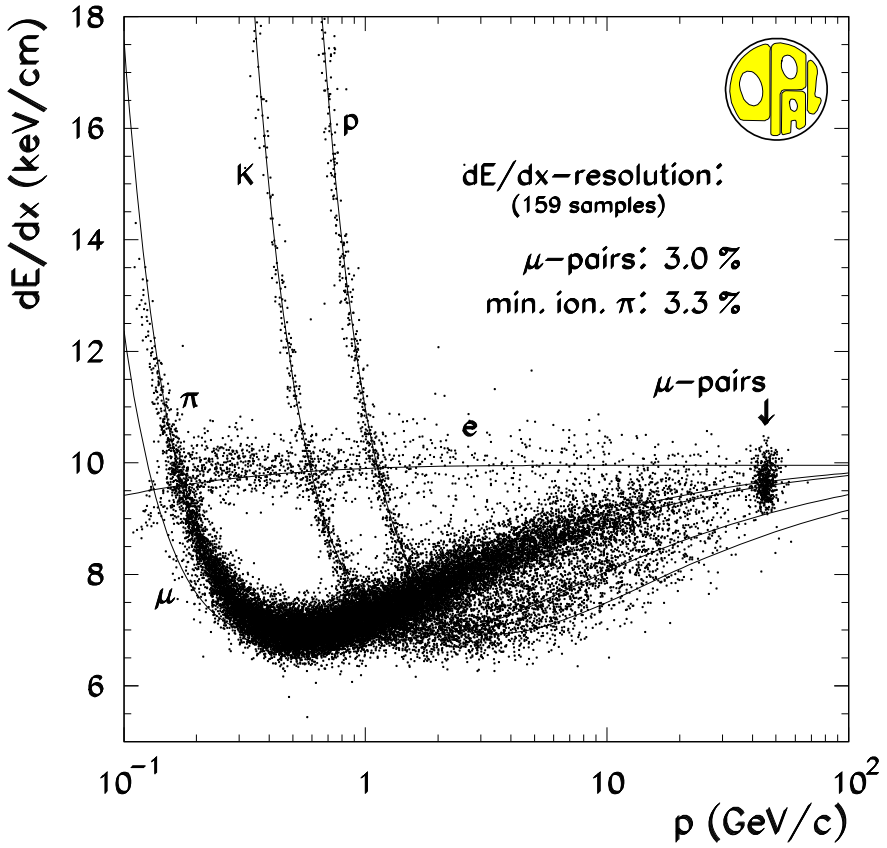

Figure 4.7: dE/dx from OPAL data for the electron, muon, pion, kaon and proton [80]. The dot points show data. The curves show the Bethe-Bloch predictions.

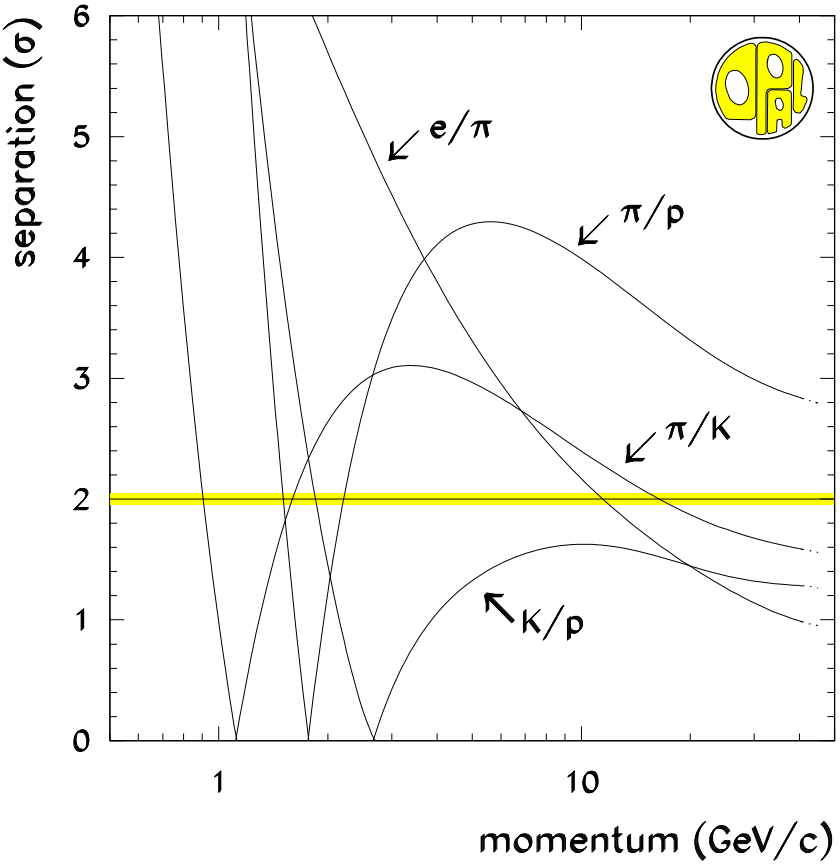

Figure 4.8: The dE/dx separation power from OPAL data for the electron, muon, pion kaon and proton [80].

5. the normalized ionization energy loss dE/dx;

6. the error on the normalized ionization energy loss.

The electron neural network output is shown in Figure 4.9. The neural network output is required to be greater than 0.9. The resulting electron efficiency is approximately 74% with a purity of 94%. Electrons from photon conversions, $\gamma \to e^+e^-$,

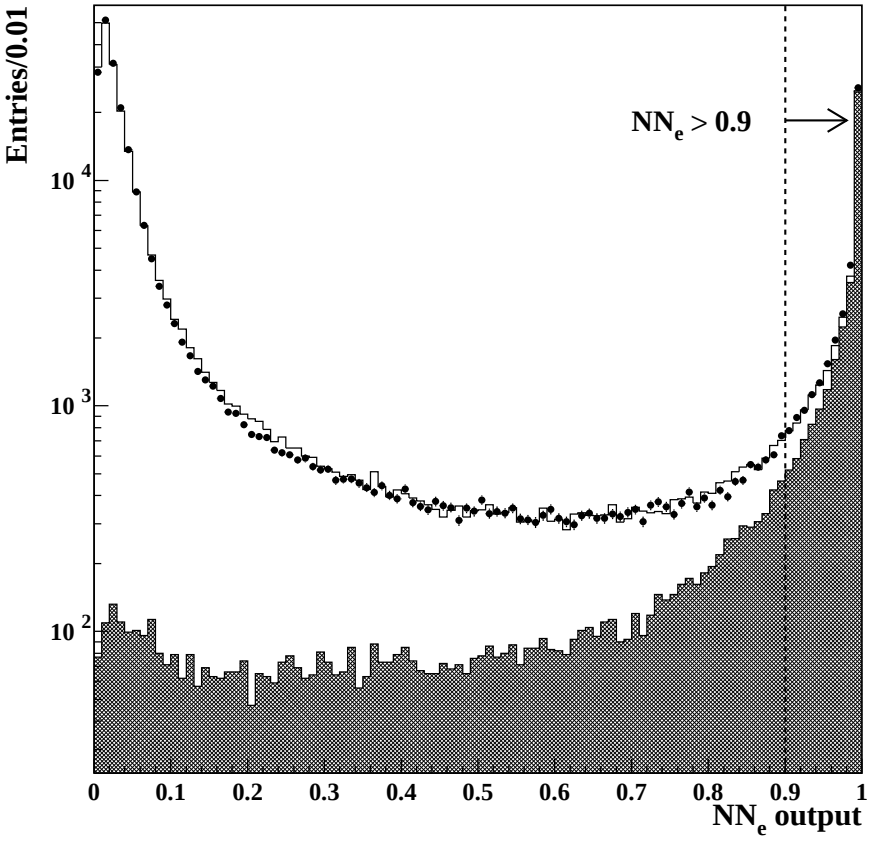

Figure 4.9: The electron neural network output NN_e for the true electron signal (hatched area) and for the total signal (solid histogram) in the Monte Carlo simulated events. The arrow shows the selected region. The OPAL data (points) are compared to the Monte Carlo simulated events [28].

contribute a significant background to the prompt electron samples. Another neural network is used to reject this background [89]. The nine input variables to this photon conversion neural network are:

- the distance between two tracks at tangency;
- for both tracks, the radius of the first measured tracking chamber hit with respect to the center of the OPAL detector;
- the radius of the reconstructed vertex of the candidate photon conversion;
- the invariant mass of the pair, assuming both tracks to be electrons;
- the impact parameter of the reconstructed photon with respect to the primary vertex of the event;
- the electron identification neural network output of the partner track;
- for both tracks, the product of the momentum and charge.

The photon conversion background is reduced by 94% after requiring the photon conversion neural network output less than 0.8, which is shown in Figure 4.10, whilst retaining 98% of the selected prompt electrons.

The muon momentum is required to be greater than 3 GeV/c. Muons are identified using reconstructed track segments in the muon chambers [89]. The reconstructed tracks in the central detector are extrapolated to the muon chambers to see if they match the track segments reconstructed in the external muon chambers. The position matching parameter $\chi_{\rm pos}$ is required to be less than 3, where $\chi_{\rm pos}$ is defined as:

$$\chi^2_{\rm pos} = (\frac{\Delta\theta}{\sigma_{\Delta\theta}})^2 + (\frac{\Delta\phi}{\sigma_{\Delta\phi}})^2, \tag{4.11}$$

where $\Delta\theta$ and $\Delta\phi$ are the differences in θ and ϕ between the extrapolated track position from the central detector and the nearest muon segment. $\sigma\Delta\theta$ and $\sigma\Delta\phi$

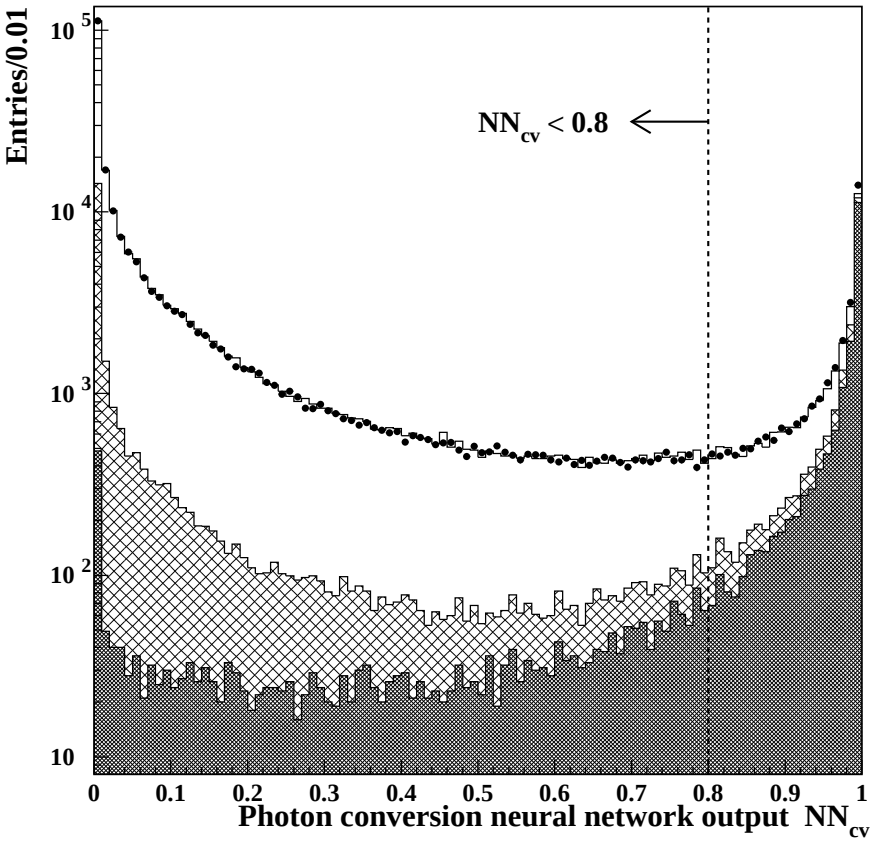

Figure 4.10: The photon neural network output NN_{cv} for OPAL data (points) and Monte Carlo simulated events (histogram). The darkly hatched region shows the electron from photon conversion. The lightly hatched region shows the prompt electron. The open region shown non-electron candidates. The tracks are selected with $NN_{cv} < 0.8$ to eliminate the electron background from the photon conversion [28].

are the errors of $\Delta\theta$ and $\Delta\phi$. The measured energy loss dE/dx is also required to be consistent with the expected value for a muon. The muon selection efficiency is approximately 90% and the muon purity approximately 93%.

Electron and muon momenta transverse to the direction of the jet containing the lepton are required to be greater than 0.5 GeV/c in order to reject leptons from light quark decays. The lepton is included in the calculation of the jet direction.

4.5 B semileptonic decay selection

A neural network [95] based on lepton information is used to separate the b hadron semileptonic decays, $b \to X_c \ell\nu$ and $b \to X_u \ell\nu$, from non semileptonic decays.

Eight input variables to this B semileptonic decay selection neural network are:

- the total momentum of the lepton candidate;
- the lepton transverse momentum with respect to the nearest jet axis, where the jet excludes the lepton candidate itself;
- the energy of the jet containing the lepton candidate;
- sub-jet energy, where the sub-jet contains the lepton candidate. The lepton jet is divided into two sub-jets, as described in [88];
- the scalar sum of transverse momenta of charged tracks in the lepton jet;
- the impact parameter of the lepton track with respect to the primary vertex, divided by the error on the distance;
- lepton Q_{jet}, i.e. the charge of the lepton candidate multiplied by the jet charge of the jet containing the lepton, including the lepton. The jet charge is the

weighted sum of all track charges in the jet,

$$Q_{jet} = \frac{\sum_j Q_i \times p_i^{0.5}}{\sum_i p_i^{0.5}}; \tag{4.12}$$

where Q_i is the track charge, p_i is the track momentum. The summation runs over all charged tracks in the jet;

– opposite Q_{jet}, i.e. the charge of the lepton candidate multiplied by the jet charge of the most energetic jet in the hemisphere opposite to the lepton.

The distributions of the neural network output variable are shown in Figure 4.11. A neural network cut greater than 0.8 is applied. After this neural network b semileptonic decay selection, the b hadron semileptonic decay purity is 97% and the efficiency is 65%; the $c \to l$ events, where c is primary quark, and $b \to c \to l$ events are suppressed.

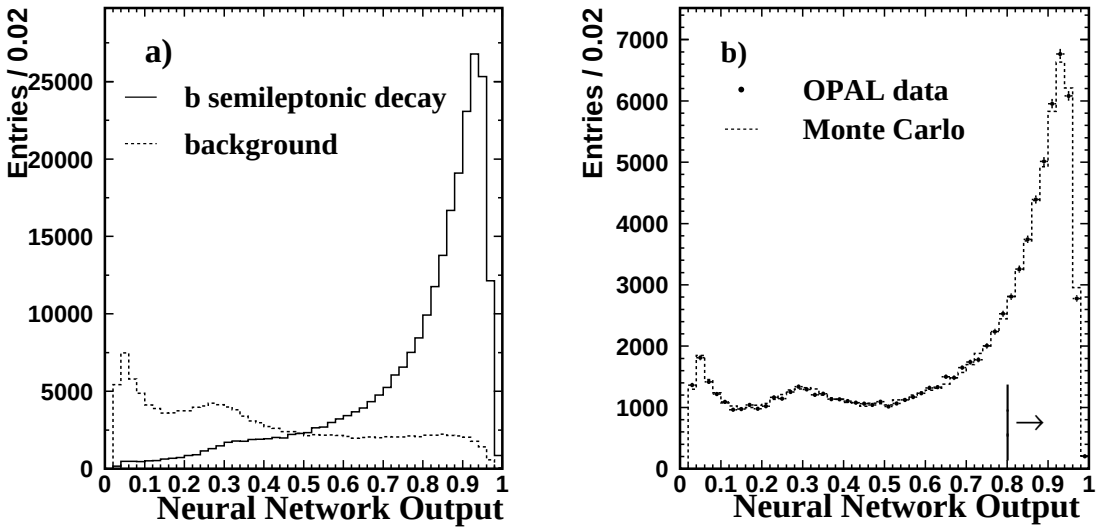

Figure 4.11: **a,b.** The b hadron semileptonic decay neural network output distributions. **a** for the b semileptonic decays and the scaled background from the Monte Carlo simulated events. **b** comparison between OPAL data and Monte Carlo simulated events. The selected region is shown by the arrow in **b**.

Chapter 5

Identification of b to u semileptonic decay

This chapter describes a neural network to separate the $b \to X_u \ell\nu$ decay from the background after the event preselection in Chapter 4. The input variables to the neural network are described in detail. The $b \to X_u \ell\nu$ model uses the $b \to X_u \ell\nu$ hybrid model described in Chapter 2.

5.1 b to u neural network

It is difficult to extract $b \to X_u \ell\nu$ decays from the dominating $b \to X_c \ell\nu$ background using only one single kinematic variable. A multi-layered feed-forward artificial neural network based on the JETNET 3.0 program [96] is used to extract $b \to X_u \ell\nu$ events. There are four layers in this neural network. The neural network structure is 7-10-10-1. In the first layer, seven variables are used as inputs to the neural network. Each of these variables has separation power between $b \to X_u \ell\nu$ and $b \to X_c \ell\nu$. The last layer is the neural network output variable which combines the separation power from these seven input variables. A figure of merit [97] is used to determine the discrimination power of

these seven variables in separating two classes of events, i.e. signal and background. The figure of merit is defined as:

$$\alpha_1\alpha_2 \int \frac{(f_1(x) - f_2(x))^2}{\alpha_1 f_1(x) + \alpha_2 f_2(x)} dx, \tag{5.1}$$

where $f_1(x)$ and $f_2(x)$ are normalized distributions for two classes, class 1 and class 2. α_1 and α_2 are the fractions of class 1 and class 2 in the total samples. The higher the figure of merit, the better the separation between the two classes.

In selecting these neural network input variables, nineteen variables were considered as input variables to this neural network initially, listed as below:

1. the invariant mass of the most energetic final state particle combined with the lepton,

2. the lepton energy in the b hadron rest frame,

3. the lepton momentum transverse to the jet axis (the jet axis calculation includes the lepton),

4. the transverse momentum of the most energetic particle with respect to the lepton direction,

5. the rapidity of the most energetic final state hadron calculated with respect to the lepton direction (assuming all hadronic particles are pions), the rapidity y is defined as:

$$y = \frac{1}{2} \log \frac{E + p_L}{E - p_L}, \tag{5.2}$$

   where p_L is the longitudinal momentum along the direction of the incident particle and E is the energy, both defined for a given particle,

6. the fraction of the reconstructed b hadron energy carried by the lepton,

7. the reconstructed hadronic invariant mass,
8. hadronic invariant mass of the charge particles,
9. charged particle multiplicity,
10. invariant mass of the most energetic and the second most energetic particles,
11. invariant mass of the most energetic and the third most energetic particles,
12. sum of the rapidity of the charged particles with respect to the lepton axis,
13. rapidity of the lepton with respect to the hemisphere axis,
14. invariant mass of the most energetic particle and the fourth most energetic particle,
15. invariant mass of the second, the third and the fourth most energetic particles,
16. invariant mass of the first, the third and the fourth most energetic particles,
17. transverse momentum of the second most energetic particle with respect to the lepton direction,
18. $\sum_{\mathrm{j}} \mathrm{p(j)}_{\mathrm{transverse}} / \sum_{\mathrm{j}} \mathrm{p(j)}$, where p(j) is the momentum of the j^{th} particle and $\mathrm{p(j)}_{\mathrm{transverse}}$ is the transverse momentum of the j^{th} particle with respect to the lepton direction,
19. $\sum_{\mathrm{j}} (\mathrm{p(j)}_{\mathrm{transverse}})^2$.

The last twelve variables are discarded for poor separation power between $b \to \mathrm{X_u} \ell \nu$ signal and background or poor agreement between the data and Monte Carlo simulated events. The first seven variables are selected as inputs to the $b \to \mathrm{X_u} \ell \nu$ neural network and the figures of merit for these seven variables are 0.057, 0.034, 0.018, 0.016, 0.012, 0.011 and 0.005 respectively, as ordered in the list above. The figure of merit of the reconstructed

hadron invariant mass is relatively low because of the poor resolution of the reconstructed hadron invariant mass. The seven input variable distributions for the $b \to X_u \ell\nu$ and the background in the Monte Carlo simulation are shown in Figure 5.1. The agreement between Monte Carlo simulated events and OPAL data for these seven variables is shown in Figure 5.2.

The correlations of these seven input variables, which are marked as V1 to V7 in the same order as list above, are shown in Figure 5.3 and Figure 5.4. The correlations of these seven input variables are not high and these seven variables can be used as inputs to the neural network. The input variables, hadronic invariant mass and the lepton energy in the b hadron rest frame, are discussed in detail in the following sections.

5.1.1 Hadronic invariant mass

The reconstructed hadronic invariant mass M_x, the last input variable to $b \to X_u \ell\nu$ neural network, can be obtained from:

$$M_x{}^2 = \sum_i (W_i E_i)^2 - \sum_i (W_i \vec{p}_i)^2, \tag{5.3}$$

where i denotes all hadronic tracks and clusters. W_i is the track or neutral cluster weight from OPAL b hadron reconstruction code [98], which is equal to the probability that a hadronic track or a neutral cluster comes from b decay. E_i and $\vec{p}_i$ are the energy and momentum of the i^{th} hadronic track or neutral cluster. The track and cluster weight are used to separate tracks and clusters from the true b production and the fragmentation. The track weight is obtained by combining the track vertex weight and the rapidity-based neural network weight and is shown in Figure 5.5. The track vertex weight and the rapidity-based neural network are described in detail in [98].

Approximately thirty percent of the b hadron energy is in neutral final state particles. All clusters in the electromagnetic and hadronic calorimeters are considered in the cluster

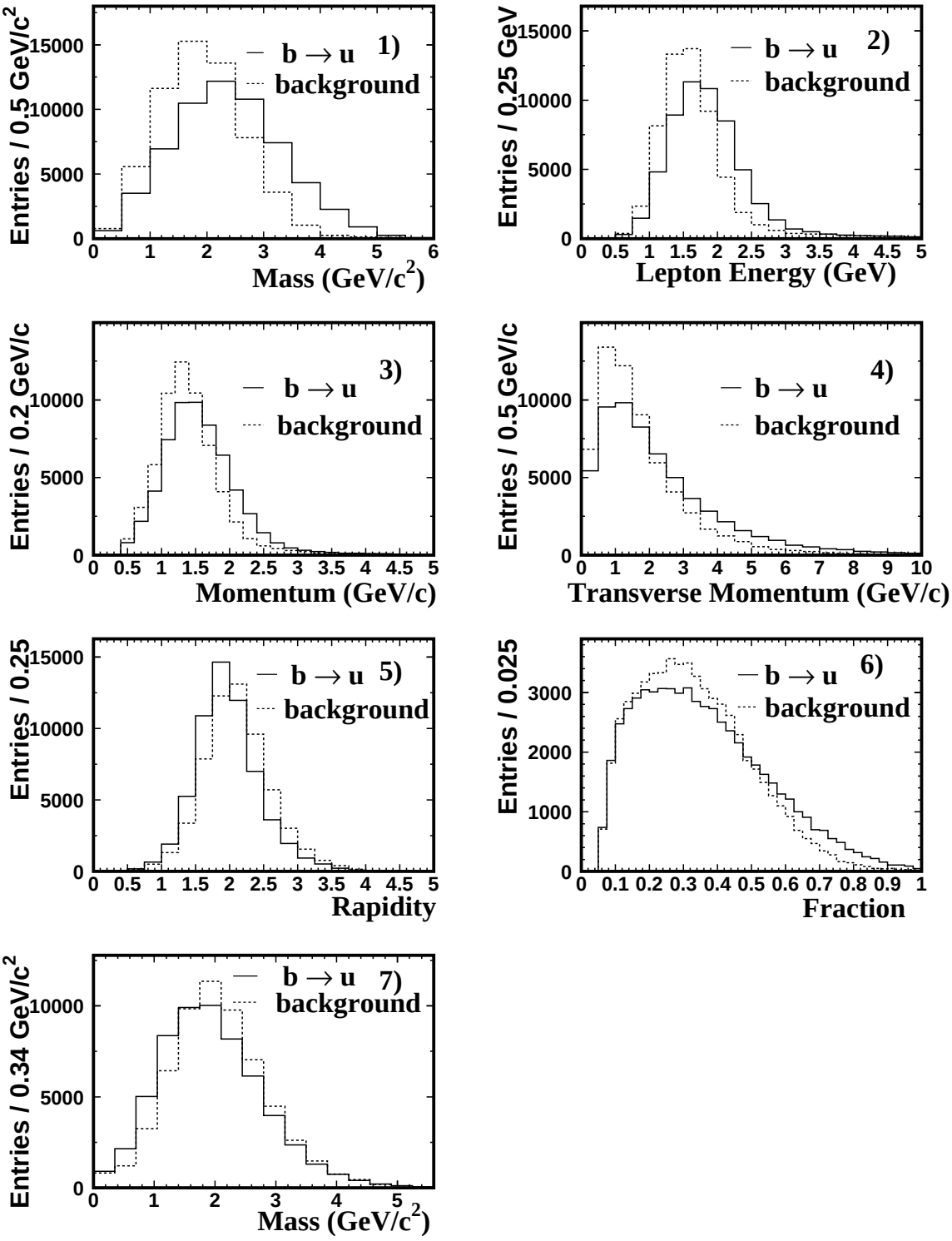

Figure 5.1: Comparison between the signal and the background in the Monte Carlo simulation for the seven b to u neural network input variables.

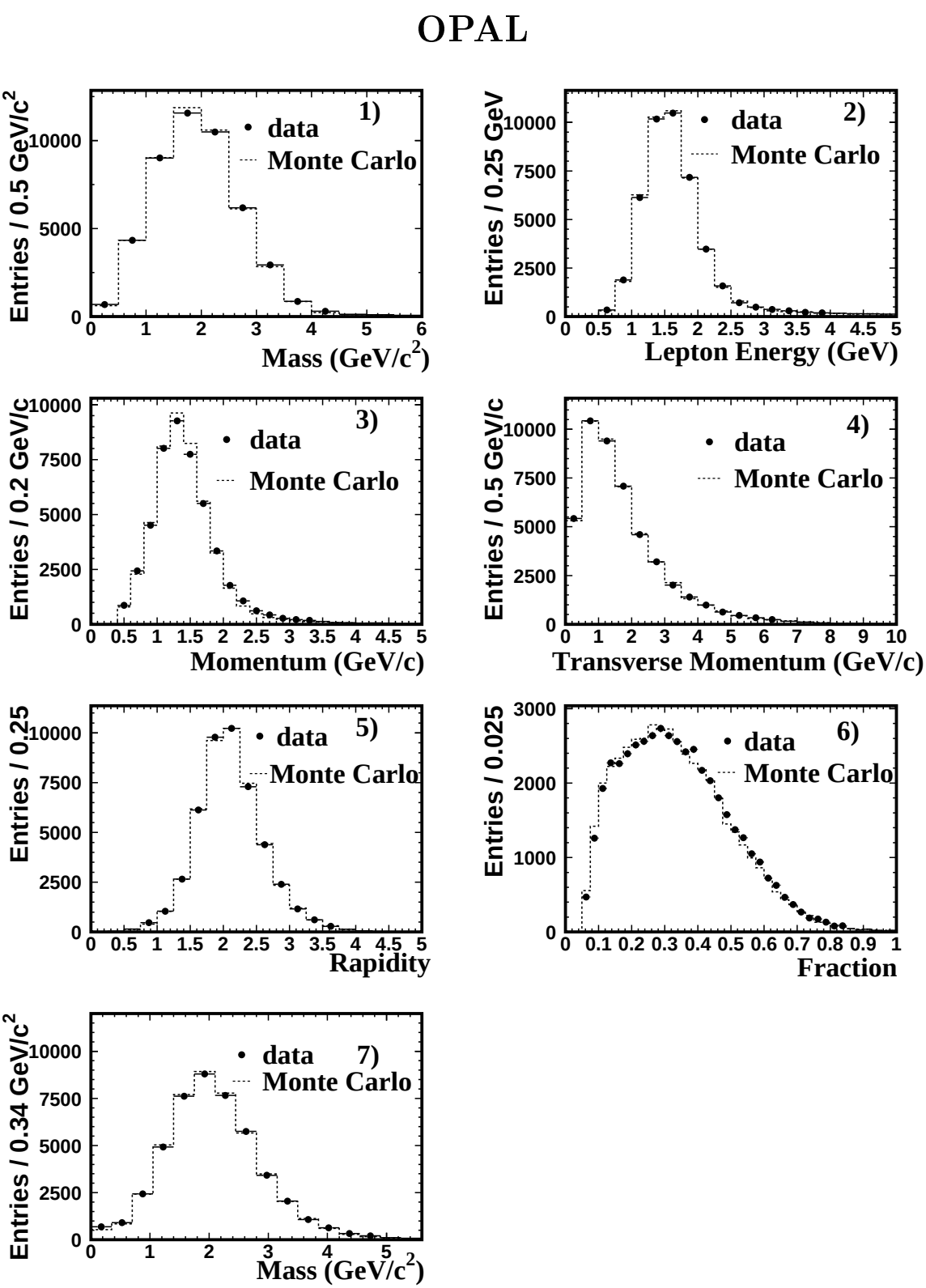

Figure 5.2: Comparison between OPAL data and Monte Carlo simulated events for the seven b to u neural network input variables.

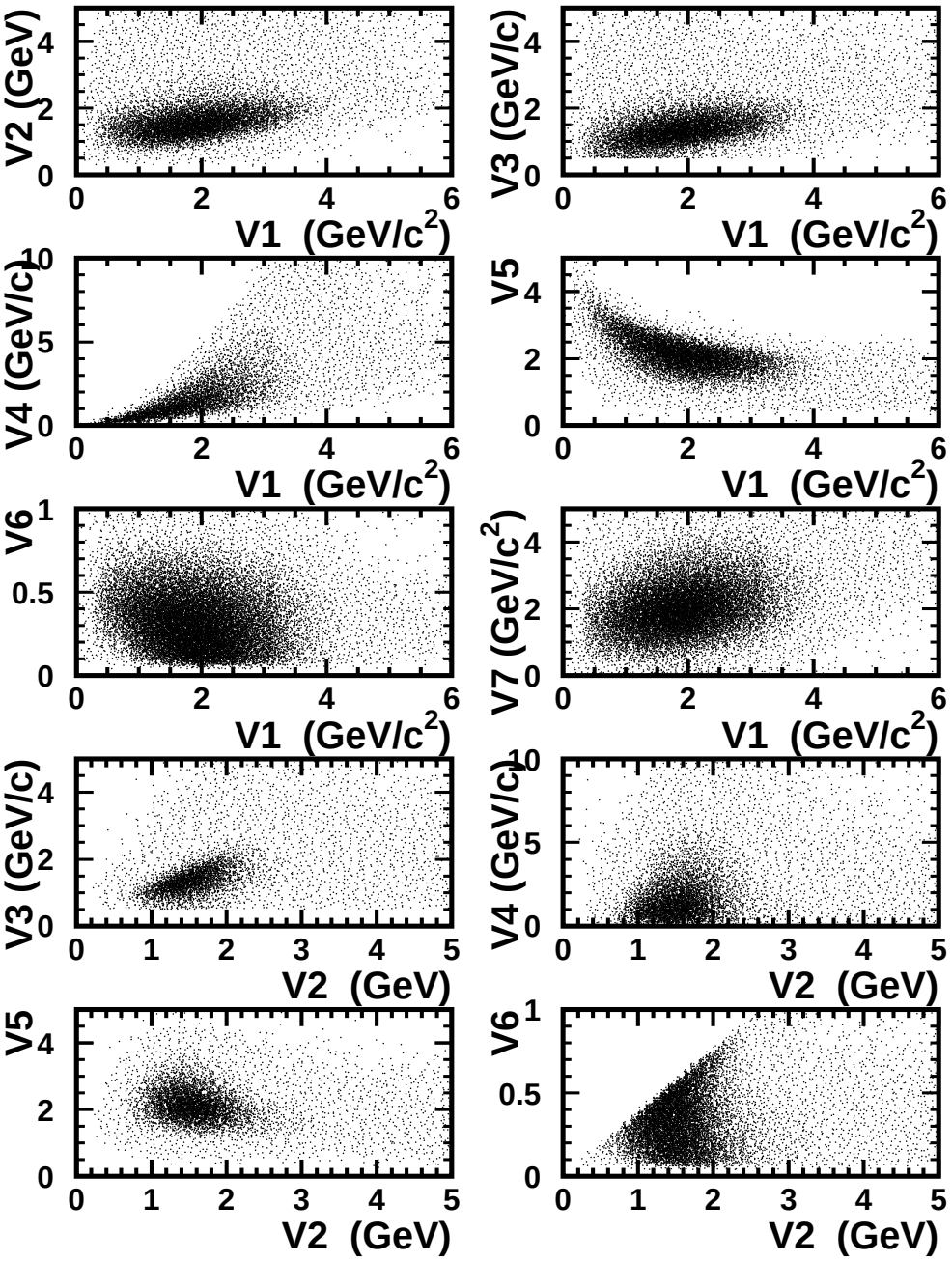

Figure 5.3: The correlations between different variables.

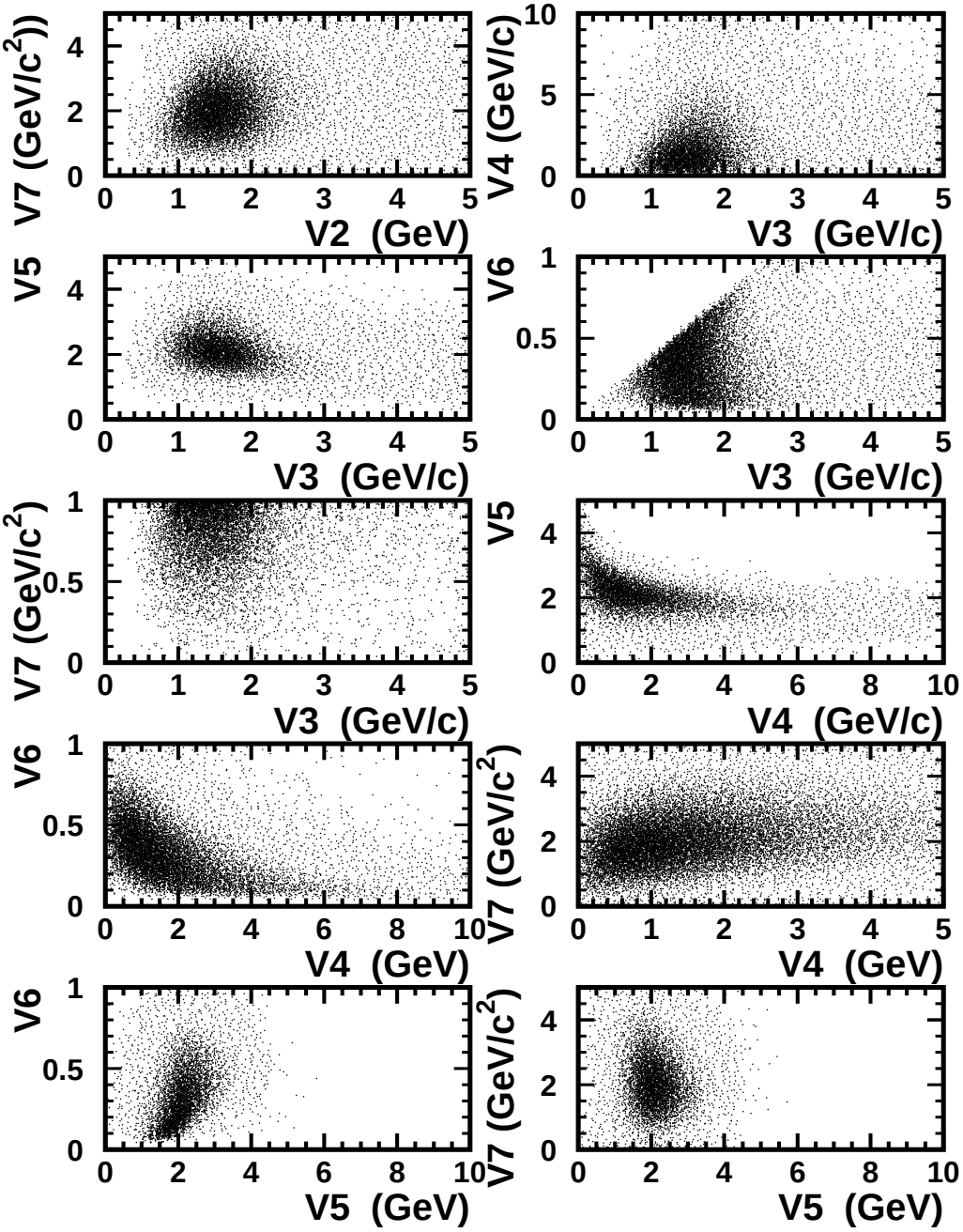

Figure 5.4: The correlations between different variables (continued).

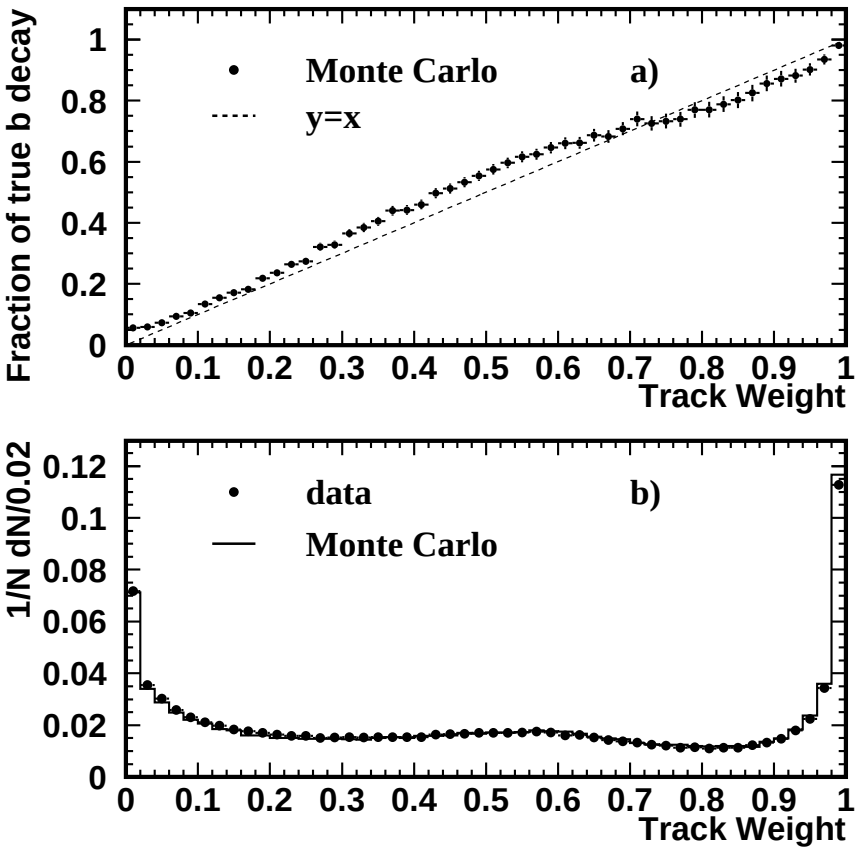

Figure 5.5: **a,b.** **a** Fraction of true b decay *vs* track weight from Monte Carlo simulated events; **b** comparison of the track weight between OPAL data and Monte Carlo simulated events.

weight procedure. The rapidity of each cluster is calculated and then a weight is assigned according to the parameterization performed in several bins of its momentum. This weight represents the probability that this cluster comes from the b hadron rather than the fragmentation. The cluster weight is shown in Figure 5.6. Most neutral clusters are detected in the electromagnetic calorimeter. Only a small portion of neutral clusters are in the hadronic calorimeter. The parameterization from momentum underestimates the cluster weight in the hadronic calorimeter for the cluster weight of 0.0-0.2 region as shown in the top plot of Figure 5.6. As only a small fraction of neutral clusters is in the first two bins, the reconstructed hadronic invariant mass will not be affected. The hadronic mass of X_u system in $B \to X_u \ell\nu$ is expected to be smaller than the hadronic mass of X_c in $B \to X_c \ell\nu$ due to the smaller mass of the u quark.

5.1.2 The lepton energy in the b hadron rest frame

The b hadron direction is reconstructed using OPAL b reconstruction code [98]. The reconstruction is based on the principle of assigning weights to charged tracks and neutral clusters, which are the same as the weights used in the reconstruction of the hadronic invariant mass W_i in Equation 5.3. The b hadron momentum is then reconstructed by summing the weighted momenta of hadronic tracks and clusters, with the lepton in the hemisphere. The b hadron flight direction is determined by the vector of b hadron momentum. The b hadron flight direction can also be calculated from the primary vertex and the secondary vertex. The b hadron direction resolution can be improved by combining the direction obtained from the b hadron momentum and the flight direction. The combination method is simply based on the weight from the angular resolution of the b direction from the momentum sum method and the flight direction. The comparison of the reconstructed b hadron direction for the data and the Monte Carlo simulation is shown in Figure 5.7. The difference between the reconstructed b hadron direction in

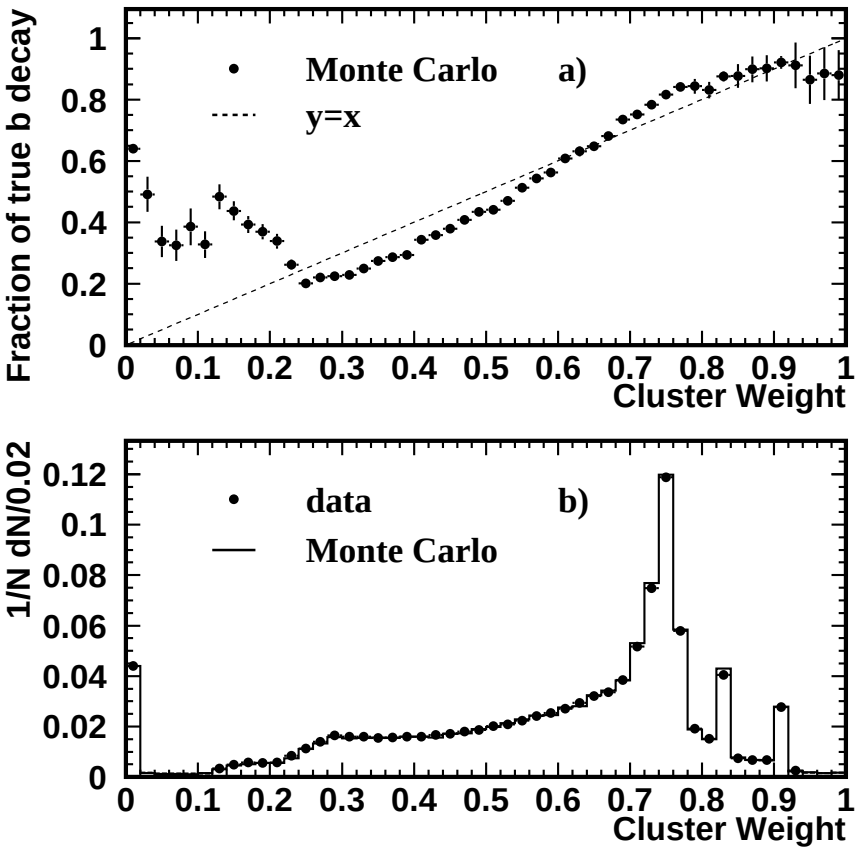

Figure 5.6: **a,b.** **a** Fraction of true b decay *vs* cluster weight from Monte Carlo simulated events; **b** comparison of the cluster weight between OPAL data and Monte Carlo simulated events.

Monte Carlo and the true b hadron direction in Monte Carlo is shown in Figure 5.8. The lepton energy in the lab frame is then boosted to the b hadron rest frame and is shown in the second plot of Figure 5.1.

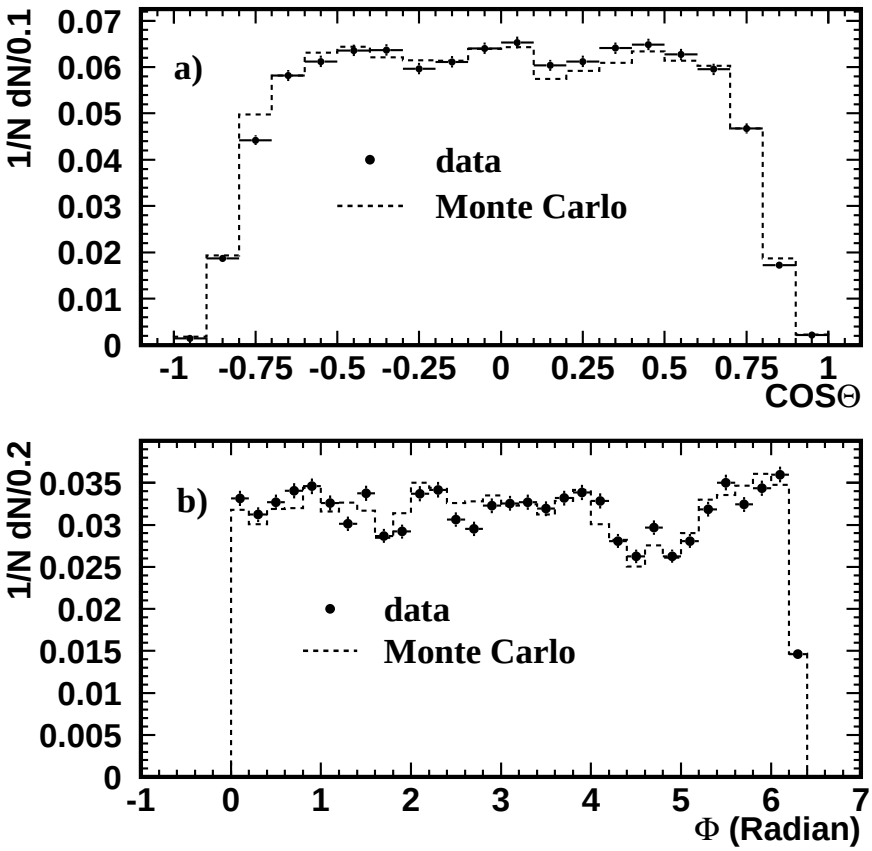

Figure 5.7: **a,b.** The b hadron **a** $\cos\theta$ direction and **b** ϕ direction comparison between OPAL data and Monte Carlo simulated events.

5.2 Discussion of b to u neural network outputs

Twelve thousand $b \to X_u \ell\nu$ events, which are simulated with the hybrid model described in Chapter 3 and which have passed the event preselection, and as many background

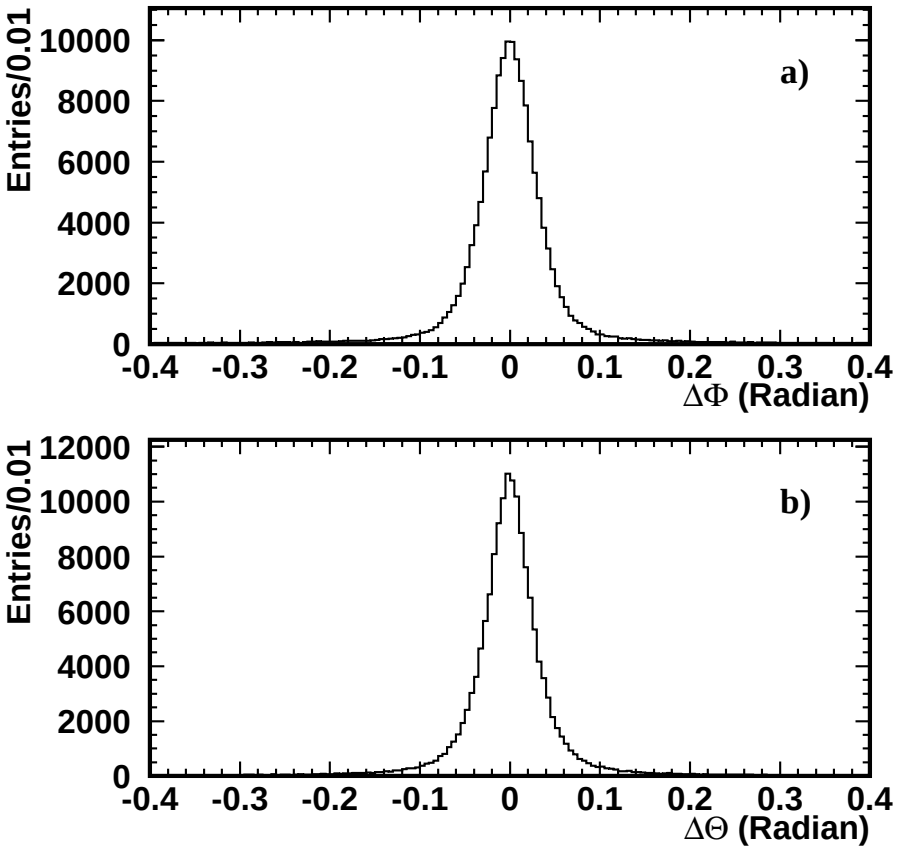

Figure 5.8: **a,b.** The difference between the reconstructed b hadron direction and the true b hadron direction in Monte Carlo simulated events for **a** θ and **b** ϕ.

events from the multi-hadron $Z \to q\bar{q}$ Monte Carlo simulation after the preselection are used to train the $b \to X_u \ell\nu$ neural network. Two other samples of signal and background events of the same size are used to test the neural network performance. The neural network output distributions from $b \to X_u \ell\nu$ and background are shown in Figure 5.9. Ninety percent of the background in this analysis comes from the $b \to X_c \ell\nu$ decay, 6.8%

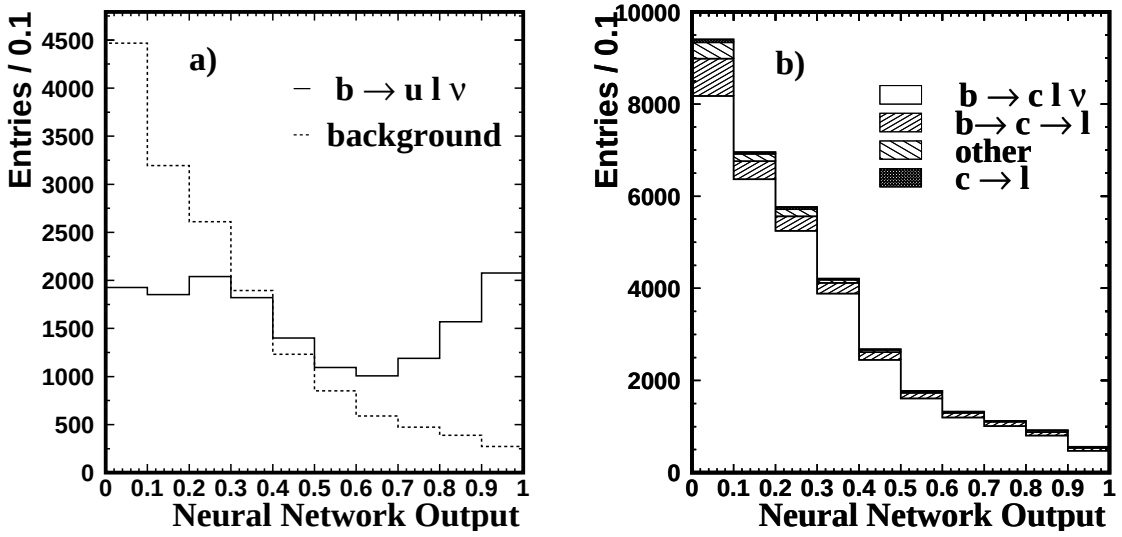

Figure 5.9: **a,b.** The b to u neural network output distributions, **a** for b to u signal and background, **b** for different background components.

from the b → c decay with the c subsequently decaying to a lepton. Another 0.6% comes from the c → ℓ decay in which the c quark is the primary quark. Other background processes make up the remaining 2.6%, of which 36% is from the b → τ decay with the τ subsequently decaying to an electron or a muon, and most of the rest of the "other" background is from a pion or a kaon misidentified as an electron or a muon.

The figure of merit for signal and background *vs* epochs for the training and test samples are shown in Figure 5.10a. It can be seen that the neural network learns quickly and reaches good performance after several epochs and the figures of merit of the training sample and test sample are similar. The number of training epochs should not be chosen

too high as the neural network will become over-trained in the high epochs and the figure of merit will drop gradually. The choice of training epochs is not critical and is chosen as 30 in this neural network training. The signal purity and efficiency *vs* neural network

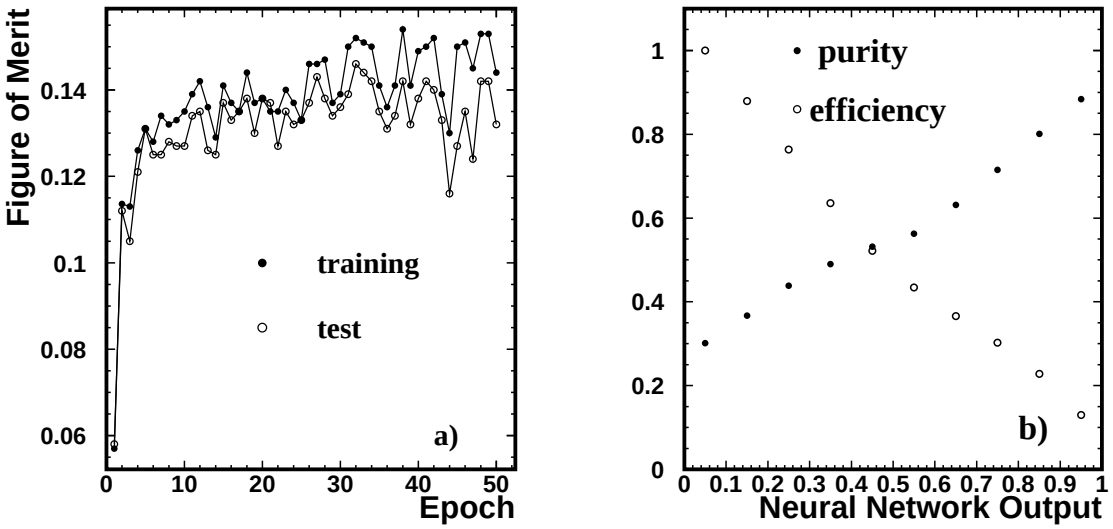

Figure 5.10: **a,b. a** The figure of merit between the signal and the background *vs* epochs for the training and test samples; **b** the signal purity and efficiency *vs* the b to u neural network output for the training sample.

output for the training sample are shown in Figure 5.10b. The agreement between the training sample and the test sample from the $b \to X_u \ell\nu$ neural network output are shown in Figure 5.11.

The $b \to X_u \ell\nu$ signal is divided into $B \to \pi\ell\nu$, $B \to \rho\ell\nu$, $B \to \eta\ell\nu$ and $B \to \omega\ell\nu$ and the corresponding neural network outputs are shown in Figure 5.12. The neural network outputs for the exclusive model and the inclusive model used in the hybrid model are shown in Figure 5.13. The neural network outputs from $B \to D\ell\nu$, $B \to D^*\ell\nu$ and $B \to D^{**}\ell\nu$ in the background are shown in Figure 5.14.

The signal $b \to X_u \ell\nu$ purity in the last bin of the neural network distribution is expected to be higher than in all other bins. This corresponds to a lower hadronic

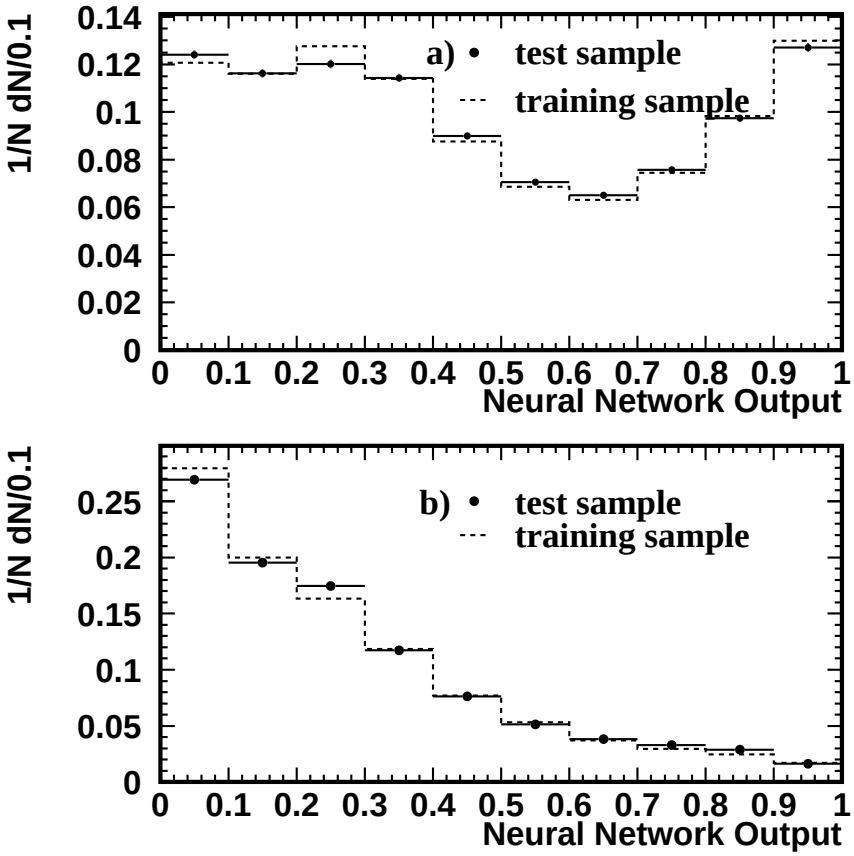

Figure 5.11: **a,b.** Comparison of neural network output distributions for **a** the signal and **b** the background of the training sample and test sample.

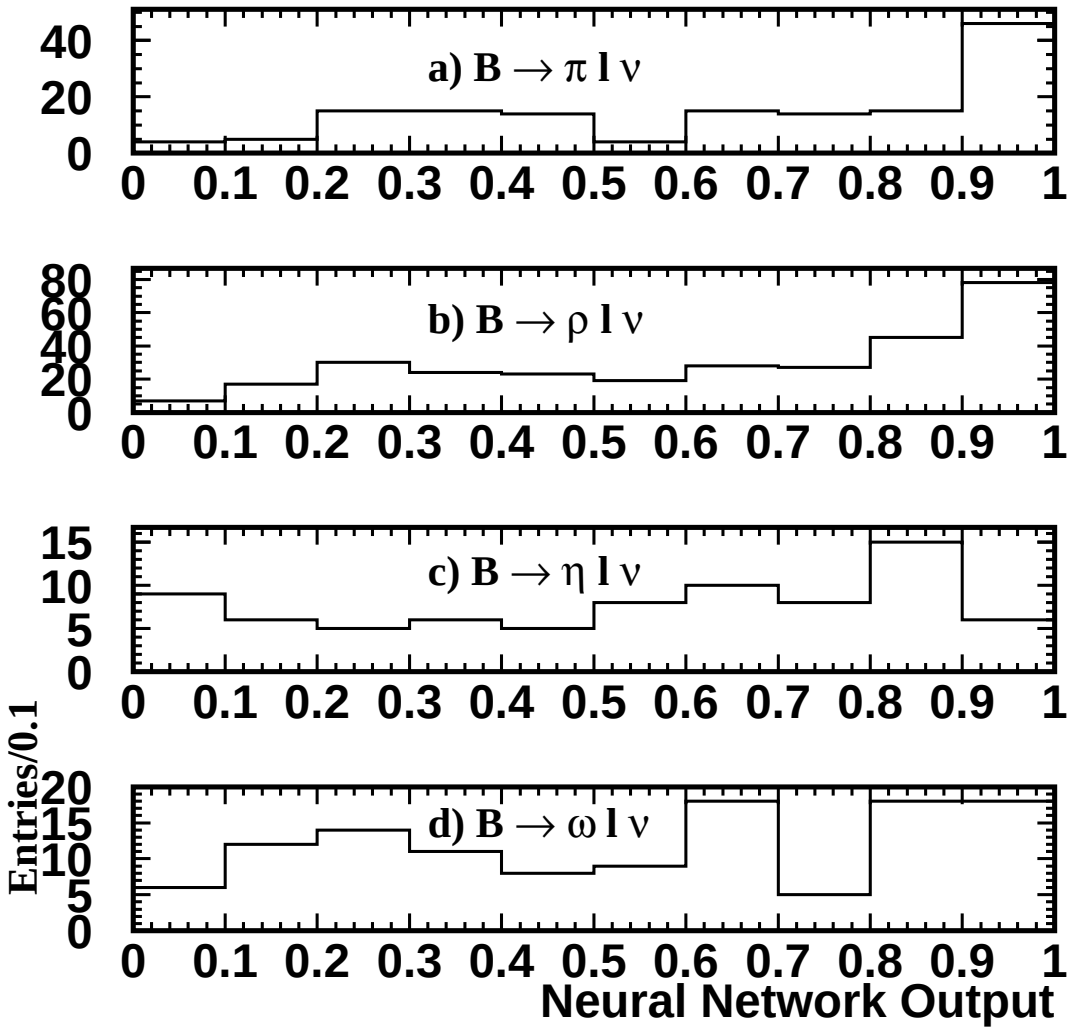

Figure 5.12: **a,b,c,d.** The neural network output distributions for **a** B to π, **b** B to ρ, **c** B to η and **d** B to ω semileptonic decay.

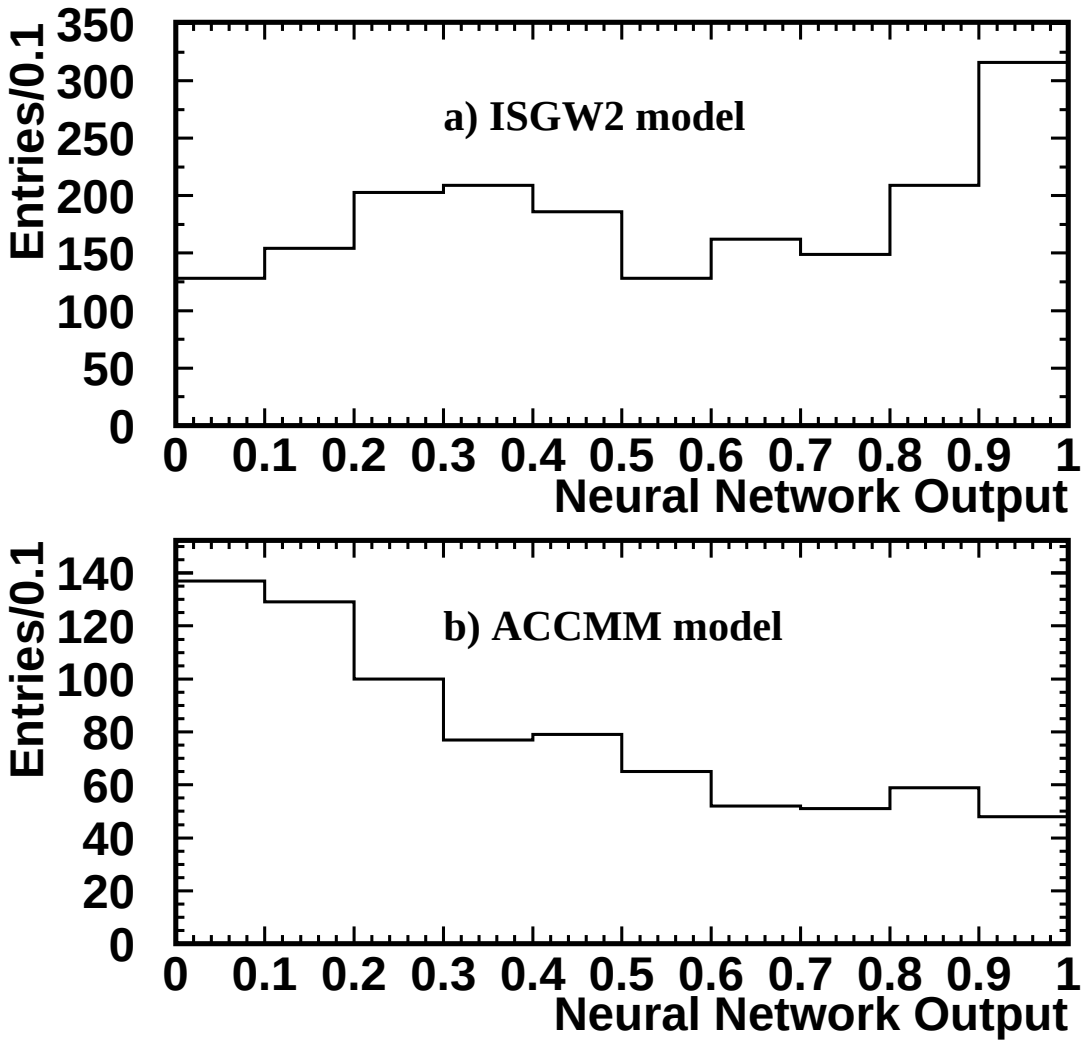

Figure 5.13: **a,b.** The neural network output distributions for **a** the ISGW2 model **b** the ACCMM model in the hybrid model.

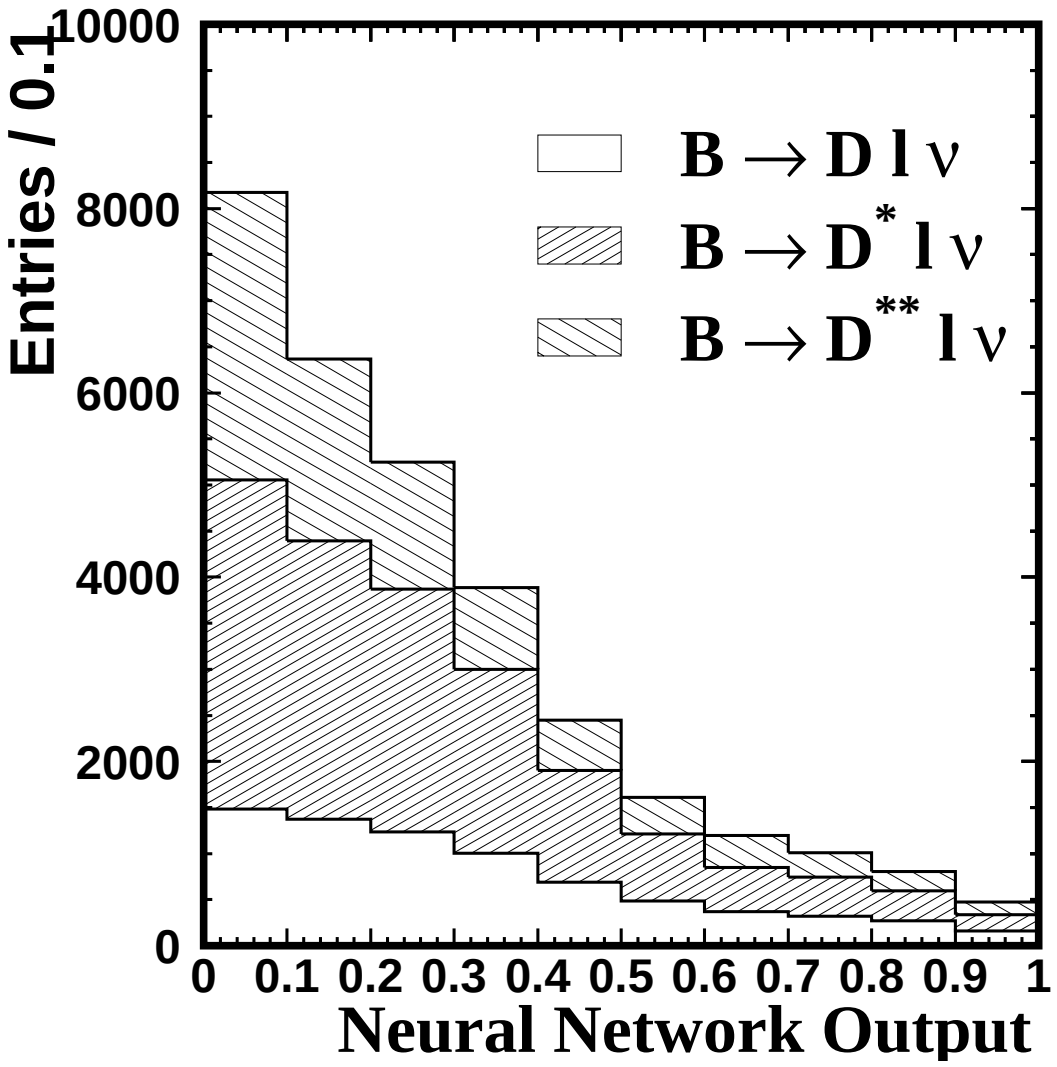

Figure 5.14: The neural network output distributions for B to D, D^* and D^{**} semileptonic decays.

invariant mass and a higher lepton momentum in the b hadron rest frame in the last bin compared to all other bins from the data, as on average the sample has lower hadronic invariant mass and higher lepton momentum in the b hadron rest frame. This is shown in Figure 5.15.

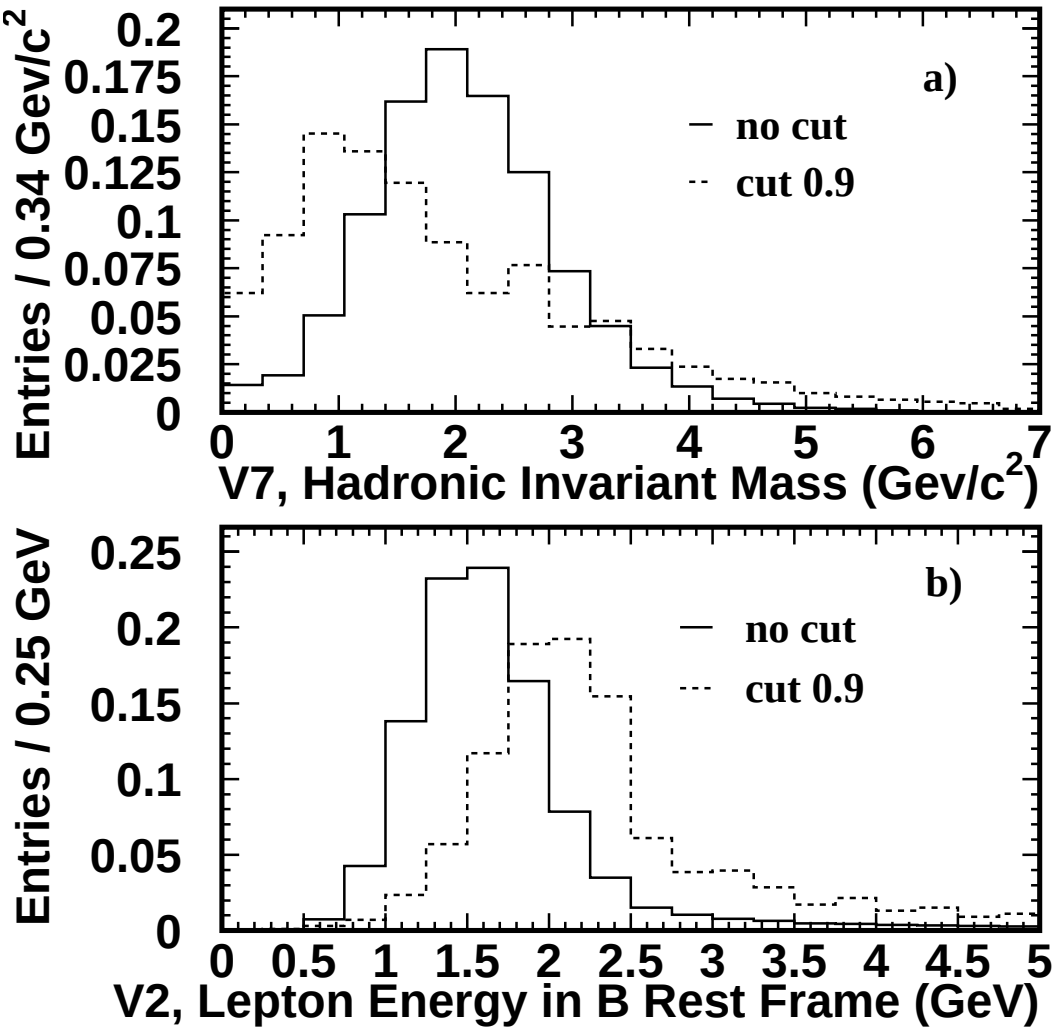

Figure 5.15: **a,b.** **a** The hadronic invariant mass from OPAL data, **b** the lepton energy in the b hadron rest frame from OPAL data, with no b to u neural network cut and with b to u neural network cut 0.9 applied.

Chapter 6

Results

This chapter describes the measurement of $\mathrm{Br}(b \to \mathrm{X_u}\ell\nu)$ using the $b \to \mathrm{X_u}\ell\nu$ neural network. The systematic error analysis and cross checks of $\mathrm{Br}(b \to \mathrm{X_u}\ell\nu)$ are presented. The extraction of $|\mathrm{V_{ub}}|$ from $\mathrm{Br}(b \to \mathrm{X_u}\ell\nu)$ is discussed.

6.1 The branching ratio of b to u semileptonic decay

The branching fraction of $b \to \mathrm{X_u}\ell\nu$ decay can be obtained from the best fit of the Monte Carlo simulated events to OPAL data based on the $b \to \mathrm{X_u}\ell\nu$ neural network output distributions. $\mathrm{Br}(b \to \mathrm{X_u}\ell\nu)$ is extracted from the $b \to \mathrm{X_u}\ell\nu$ neural network output distributions by minimizing:

$$\chi^2 = \sum_{\mathrm{k}} \frac{[\mathrm{N_k^{data}} - \mathrm{N_{data}}(x\mathrm{f_k^{MC_{bu}}} + (1-x)\mathrm{f_k^{MC_{bg}}})]^2}{\mathrm{N_k^{data}}}, \tag{6.1}$$

where $\mathrm{N_k^{data}}$ is the number of events from the data in the $\mathrm{k^{th}}$ bin of the $b \to \mathrm{X_u}\ell\nu$ neural network output. $\mathrm{N_{data}}$ is the total number of events in the data after preselection. The free parameter x is the fraction of signal events in the data after preselection, which can be converted to $\mathrm{Br}(b \to \mathrm{X_u}\ell\nu)$ based on the number of signal events and the number of background events in the Monte Carlo simulation after preselection. $\mathrm{f_k^{MC_{bu}}}$ is the

fraction of simulated signal events in the k^{th} bin of the $b \to X_u \ell\nu$ neural network output with respect to the total number of simulated signal events after preselection. $f_k^{MC_{bg}}$ is the fraction of simulated background events in the k^{th} bin of the $b \to X_u \ell\nu$ neural network output with respect to the total number of simulated background events after preselection. Here the background includes $b \to X_c \ell\nu$, $b \to c \to \ell$, $c \to \ell$ and other contributions. The sum over the index k is performed from the neural network cut to the last bin in the neural network output distribution. The $Br(b \to X_u \ell\nu)$ from the fit result x, as well as its statistical and systematic errors, depends on the $b \to X_u \ell\nu$ neural network cut. The resulting $Br(b \to X_u \ell\nu)$ is stable, with variations less than 0.24×10^{-3} as the neural network cut varies in value from 0.3 to 0.8. A neural network cut of 0.7 is chosen to minimize the total relative errors and yields

$$Br(b \to X_u \ell\nu) = (1.63 \pm 0.53) \times 10^{-3},$$

where the uncertainty is the statistical error only. The total relative errors are defined as the combination of the statistical error and the systematic error of $Br(b \to X_u \ell\nu)$ divided by $Br(b \to X_u \ell\nu)$ and are also shown in Table 6.1.

In Figure 6.1, the neural network output from the Monte Carlo simulation events with no $b \to X_u \ell\nu$ semileptonic decay is shown and the excess of events in the data can be seen in the highest bin. Here the Monte Carlo sample is normalized to the same number of entries as the data. The last bin of neural network output from the data contains 869 events. According to the Monte Carlo simulation, there would be 775 events in the last bin without the $b \to X_u \ell\nu$ semileptonic transition. The excess of events in that bin is 94 ± 31. The χ^2/ndf is 14.6/9, which corresponds to a 10% confidence level when one presumes no contributions from $b \to X_u \ell\nu$ transition. Here the χ^2 is calculated using all bin information. When the $b \to X_u \ell\nu$ transition is incorporated in the Monte Carlo simulation with a branching fraction of 1.63×10^{-3}, the Monte Carlo simulation agrees

Neural network cut	$\mathrm{Br}(b \to \mathrm{X_u}\ell\nu)$ $\times 10^{-3}$	Statistical error $\times 10^{-3}$	Systematic error $\times 10^{-3}$	Total relative error
0	1.45	0.52	$^{+0.82}_{-0.87}$	$^{+67\%}_{-70\%}$
0.1	1.51	0.53	$^{+0.62}_{-0.73}$	$^{+54\%}_{-60\%}$
0.2	1.50	0.53	$^{+0.61}_{-0.70}$	$^{+54\%}_{-59\%}$
0.3	1.54	0.53	$^{+0.59}_{-0.67}$	$^{+51\%}_{-55\%}$
0.4	1.55	0.53	$^{+0.59}_{-0.65}$	$^{+51\%}_{-54\%}$
0.5	1.57	0.53	$^{+0.60}_{-0.68}$	$^{+51\%}_{-55\%}$
0.6	1.60	0.53	$^{+0.57}_{-0.66}$	$^{+49\%}_{-53\%}$
0.7	1.63	0.53	$^{+0.55}_{-0.62}$	$^{+47\%}_{-50\%}$
0.8	1.78	0.62	$^{+0.62}_{-0.72}$	$^{+49\%}_{-53\%}$
0.9	2.03	0.72	$^{+0.72}_{-0.80}$	$^{+50\%}_{-53\%}$

Table 6.1: Results of different neural network cuts to get the branching fraction of b to u semileptonic decay.

much better with the data, as can be seen in the right plot of Figure 6.1. The χ^2/ndf is then 8.3/8, corresponding to a 41% confidence level.

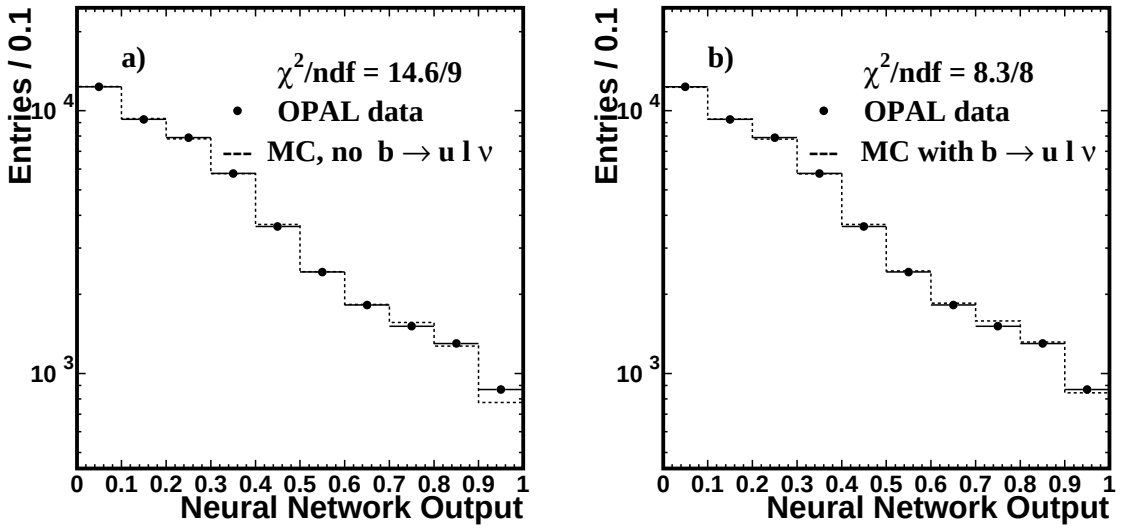

Figure 6.1: **a,b.** The neural network output distributions for OPAL data and Monte Carlo simulated events, **a** with no b to u semileptonic transition in the Monte Carlo simulated events, **b** with a branching fraction of 1.63×10^{-3} b to u semileptonic decay incorporated. The distribution of Monte Carlo simulated events is normalized to the data for both plots.

The data after subtracting the background from the Monte Carlo simulated events agree well with the simulated $b \to \mathrm{X_u}\ell\nu$ signal within statistical errors, which is shown in Figure 6.2.

6.2 Systematic errors and cross check

The list of systematic errors on $\mathrm{Br}(b \to \mathrm{X_u}\ell\nu)$ is given in Table 6.2. Unless otherwise specified, the systematic errors are evaluated by varying each parameter described by $\pm 1\sigma$ and taking the corresponding largest errors. A detailed description of these systematic errors are presented in Section 6.2.1 and a series of cross checks are performed and

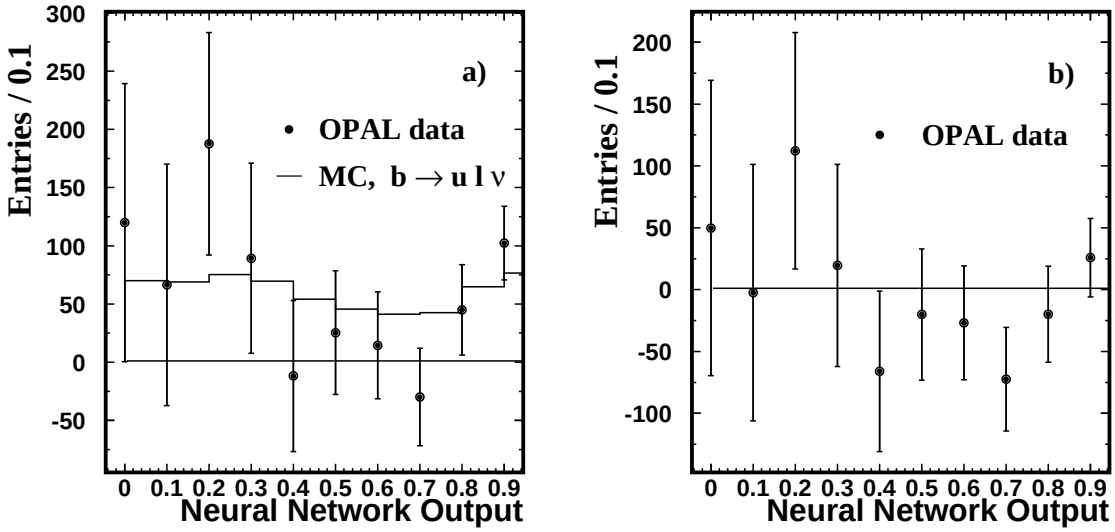

Figure 6.2: **a,b.** The neural network output distributions. **a** Data after subtracting the background from the Monte Carlo simulated event (points) show agreement with the simulated b to u signal (solid histogram). **b** Data after subtracting the Monte Carlo simulated events with a branching fraction of 1.63×10^{-3} b to u decay incorporated. Here the error bars include the statistical error from data and Monte Carlo simulated events.

presented in Section 6.2.2.

6.2.1 Systematic errors

The resulting systematic error in Table 6.2 is discussed in detail:

b quark fragmentation: Many parameterizations have been suggested to describe the heavy quark fragmentation process. The Peterson function [29] is used here to simulate the b and c quark fragmentation in the Monte Carlo simulation. The systematic error in the b quark fragmentation is estimated by varying the b hadron mean scaled energy $\langle x_E \rangle_b$ within the experimental range 0.702 ± 0.008 [99] recommended by the LEP Electroweak Working Group [99]. This value is consistent with a recent determination of $\langle x_E \rangle_b = 0.714 \pm 0.009$ from SLD [100].

The systematic error is also estimated from the Collins and Spiller fragmentation function [30] and Kartvelishvili fragmentation function [31] which are discussed below. The largest deviations are taken as systematic errors. The uncertainties of parameters from different fragmentation models are discussed below, where z is defined in Equation 2.4.

1. The Peterson function [29]:

$$f(z) = \frac{N}{z(1 - \frac{1}{z} - \frac{\epsilon_q}{1-z})^2}, \tag{6.2}$$

where N is the normalization factor. The ϵ_q in b fragmentation from Z peak is $0.0047\ ^{+0.0010}_{-0.0008}$ [2]. From the OPAL measurement, the b hadron mean scaled energy $\langle x_E \rangle_b$ is 0.702 ± 0.008, corresponding to a value of $\epsilon_q = 0.0038\ ^{+0.0010}_{-0.0008}$. For c quark fragmentation, $\langle x_E \rangle_c$ is 0.484 ± 0.008, which corresponds to $\epsilon_q = 0.031 \pm 0.006$.

2. The function from Collins and Spiller [30]:

$$f(z) = N(\frac{1-z}{z} + \frac{(2-z)\epsilon}{1-z})(1+z^2)(1 - \frac{1}{z} - \frac{\epsilon}{1-z})^{-2}, \tag{6.3}$$

Error Source	Variation or value and variation	$\Delta\mathrm{Br}(b \to \mathrm{X_u}\ell\nu)$ 10^{-3}
Fragmentation $\langle \mathrm{x_E} \rangle_\mathrm{b}$	0.702 ± 0.008 [99]	$^{+0.28}_{-0.32}$
Lepton spectrum (b $\to$ c)	ISGW** [35], ISGW [34]	$^{+0.18}_{-0.29}$
MC statistics	(see text)	± 0.22
b and c hadron semileptonic decay	(see text)	± 0.19
MC modeling	(see text)	± 0.19
$b \to \mathrm{X_u}\ell\nu$ modeling error (hybrid)	(see text)	± 0.19
$b \to \mathrm{X_u}\ell\nu$ modeling error (inclusive)	Parton [58], QCD [55]	± 0.14
$b \to \mathrm{X_u}\ell\nu$ modeling error (exclusive)	ISGW2 [37], JETSET [15]	± 0.07
Tracking resolution	$\pm 10\%$ [89]	± 0.07
c hadron decay multiplicity	(see text)	± 0.07
Λ_b production rate	$(11.6 \pm 2.0)\%$ [2]	∓ 0.04
Λ_b polarization	$-0.56\ ^{+0.22}_{-0.16}$ [69]	± 0.03
Electron ID efficiency	$\pm 4\%$ [89]	∓ 0.04
Muon ID efficiency	$\pm 2\%$ [95]	∓ 0.03
Electron fake rate	$\pm 21\%$ [89]	∓ 0.02
Muon fake rate	$\pm 8\%$ [89]	∓ 0.01
$\mathrm{Br}(b \to \mathrm{X}\tau\bar{\nu}_\tau)$	$(2.6 \pm 0.4)\%$ [2]	± 0.01
b lifetime	(1.564 ± 0.014) ps [2]	< 0.01
$\mathrm{R_b}$	0.21644 ± 0.00075 [2]	< 0.01
Total		$^{+0.55}_{-0.62}$

Table 6.2: Systematic errors for the branching fraction of b to u semileptonic decay.

where N is the normalization factor. For b quark fragmentation, ϵ is equal to (3.42 $\pm$ 0.62)$\times 10^{-3}$, corresponding to $\langle x_E \rangle_b = 0.698 \pm 0.004$ [95]. For c quark fragmentation, ϵ is equal to 0.059 $\pm$ 0.032, corresponding to $\langle x_E \rangle_c = 0.473 \pm 0.017$ [101].

3. The Kartvelishvili *et al.* [31] function:

$$f(z) = N z^{\alpha}(1-z), \tag{6.4}$$

where N is the normalization factor. For b quark fragmentation, α is equal to 10.04 $\pm$ 0.57 corresponding to $\langle x_E \rangle_b = 0.720 \pm 0.005$ [95]. For c quark fragmentation, α is equal to 4.02 $\pm$ 0.78 corresponding to $\langle x_E \rangle_c = 0.484 \pm 0.018$ [101].

4. The Lund symmetric function [32]:

$$f(z) = N \frac{1}{z}(1-z)^{a} exp[-\frac{bM_T^2}{z}], \tag{6.5}$$

where N is the normalization factor. b quark fragmentation for this function is not studied yet. For c quark fragmentation, a is equal to 0.18 and bM_T^2 is equal to 1.55 ± 0.36 corresponding to $\langle x_E \rangle_c = 0.478 \pm 0.018$ [101].

The systematic error for $Br(b \to X_u \ell \nu)$ from c quark fragmentation can be neglected because there is a very small background from $c \to \ell$, where c is a primary quark.

***b* $\to X_c \ell \nu$ lepton momentum spectrum modeling:** Different decay models are used to predict the lepton spectrum in the b hadron rest frame for the $b \to X_c \ell \nu$ decay. Although all models are derived for B^0 and B^+ semileptonic decay only, they are extrapolated to the B_s and Λ_b semileptonic decays. This will be correct in the simple spectator model and is a reasonable approximation for this analysis. The lepton spectrum from the ACCMM model [54] is used as a base model for the $b \to X_c \ell \nu$ decay. In ACCMM model, the spectator quark in the B meson has momentum distribution $f(p) = \frac{4}{\sqrt{\pi} P_F^3} e^{\frac{-p^2}{p_F^2}}$, where p_F is the Fermi momentum. The

CLEO Collaboration [103] has fit the ACCMM model to their data to determine p_F equal to 298 MeV/c.

The systematic errors due to $b \to X_c \ell\nu$ lepton momentum spectrum modeling are estimated from the ISGW [34] and ISGW** [35] models.

The lepton spectrum from the $b \to c \to \ell$ decay in the ACCMM model is different from the ISGW model. The systematic error due to the shape of the $b \to c \to \ell$ lepton spectrum is calculated and is found to be negligible. The lepton spectrum from the $c \to \ell$ decay is varied from the ACCMM model to the ISGW model, where the c quark is a primary quark from Z decay. The systematic error is calculated and found to be negligible.

Monte Carlo statistics: The systematic uncertainty due to the limited Monte Carlo statistics is $\pm 0.22 \times 10^{-3}$.

***b* and *c* hadron decay properties:** The systematic error is estimated from the uncertainties of the branching fractions of $B^0 \to D^- \ell^+ \nu$, $B^0 \to D^{*-} \ell^+ \nu$, $B^+ \to \bar{D}^0 \ell^+ \nu$, $B^+ \to \bar{D}^{*0} \ell^+ \nu$, $\bar{B} \to D^{**} \ell\nu$ and $\Lambda_b \to \Lambda_c X \ell\nu$. There is a 6.8% background contribution from the $b \to c \to \ell$ decays and a 0.6% background contribution from the $c \to \ell$ decays. The systematic error is also estimated from the uncertainty of the branching fraction of the $b \to c \to \ell$ decays. A summary of the systematic errors from the uncertainties of b hadron and c hadron semileptonic decay branching ratios is shown in Table 6.3. The $Br(\bar{B} \to D^{**} \ell\nu)$ in Table 6.3 is obtained by averaging the $Br(\bar{B} \to D^{**} \ell\nu)$ from ARGUS [105], ALEPH [106], DELPHI [107] and the total B semileptonic decay branching fraction subtracting the contribution from B to D and D^* semileptonic decay, described by the LEP, CDF and SLD Heavy Flavour Working Group [5]. For the decay of $\bar{B} \to D^{**} \ell\nu$, in which D^{**} refers to D_1, D_2^*, D_2 and D_1^*, the branching ratio for each specific D^{**} final state is not well measured.

For this analysis, the narrow final states of D^{**} in $\bar{B} \to D^{**}\ell\nu$ are replaced by the broad states and then vice-versa to check the sensitivity of the $Br(b \to X_u\ell\nu)$ to the relative ratio of the narrow and broad states of D^{**} in $\bar{B} \to D^{**}\ell\nu$. The effect on the $Br(b \to X_u\ell\nu)$ is found to be negligible.

Error Source	Variation	$\Delta Br(b \to X_u\ell\nu)(10^{-3})$
$Br(B^0 \to D^-\ell^+\nu)$	$(2.10 \pm 0.19)\%$ [2]	∓ 0.02
$Br(B^0 \to D^{*-}\ell^+\nu)$	$(4.60 \pm 0.27)\%$ [2]	± 0.03
$Br(B^+ \to \bar{D}^0\ell^+\nu)$	$(2.15 \pm 0.22)\%$ [2]	∓ 0.06
$Br(B^+ \to \bar{D}^{*0}\ell^+\nu)$	$(5.3 \pm 0.8)\%$ [2]	± 0.04
$Br(\bar{B} \to D^{**}\ell\nu)$	$(3.04 \pm 0.44)\%$ [5]	± 0.16
$Br(b \to c \to \ell)$	$(8.4\ ^{+0.42}_{-0.39})\%$ [95]	∓ 0.02
$Br(\Lambda_b \to \Lambda_c X\ell\nu)$	$(7.9 \pm 1.9)\%$ [2]	∓ 0.06
Total		± 0.19

Table 6.3: Systematic errors for the branching fraction of b to u semileptonic decay from uncertainties of the b hadron and c hadron semileptonic decay branching ratios.

Monte Carlo modeling errors: The systematic error for the Monte Carlo modeling errors is estimated by re-weighting each input variable distribution in the Monte Carlo simulation to agree with the corresponding data distributions. A branching fraction of 1.63×10^{-3} for the $b \to X_u\ell\nu$ transition is incorporated in the Monte Carlo simulation. This gives a conservative estimate of the systematic uncertainty due to the modeling of the input variables.

***b* $\to X_u\ell\nu$ modeling error from the hybrid model:** The boundary between the inclusive and exclusive regions in the hybrid model is varied from 1.5 GeV/c^2 to 0.9 GeV/c^2. This conservatively estimates the systematic error arising from the placement of the boundary between the inclusive and exclusive models. This produces

an uncertainty of $\pm 0.19 \times 10^{-3}$ for Br($b \to X_u \ell\nu$).

$b \to X_u \ell\nu$ inclusive model: The QCD universal function model and the parton model are used to evaluate the systematic errors in the inclusive part of the $b \to X_u \ell\nu$ hybrid model. This gives a change of -0.14 $\times$ 10^{-3} for the QCD universal function model and $+0.02 \times 10^{-3}$ for the parton model for the branching ratio of $b \to X_u \ell\nu$. The largest variation is taken as the systematic uncertainty.

$b \to X_u \ell\nu$ exclusive model: The model implemented in the OPAL JETSET [16] Monte Carlo simulation, which has the u quark and the spectator quark forming one single hadron in the final state, is used to estimate the systematic error in the exclusive part of the $b \to X_u \ell\nu$ hybrid model.

Tracking resolution: The systematic error due to the uncertainties of the detector resolution is estimated by applying a $\pm 10\%$ variation to the r-ϕ track parameters and an independent $\pm 10\%$ variation to the analogous parameters in the r-z plane to the Monte Carlo simulated events.

***c* hadron decay multiplicity:** The systematic error of the Br($b \to X_u \ell\nu$) associated with the c hadron decay charge multiplicity is estimated using the average charged track multiplicity of D^+, D^0, D_s^+ decays as measured by MARK III [102]. The systematic uncertainty of the Br($b \to X_u \ell\nu$) is $\pm 0.07 \times 10^{-3}$ from the uncertainty of c hadron decay multiplicity. The systematic error of Br($b \to X_u \ell\nu$) associated with D decay charge multiplicity is shown in Table 6.4.

Λ_b production rate: The PDG [2] gives the production fraction of B^+, B^0, B_s^0 and Λ_b in Z decay as (38.9 $\pm$ 1.3)%, (38.9 $\pm$ 1.3)%, (10.7 $\pm$ 1.4)% and (11.6 $\pm$ 2.0)%. The neural network output variable distributions among B^+, B^0 and B_s^0 are similar and the systematic effects caused by the uncertainties of the production fraction of

Error Source	Variation	$\Delta\mathrm{Br}(b \to \mathrm{X_u l}\nu)(10^{-3})$
$\mathrm{D}^0 \to 0$ prong	0.054 ± 0.011 [102]	± 0.06
$\mathrm{D}^0 \to 2$ prong	0.634 ± 0.015 [102]	<0.01
$\mathrm{D}^0 \to 4$ prong	0.293 ± 0.023 [102]	<0.01
$\mathrm{D}^0 \to 6$ prong	0.019 ± 0.009 [102]	<0.01
$\mathrm{D}^+ \to 1$ prong	0.384 ± 0.023 [102]	<0.01
$\mathrm{D}^+ \to 3$ prong	0.541 ± 0.023 [102]	<0.01
$\mathrm{D}^+ \to 5$ prong	0.075 ± 0.015 [102]	<0.01
$\mathrm{D_s^+} \to 1$ prong	0.37 ± 0.10 [102]	± 0.04
$\mathrm{D_s^+} \to 3$ prong	0.42 ± 0.15 [102]	<0.01
$\mathrm{D_s^+} \to 5$ prong	0.21 ± 0.11 [102]	<0.01
Total		± 0.07

Table 6.4: Systematic errors for the branching fraction of b to u semileptonic decay from uncertainties of the D decay multiplicity.

B^+, B^0 and B_s^0 are neglected. Due to the difference of the neural network output variable distributions between Λ_b and B mesons, the fraction of Λ_b is varied by a one standard deviation to determine the corresponding systematic error.

Λ_b polarization: According to the Standard Model, the b quark is longitudinally polarized with a large average value of $\langle P_L^b \rangle$ = -0.94 for a weak mixing angle of $\sin^2\theta_W = 0.23$ [104] in Z decay. Any b quark polarization information is lost in the B meson due to the fact that the B meson has spin 0. As Λ_b has spin $\frac{1}{2}$ and the b quark mass is heavy, Λ_b is expected to carry most of the b quark polarization. The lepton momentum spectrum from Λ_b semileptonic decays depends on the degree of Λ_b polarization. The systematic uncertainties are estimated by using the Λ_b polarization range $\langle P_L^{\Lambda_b} \rangle = -0.56\ ^{+0.22}_{-0.16}$ [69].

Lepton identification efficiency: The number of selected events in the signal and background depends on the electron identification efficiency and the muon identification efficiency. The electron identification efficiency has been studied using control samples of electrons from $e^+e^- \to e^+e^-$ events and photon conversions, and is modeled to a precision of 4.1% [89]. The muon identification efficiency has been studied using the muon pairs produced in two-photon collisions and $Z \to \mu^+\mu^-$ events, giving an uncertainty of 1.9% [95].

Lepton fake rate: Fake electrons in the electron sample are primarily from the charged hadrons (mainly charged pions) mis-identified as electrons and from untagged photon conversions. The uncertainty associated with electron mis-identification is ±21% [89]. The muon fake rate is studied from $K_s^0 \to \pi^+\pi^-$ and $\tau \to 3\pi$ decay. The uncertainty of the fake muon rate is estimated to be ±8%.

$b \to X\tau\nu_\tau$ branching ratio: One important composition in the "other" background in

Figure 5.9 results from a b quark semileptonic decay to a τ lepton with the τ lepton subsequently decaying to an electron or a muon. The branching ratio of $b \to \mathrm{X}\tau\nu_\tau$ is $(2.6 \pm 0.4)\%$ [2] and the systematic error is estimated using the uncertainties of the $b \to \mathrm{X}\tau\nu_\tau$ branching ratio.

Uncertainty of *b* lifetime: The average b hadron lifetime is measured to be (1.564 ± 0.014) ps [2]. The uncertainty in b lifetime results in a negligible uncertainty in $\mathrm{Br}(b \to X_u \ell\nu)$.

Uncertainty of $\mathrm{R_b}$: The fraction of $\mathrm{Z} \to \mathrm{b\bar{b}}$ events in hadronic Z decays, $\mathrm{R_b}$, is measured to be 0.21644 ± 0.00075 [2]. The uncertainty in $\mathrm{R_b}$ results in a negligible uncertainty in the background composition.

6.2.2 Cross checks of the result

The fit procedure is applied to the electron sample and the muon sample separately. The $\mathrm{Br}(b \to X_u \ell\nu)$ fitting result for the electron sample is $(1.33 \pm 0.86\ (\mathrm{stat})) \times 10^{-3}$ and the result for the muon sample is $(2.12 \pm 0.83\ (\mathrm{stat})) \times 10^{-3}$. The same procedure is also applied to the data between 1991 and 1993, and the data between 1994 and 1995, respectively. The $\mathrm{Br}(b \to \mathrm{X_u}\ell\nu)$ results are $(1.83 \pm 0.75\ (\mathrm{stat})) \times 10^{-3}$ and $(1.49 \pm 0.87\ (\mathrm{stat})) \times 10^{-3}$ for the data between 1991 and 1993 and the data between 1994 and 1995 respectively.

6.3 Measurement of $|V_{ub}|$ from the branching ratio of b to u semileptonic decay

The $b \to X_u \ell \nu$ decay width can be obtained from the Operator Product Expansion (OPE) [109, 110]:

$$\Gamma = \frac{G_F^2 m_b(\mu)^5}{192\pi^3}|V_{ub}|^2(A_0(1 - \frac{\mu_\pi^2 - \mu_G^2}{2m_b^2}) - 2\frac{\mu_G^2}{2m_b^2} + \mathcal{O}(\frac{1}{m_b^3})), \tag{6.6}$$

where G_F is the Fermi coupling constant and m_b is the b quark mass. μ is the normalization point for m_b. μ_π^2 is the average of the square of the heavy quark momentum inside the B hadron. μ_G^2 is the expectation value of the chromomagnetic operator. The leading order coefficient A_0 can be calculated from the partonic width free from bound-state nonperturbative corrections. The term starting with $1/m_b^2$ is the nonperturbative corrections. For the nonperturbative corrections, μ_G^2 is around 0.4 GeV^2 with the conservative estimated accuracy $\pm 25\%$. μ_π^2 is (0.6 ± 0.2) GeV^2. The perturbative expansion of the $b \to X_u \ell \nu$ decay width has the general form [109]:

$$\Gamma = \frac{G_F^2 m_b(\mu)^5}{192\pi^3}|V_{ub}|^2(1 + a_1\frac{\alpha(\tilde{\mu})}{\pi} + a_2\left(\frac{\alpha(\tilde{\mu})}{\pi}\right)^2 + a_3\left(\frac{\alpha(\tilde{\mu})}{\pi}\right)^3 + ...), \tag{6.7}$$

where $\tilde{\mu}$ is the normalization point for α_s. The value of low scale running mass $m_b(\mu)$ is translated to the scale μ of 1 GeV and $m_b(1\text{GeV})$ is assumed to be (4.58 ± 0.060) GeV/c^2 [111]. Combining the uncertainties from perturbative and non-perturbative corrections, the $b \to X_u \ell \nu$ decay width can be written as:

$$\Gamma = 66\text{ps}^{-1}|V_{ub}|^2(1 + 0.065\frac{m_b(1\text{GeV}) - 4.58\text{GeV}}{60\text{MeV}} \pm 0.02_{\text{pert}} \pm 0.035_{\text{nonpert}}). \tag{6.8}$$

The $|V_{ub}|$ can be derived as:

$$|V_{ub}| = 0.00442 \times \left(\frac{\text{Br}(b \to X_u \ell \nu)}{0.002}\frac{1.55\text{ps}}{\tau_b}\right)^{\frac{1}{2}} \times (1 \pm 0.025_{\text{QCD}} \pm 0.035_{m_b}), \tag{6.9}$$

where τ_{b} is the average b hadron lifetime. The uncertainty 0.025_{QCD} combined with the uncertainty from perturbative and non-perturbative corrections. $0.035_{\mathrm{m_b}}$ is from the uncertainty of the running of the b quark mass. The LEP working group slightly modified this formula by combining the work from another group [45] and produced [5, 113]:

$$|\mathrm{V_{ub}}| = 0.00445 \times \left(\frac{\mathrm{Br}(b \to \mathrm{X_u} \ell \nu)}{0.002} \frac{1.55\mathrm{ps}}{\tau_{\mathrm{b}}} \right)^{\frac{1}{2}} \times (1 \pm 0.010_{\mathrm{pert}} \pm 0.030_{1/\mathrm{m_b^3}} \pm 0.035_{\mathrm{m_b}}). \quad (6.10)$$

This formula is used in the calculation of $|\mathrm{V_{ub}}|$ in this analysis.

Chapter 7

Conclusion

The branching fraction of the inclusive $b \to X_u \ell\nu$ decay is measured to be:

$$\mathrm{Br}(b \to X_u \ell\nu) = (1.63 \pm 0.53\ (\mathrm{stat})\ ^{+0.55}_{-0.62}\ (\mathrm{sys})) \times 10^{-3}. \tag{7.1}$$

The first error 0.53 is the statistical error from the data only. The errors associated with the limited statistics of the Monte Carlo sample are included in the systematic error. This result is consistent with similar measurements from ALEPH, DELPHI and L3, the other three LEP experiments, shown in Table 7.1. In Table 7.1, the first error in $\mathrm{Br}(b \to X_u \ell\nu)$ combines the statistical error from the data and limited Monte Carlo statistics as well as the uncorrelated systematic uncertainties due to experimental systematic errors, such as detector resolution and lepton identification efficiency. The second error contains the systematic uncertainties from the $b \to X_c \ell\nu$ Monte Carlo simulation models. The third error contains the systematic uncertainties from the $b \to X_u \ell\nu$ models. The second and third errors are correlated between the various experiments. The $\mathrm{Br}(b \to X_u \ell\nu)$ from the DELPHI collaboration is revised by the LEP Heavy Flavour Working Group [5].

$|V_{ub}|$ can be obtained from $\mathrm{Br}(b \to X_u \ell\nu)$ using Equation 6.10 where the average b hadron

Experiment	$\mathrm{Br}(b \to \mathrm{X_u}\ell\nu)$ (10^{-3})	Ref
ALEPH	1.73 ± 0.56 (stat+det) ± 0.51 (b → c) ± 0.2 (b → u)	[10]
DELPHI	1.69 ± 0.53 (stat+det) ± 0.45 (b → c) ± 0.2 (b → u)	[11, 5]
L3	3.3 ± 1.3 (stat+det) ± 1.4 (b → c) ± 0.5 (b → u)	[12]
OPAL (This analysis)	1.63 ± 0.57 (stat+det) $^{+0.44}_{-0.52}$ (b → c) ± 0.25 (b → u)	

Table 7.1: The branching fractions of $b \to \mathrm{X_u}\ell\nu$ measured from ALEPH, DELPHI, L3 and this analysis.

lifetime τ_b is equal to (1.564 ± 0.014) ps[2]. Thus, $|\mathrm{V_{ub}}|$ obtained from this analysis is:

$$|\mathrm{V_{ub}}| = (4.00 \pm 0.65\ (\mathrm{stat})\ ^{+0.67}_{-0.76}\ (\mathrm{sys}) \pm 0.19\ (\mathrm{HQE})) \times 10^{-3}, \tag{7.2}$$

where the systematic error includes the b to u and b to c semileptonic decay modeling error, and the HQE error is purely the theoretical error from the Heavy Quark Expansion. This result is consistent with the $|\mathrm{V_{ub}}|$ value from the CLEO exclusive measurement of $(3.3 \pm 0.8\ (\mathrm{total})) \times 10^{-3}$ [4].

The four measurements of $\mathrm{Br}(b \to \mathrm{X_u}\ell\nu)$ from the LEP experiments are averaged using the Best Linear Unbiased Estimate technique [112, 113]. This technique provides an unbiased estimate of LEP $\mathrm{Br}(b \to \mathrm{X_u}\ell\nu)$ average result $\mathrm{Br_{LEP}}$:

$$\mathrm{Br_{LEP}} = \frac{\sum_{\mathrm{i}=1}^{4}\sum_{\mathrm{j}=1}^{4}\mathrm{Br_i}(\mathrm{E}^{-1})_{\mathrm{ij}}}{\sum_{\mathrm{i}=1}^{4}\sum_{\mathrm{j}=1}^{4}(\mathrm{E}^{-1})_{\mathrm{ij}}}, \tag{7.3}$$

where $\mathrm{Br_i}$ is the $\mathrm{Br}(b \to \mathrm{X_u}\ell\nu)$ from the four LEP experiments. E is the error matrix including the off-diagonal terms giving the correlations between the four LEP experiments. The LEP average $\mathrm{Br}(b \to \mathrm{X_u}\ell\nu)$ is obtained as [113]:

$$\mathrm{Br}(b \to \mathrm{X_u}\ell\nu) = 1.71 \pm 0.31(\mathrm{stat} + \mathrm{det}) \pm 0.37(\mathrm{b} \to \mathrm{c}) \pm 0.20(\mathrm{b} \to \mathrm{u}). \tag{7.4}$$

Using Equation 6.10, the average $|\mathrm{V_{ub}}|$ obtained from the four LEP experiments is:

$$|\mathrm{V_{ub}}| = (4.09 \pm 0.37\ (\mathrm{stat} + \mathrm{det}) \pm 0.44(\mathrm{b} \to \mathrm{c}) \pm 0.24(\mathrm{b} \to \mathrm{u}) \pm 0.19\ (\mathrm{HQE})) \times 10^{-3}. \tag{7.5}$$

The measurements of $|V_{ub}|$ will also be performed by the BaBar experiment at SLAC and the Belle experiment at KEK. Now the LEP average $|V_{ub}|$ is most precise measurement of $|V_{ub}|$ in the world. The more precise $|V_{ub}|$ measurements will be achieved by the BaBar and Belle experiments in the future as there will be more B events accumulated in BaBar and Belle than in LEP.

Appendix A

My Contribution to OPAL Collaboration

I was involved with the OPAL Collaboration from September, 1997 to October, 2001 as a part of University of British Columbia group. I spent a total of 14 months at CERN during this period. My contributions to OPAL Collaboration are listed below:

- I participated in OPAL data taking shifts each year from 1998 to 2000.
- As a member of OPAL Online ROPE (Reconstruction of OPAL Events) experts, I was in charge of the OPAL online event processing, data recording and offline event re-processing system. I also developed a graphical interface to execute Online Rope commands to make the operation of ROPE farm smoother and more friendly.
- I wrote the Monte Carlo simulation code for the $b \to X_u \ell \nu$ hybrid model and produced 200,000 Monte Carlo events on the OPAL Monte Carlo farm.
- I did a study in b quark fragmentation. The study result is used as a general tool for b fragmentation in OPAL heavy flavour group.

- I represented OPAL to present a talk about "Measurement of $|V_{cb}|$ using $B^0 \to D^* \ell \nu$ decays" in year 2000 APS April meeting in Long Beach, USA. I also presented a talk about " Measurement of $|V_{ub}|$ using b semileptonic decay" at APS Northwest Section meeting in May 2001 in Seattle, USA.

- I was one of the editorial board members for the OPAL paper "$D_s \to \tau \nu_\tau$ branching fraction measurement".

- Although OPAL is a large Collaboration, this $|V_{ub}|$ analysis is mainly done by me. This result was published in the Eur. Phy. J. C 21 (2001) 399 in August, 2001.

- I am a member of the LEP $|V_{ub}|$ working group which combines all LEP $|V_{ub}|$ measurements.

Appendix B

Glossary

ACCMM — Altarelli, Cabibbo, Corbà, Maiani and Martinelli, a model describing that the b quark and the spectator quark momenta in the b hadron rest frame follow a Gaussian distribution.

ALEPH — One of the four particle physics experiments at LEP.

ANN — Artificial Neural Network, a computational model applied to classification, pattern recognition and optimization, inspired by biological neural systems.

ARGUS — A collaboration that studied b and Υ physics using the DORIS electron-positron ring at DESY in Hamburg, Germany.

b and b — b represents a b quark, the fifth flavour of quark (in order of increasing mass), with electric charge -1/3. b represents a b hadron in this thesis.

BaBar — A collaboration that studies millions of B mesons produced by the PEP-II storage ring at SLAC.

BELLE A collaboration that studies millions of B mesons produced by the KEK b factory in Japan.

Bhabha event The event from $e^+e^- \to e^+e^-$ process.

BT B Tag neural network package from OPAL.

Calorimeter A composite detector using total absorption of particles to measure the energy and position of incident particles or jets.

CDF A detector for proton and anti-proton collider in Fermi National Accelerator Laboratory.

CERN European Organization for Nuclear Research.

CESR Cornell Electron Storage Ring.

CLEO A collaboration studying the production and decay of beauty and charm quarks and tau lepton produced in the Cornell Electron Storage Ring.

CKM matrix Cabibbo, Kobayashi and Maskawa, a matrix describing the relation between quark weak and mass eigenstates.

Collider An accelerator in which two beams traveling in opposite directions are steered together to provide high-energy collisions between the particles in one beam and those in the other.

Deadtime A span of time during which a detector, or an associated readout system, is unable to record new information.

DELPHI One of the four particle physics experiments at LEP.

DESY Deutsches Elektronen-Sychrotron at Hamburg, Germany. The laboratory performs basic research in high-energy and particle physics as well as in the production and application of synchrotron radiation.

Drift Chamber A multi-wire chamber in which spatial resolution is achieved by measuring the time electrons need to reach the anode wire, measured from the moment that the ionizing particle traversed the detector.

DST Data Summary Tape, a data format in OPAL which can be analyzed online and offline.

D0 A detector for proton and anti-proton collider in Fermi National Accelerator Laboratory.

Feynman diagram Schematic representation of an interaction between particles.

Flash ADC Flash Analog to Digital Converter, an ADC whose output code is determined in a single step by a bank of comparators and encoding logic.

FNAL Fermi National Accelerator Laboratory in Batavia, Illinois (near Chicago), named for particle physics pioneer Enrico Fermi.

Hadron A particle made of strongly-interacting constituents (quarks and/or gluons). These include the mesons and baryons. Such particles participate in strong interactions.

HQET	Heavy Quark Effective Theory, a theory used to describe heavy quark transitions.
ISGW	Isgur, Scora, Grinstein and Wise, a model describing B meson decays using form factors based on heavy quark symmetry.
Jet	Groups of particles moving in roughly the same direction.
JETSET	A Monte Carlo simulation program for jet fragmentation and e^+e^- physics.
JETNET	A program used to train the neural network.
KEK	Koo Energy Ken. The High Energy Accelerator Research Organization, Tsukuba, Japan.
KEKB	KEK B factory.
LEP	Large Electron Positron collider at the CERN laboratory in Geneva, Switzerland.
LINAC	LINear Accelerator.
L3	One of the four particle physics experiments at LEP.
MARK III	One of the particle physics experiments at SLAC.
OPAL	Omni Purpose Apparatus for LEP, one of the four particle physics experiments at LEP.
PDG	Particle Data Group.
PEP	Positron Electron Project, a 2.2 km circumference storage ring at SLAC.

PEP II — Upgraded SLAC PEP electron-positron collider. Its transformation into an asymmetric B-Factory included addition of a second storage ring, as well as new beam power and control systems.

QCD — Quantum ChromoDynamics, a gauge theory describing the strong interaction.

Radiation Length — Distance for a electron to have its energy reduced to 1/e of its original energy by Bremsstrahlung in traversing a layer of material.

Standard Model — The theory of fundamental particles and their interactions. It is widely tested and is accepted as correct by particle physicists.

ROPE — Reconstruction of OPAL Events.

SLAC — The Stanford Linear Accelerator Center in Stanford, California.

SLC — Stanford Linear Collider (100 GeV center of mass).

SLD — SLAC Large Detector, a particle physics detector for the SLC.

SU(3) — Group used to describe strong interaction.

SU(2) — Group used to describe weak interaction.

Tevatron — A proton accelerator at Fermilab which can accelerate protons to 1 TeV.

$W^{\pm}$ boson — A carrier particle of the weak interactions. It is involved in all electric-charge-changing weak processes.

Z boson	A carrier particle of weak interactions. It is involved in all weak processes that do not change flavour.
U(1)	Group used to describe quantum electrodynamics.
Υ(1S), Υ(2S), Υ(3S) and Υ(4S)	Four bound $b\bar{b}$ states.

Bibliography

[1] N. Cabibbo, Phys. Rev. Lett. **10** (1963) 531; M. Kobayashi and T. Maskawa, Prog. Theo. Phys. **49** (1973) 652.

[2] D. E. Groom *et al.*, Eur. Phys. J. **C15** (2000) 1.

[3] H. Leutwyler and M. Roos, Z. Phys. **C25** (1984) 91.

[4] CLEO Collaboration, J. P. Alexander *et al.*, Phys. Rev. Lett. **77** (1996) 5000.

[5] ALEPH Collaboration, CDF Collaboration, DELPHI Collaboration, L3 Collaboration, OPAL Collaboration and SLD Collaborations, D. Abbaneo *et al.*, "Combined results on B hadron production rates, lifetimes, oscillations and semileptonic decays", SLAC-PUB-8492, CERN-EP-2000-096 (2000); M. Battaglia, "Semileptonic B decays: recent results from LEP and comparison with Upsilon(4S) data", appearing in the proceedings of 5th Workshop on Heavy Quarks at Fixed Target (HQ2K), Rio de Janeiro, Brazil, 9-12 Oct 2000. e-Print Archive: hep-ph/0102170.

[6] DELPHI Collaboration, P. Abreu *et al.*, Phys. Lett. **B439** (1998) 209.

[7] P. F. Harrison and H. R. Quinn, Editors, "The Babar physics book", SLAC-R-504, October, 1998.

[8] ARGUS Collaboration, H. Albrecht *et al.*, Phys. Lett. **B234** (1990) 409.

[9] CLEO Collaboration, R. Fulton *et al.*, Phys. Rev. Lett. **64** (1990) 16.

[10] ALEPH Collaboration, R. Barate *et al.*, Eur. Phys. J. **C6** (1999) 555.

[11] DELPHI Collaboration, P. Abreu *et al.*, Phys. Lett. **B478** (2000) 14.

[12] L3 Collaboration, M. Acciarri *et al.*, Phys. Lett. **B436** (1998) 174.

[13] A. H. Hoang, Z. Ligeti and A. V. Manohar, Phys. Rev. **D59** (1999) 074017; A. H. Hoang, Z. Ligeti and A. V. Manohar, Phys. Rev. Lett. **82** (1999) 277.

[14] CLEO Collaboration, B. H. Behrens *et al.*, Phys. Rev. **D61** (2000) 052001.

[15] T. Sjöstrand, Comp. Phys. Comm. **82** (1994) 74.

[16] OPAL Collaboration, G. Alexander *et al.*, Z. Phys. **C69** (1996) 543.

[17] C. Ramirez, J. F. Donoghue and G. Burdman, Phys. Rev. **D41** (1990) 1496.

[18] S. W. Herb *et al.*, Phys. Rev. Lett. **39** (1977) 252.

[19] PLUTO Collaboration, C. Berger *et al.*, Phys. Lett. **B76** (1978) 243; C. W. Darden *et al.*, Phys. Lett **B76** (1978) 246.

[20] D. Andrews *et al.*, Phys. Rev. Lett. **45** (1980) 219; G. Finocchiaro *et al.*, Phys. Rev. Lett. **45** (1980) 222.

[21] CLEO Collaboration, S. Behrends *et al.*, Phys. Rev. Lett. **50** (1983) 881.

[22] ARGUS Collaboration, H. Albrecht *et al.*, Phys. Lett. **B192** (1987) 245.

[23] N. Isgur and M. B. Wise, Phys. Lett. **B232** (1989) 113; N. Isgur and M. B. Wise, Phys. Lett. **B237** (1990) 527.

[24] M. A. Shifman and M. B. Voloshin, Yad. Fiz. **45** (1987) 463, [Sov. J. Nucl.Phys. **45** (1987) 292]; M. A. Shifman and M. B. Voloshin, Yad. Fiz. **47** (1988) 801, [Sov. J. Nucl. Phys. **47** (1988) 511].

[25] ALEPH Collaboration, D. Buskulic *et al.*, Phys. Lett. **B311** (1993) 425; DELPHI Collaboration, P. Abreu *et al.*, Phys. Lett. **B311** (1993) 379.

[26] CLEO Collaboration, R. Ammar *et al.*, Phys. Rev. Lett. **71** (1993) 674.

[27] R. Greene, Nucl. Phys. Proc. Suppl. **65** (1998) 189.

[28] C. R. Jones, PhD thesis, " A measurement of the inclusive semileptonic branching fractions of b hadrons", University of Cambridge, August, 1999.

[29] C. Peterson, D. Schlatter, I. Schmitt and P. M. Zerwas, Phys. Rev. **D27** (1983) 105.

[30] P. D. B. Collins and T. P. Spiller, J. Phys. **G11** (1985) 1289.

[31] V. G. Kartvelishvili, A. K. Likhoded and V. A. Petrov, Phys. Lett. **B78** (1978) 615.

[32] B. Andersson, G. Gustafson and B. Soderberg, Z. Phys. **C20** (1983) 317.

[33] J. D. Richman and P. R. Burchat, Rev. Mod. Phys. **67** (1995) 893.

[34] N. Isgur, D. Scora, B. Grinstein and M. B. Wise, Phys. Rev. **D39** (1989) 799.

[35] CLEO Collaboration, R. Fulton *et al.*, Phys. Rev. **D43** (1991) 651.

[36] ARGUS Collaboration, H. Albrecht *et al.*, "Exclusive semileptonic decays of B mesons to D mesons", (1992), DESY-92-029.

[37] D. Scora and N. Isgur, Phys. Rev. **D52** (1995) 2783.

[38] CLEO Collaboration, B. Barish *et al.*, Phys. Rev. Lett. **76** (1996) 1570.

[39] P. Ball, M. Beneke and V. M. Braun, Phys. Rev. **D52** (1995) 3929.

[40] M. A. Shifman, N. G. Uraltsev and A. I. Vainshtein, Phys. Rev. **D51** (1995) 2217.

[41] ALEPH Collaboration, D. Buskuli *et al.*, "Measurement of the semileptonic b branching ratios from inclusive leptons in Z decay", (1995), Contributed Paper to EPS-HEP-95 Brussels, EPS-0404.

[42] DELPHI Collaboration, P. Abreu *et al.*, Z Phys. **C66** (1995) 323.

[43] OPAL Collaboration, R. Akers *et al.*, Z. Phys. **C60** (1993) 199.

[44] L3 Collaboration, M. Acciarri *et al.*, Z. Phys. **C71** (1996) 379.

[45] A. H. Hoang, Z. Ligeti and A. V. Manohar, Phys. Rev. Lett. **82** (1999) 277; A. H. Hoang, Z. Ligeti and A. V. Manohar, Phys. Rev. **D59** (1999) 074017.

[46] UKQCD Collaboration, L. D. Debbio *et al.*, Phys. Lett. **B416** (1998) 392.

[47] P. Ball and V. M. Braun, Phys. Rev. **D58** (1998) 094016.

[48] Z. Ligeti and M. B. Wise, Phys. Rev. **D53** (1996) 4937; E791 Collaboration, E. M. Aitala *et al.*, Phys. Rev. Lett. **80** (1998) 1393.

[49] M. Beyer and D. Melikhov, Phys. Lett. **B436** (1998) 344.

[50] CLEO Collaboration, R. Fulton *et al.*, Phys. Rev. Lett. **64** (1990) 16.

[51] CLEO Collaboration, J. Bartelt, Phys. Rev. Lett. **71** (1993) 4111

[52] B. Grinstein, M. B. Wise, and N. Isgur, Phys. Rev. Lett. **56** (1986) 298.

[53] M. Wirbel, B. Stech and M. Bauer, Z. Phys. **C29** (1985) 637; J. G. Körner and G. A. Schuler, Z. Phys. **C38** (1988) 511.

[54] G. Altarelli, N. Cabibbo, G. Corbà, L. Maiani and G. Martinelli, Nucl. Phys. **B208** (1982) 365.

[55] T. Mannel and M. Neubert, Phys. Rev. **D50** (1994) 2037.

[56] M. Neubert, Phys. Rev. **D49** (1994) 4623.

[57] R. D. Dikeman, M. Shifman and N. G. Uraltsev, Int. J. Mod. Phys. **A11** (1996) 571.

[58] A. Bareiss and E. A. Paschos, Nucl. Phys. **B327** (1989) 353.

[59] M. Jezabek and J.H. Kühn, Nucl. Phys. **B314** (1989) 1.

[60] CLEO Collaboration, M. S. Alam *et al.*, Phys. Rev. Lett. **74** (1995) 2885.

[61] D. S. Hwang, C. S. Kim and W. Namgung, Phys. Lett. **B406** (1997) 117.

[62] A. Ali and C. Greub, "Photon energy spectrum in B $\to X_s\gamma$ and comparison with data", DESY 95-117.

[63] W. F. Palmer, E. A. Paschos and P. H. Soldan, Phys. Rev. **D56** (1997) 5794.

[64] E. Bagan, P. Ball, V.M. Braun, and H. G. Dosch, Phys. Lett. **B278** (1992) 457.

[65] M. Neubert, Phys. Rev. **D46** (1992) 1076.

[66] K. S. Kölbig, J. A. Mignaco and E. Remiddi, BIT **10** (1970) 38.

[67] K. S. Kölbig, SIAM J. Math. Anal. **17** (1986) 1232; **46** (1992) 1076; M. Neubert, Phys. Rev. **D45** (1992) 2451.

[68] G. Altarelli, G. Parisi, Nucl. Phys. **B126** (1977) 298.

[69] OPAL Collaboration, G. Abbiendi *et al.*, Phys. Lett. **B444** (1998) 539.

[70] J. Allison *et al.*, Nucl. Instrum. Meth. **A317** (1992) 47.

[71] OPAL Collaboration, K. Ahmet *et al.*, Nucl. Instrum. Meth. **A305** (1991) 275.

[72] http://opalinfo.cern.ch/opal/plots/publicity/publicity.html

[73] http://welcome.cern.ch/

[74] http://opal.web.cern.ch/Opal/welcome.html

[75] OPAL Collaboration, P. P. Allport *et al.*, Nucl. Instrum. Meth. **A346** (1994) 476; OPAL Collaboration, A. Honma, Nucl. Instrum. Meth. **A348** (1994) 409; S. Anderson *et al.*, Nucl. Instrum. Meth. **A403** (1998) 326.

[76] J. R. Carter *et al.*, Nucl. Instrum. Meth. **A286** (1990) 99.

[77] H. M. Fischer *et al.*, Nucl. Instrum. Meth. **A283** (1989) 492.

[78] H. Mes *et al.*, Nucl. Instrum. Meth. **A265** (1988) 445.

[79] R. J. Akers *et al.*, Nucl. Instrum. Meth. **A357** (1995) 253.

[80] M. Hauschild *et al.*, Nucl. Instrum. Meth. **A314** (1992) 74.

[81] O. Biebel *et al.*, Nucl. Instrum. Meth. **A323** (1992) 169.

[82] J. An *et al.*, Nucl. Instrum. Meth. **A267** (1988) 386; J. An *et al.*, Nucl. Instrum. Meth. **A267** (1988) 396.

[83] C. Beard *et al.*, Nucl. Instrum. Meth. **A286** (1990) 117.

[84] M. Ajrawy *et al.*, Nucl. Instrum. Meth. **A290** (1990) 76.

[85] G. Artusi *et al.*, Nucl. Instrum. Method. **A279** (1989) 523.

[86] G. Mikenberg, Nucl. Instrum. Method. **A265** (1988) 223.

[87] M. Arignon *et al.*, Nucl. Instrum. Method. **A333** (1993) 330; OPAL Collaboration, M. Arignon *et al.*, Nucl. Instrum. Method. **A313** (1992) 103.

[88] OPAL Collaboration, R. Akers *et al.*, Z. Phys. **C66** (1995) 555.

[89] OPAL Collaboration, G. Abbiendi *et al.*, Eur. Phys. J. **C8** (1999) 217.

[90] OPAL collaboration, G. Alexander *et al.*, Z. Phys. **C52** (1991) 175.

[91] R. Hawkings, "High performance b-tagging using 3D vertexing and neural networks", OPAL Technical Note TN515, September 1997.

[92] L. del Pozo, "Jet finding with a cone algorithm", OPAL Technical Note TN170, June 1993.

[93] OPAL Collaboration, R. Akers *et al.*, Z. Phys. **C63** (1994) 197.

[94] O. Cooke, C. Jones, " Neural network electron and photon conversion identification", OPAL Technical Note TN556, July 1998.

[95] OPAL Collaboration, G. Abbiendi *et al.*, Eur. Phys. J. **C13** (2000) 225.

[96] C. Peterson *et al.*, Comp. Phys. Comm. **81** (1994) 185.

[97] R. Hawkings, "Vertex tagging of b-hadrons using 3D tracking and neural networks", OPAL Technical Note TN366 , April, 1996.

[98] Simon Robins, "Inclusive reconstruction of b hadrons", OPAL Technical Note, TN594, January, 1999.

[99] The LEP collaboration, ALEPH, DELPHI, L3 and OPAL, Nucl. Instrum. Meth. **A378** (1996) 101.

[100] SLD collaboration, K. Abe *et al.*, Phys. Rev. Lett. **84** (2000) 4300.

[101] OPAL Collaboration, G. Alexander *et al.*, Z. Phys. **C72** (1996) 1.

[102] MARK III Collaboration, D. Coffman *et al.*, Phys. Lett. **B263** (1991) 135.

[103] CLEO Collaboration, S. Henderson *et al.*, Phys. Rev. **D45** (1992) 2212.

[104] F. E. Close, J. G. Körner, R. J. N. Phillips and D. J. Summers, J. Phys. **G18** (1992) 1573; T. Mannel and G. Schuler, Phys. Lett. **B279** (1992) 194; A. F. Falk and M. E. Peskin, Phys. Rev. **D49** (1994) 3320.

[105] ARGUS Collaboration, H. Albrecht *et al.*, Z. Phys. **C57** (1993) 533.

[106] ALEPH Collaboration, D. Buskulic *et al.*, Z. Phys. **C73** (1997) 601.

[107] DELPHI Collaboration, P. Abreu *et al.*, Phys. Lett. **B475** (2000) 407.

[108] B. Mele and G. Altarelli, Phys. Lett. **B299** (1993) 345; B. Mele, Mod. Phys. Lett. **A9** (1994) 1239.

[109] N. G. Uraltsev, Int. J. Mod. Phys. **A14** (1999) 4641.

[110] I. I. Bigi, N. G. Uraltsev and A. I. Vainshtein, Phys. Lett. **B293** (1992) 430; I. I. Bigi, M. A. Shifman, N. G. Uraltsev and A. I. Vainshtein, Phys. Rev. Lett. **71** (1993) 496.

[111] K. Melnikov, A. Yelkhovsky, Phys. Rev. **D59** (1999) 114009; A. H. Hoang, Phys. Rev. **D61** (2000) 034005

[112] L. Lyons, D. Gibaut and P. Clifford, Nucl. Instrum. Meth. **A270** (1998) 110.

[113] D. Abbaneo, M. Battaglia, P. Gagnon, P. Henrad, J. Lu, S. Mele, E. Piotto and P. Rosnet, "Determination of the LEP average Br($b \to X_u \ell \nu$) and derivation of $|V_{ub}|$", LEPVUB-01/01, June, 2001.